August 2018

Uncertainty Assessment of Spectral Mixture Analysis in Remote Sensing Imagery

Yingbin Deng
University of Wisconsin-Milwaukee

UNCERTAINTY ASSESSMENT OF SPECTRAL MIXTURE ANALYSIS IN REMOTE SENSING IMAGERY

by

Yingbin Deng

A Dissertation Submitted in

Partial Fulfillment of the

Requirements for the Degree of

Doctor of Philosophy

in Geography

at

The University of Wisconsin-Milwaukee

August 2018

ABSTRACT

UNCERTAINTY ASSESSMENT OF SPECTRAL MIXTURE ANALYSIS IN REMOTE SENSING IMAGERY

by

Yingbin Deng

The University of Wisconsin-Milwaukee, 2018

Under the Supervision of Professor Changshan Wu

Spectral mixture analysis (SMA), a scheme of sub-pixel-based classifications, is one of the widely used models to map fractional land use and land cover information in remote sensing imagery. It assumes that: 1) a mixed pixel is composed by several pure land cover classes (endmembers) linearly or nonlinearly, and 2) the spectral signature of each endmember is a constant within the entire spatial extent of analysis. SMA has been commonly applied to impervious surface area extraction, vegetation fraction estimation, and land use and land cover change (LULC) mapping. Limitations of SMA, however, still exist. First, the existence of between- and within-class variability prevents the selection of accurate endmembers, which results in poor accuracy of fractional land cover estimates. Weighted spectral mixture analysis (WSMA) and transformed spectral mixture analysis (TSMA) are alternate means to address the within- and between- class variability. These methods, however, have not been analyzed systematically and comprehensively. The effectiveness of each WSMA and TSMA scheme is still unknown, in particular within different urban areas. Second, multiple endmember SMA (MESMA) is a better alternative to address spectral mixture model uncertainties. It, nonetheless, is time consuming and

inefficient. Further, incorrect endmember selections may still limit model performance as the best-fit endmember model might not be the optimal model due to the existence of spectral variability. Therefore, this study aims 1) to explore endmember uncertainties by examining WSMA and TSMA modeling comprehensively, and 2) to develop an improved MESMA model in order to address the uncertainties of spectral mixture models.

Results of the WSMA examination illustrated that some weighting schemes did reduce endmember uncertainties since they could improve the fractional estimates significantly. The results also indicated that spectral class variance played a key role in addressing the endmember uncertainties, as the better performing weighting schemes were constructed with spectral class variance. In addition, the results of TSMA examination demonstrated that some TSMAs, such as normalized spectral mixture analysis (NSMA), could effectively solve the endmember uncertainties because of their stable performance in different study areas. Results of Class-based MEMSA (C-MESMA) indicated that it could address spectral mixture model uncertainties by reducing a lot of the calculation burden and effectively improving accuracy. Assessment demonstrated that C-MEMSA significantly improving accuracy.

Major contributions of this study can be summarized as follow. First, the effectiveness of addressing endmember uncertainties have been fully discussed by examining: 1) the effectiveness of ten weighted spectral mixture models in urban environments; and 2) the effectiveness of 26 transformed spectral mixture models in three locations. Constructive guidance regarding handling endmember uncertainties using WSMA and TSMA have been provided. Second, the uncertainties of spectral mixture model were reduced by developing an improved MESMA model, named C-MESMA. C-MESMA could restrict the distribution of endmembers and reduce the calculation burden of traditional MESMA, increasing SMA accuracy significantly.

Dedicated to my wife,
my daughter,
and my parents

TABLE OF CONTENTS

LIST OF FIGURES

LIST OF TABLES

ACKNOWLEDGEMENTS

This work would not have been possible without the help of my advisor, Professor Changshan Wu, who provided significant support for both my academic career and daily life. Professor Wu's research experience has greatly supported of my career goals.

I also want to extend appreciation to my committee members, Distinguished Professor Mark D. Schwartz, Professor Woonsup Choi, Professor Zengwang Xu, and Professor Lingqian Hu, for their valuable comments and suggestions for my dissertation work.

In addition, I also want to thank all faculty members in the department of Geography, University of Wisconsin – Milwaukee, who provided help during my time here. Thanks also to faculty in the School of Geographical Science, South China Normal University, specially Professor Fenglie Fan, Professor Weihong Li, and Dr. Haixia. I would also like to thank colleagues, Gainbi, Haijian, Wenliang, Yang, Wei Xu, Wei Fan, Bailu, Minji, Muriel, Nick, Feng, and Susan and my closest friends Dr. Miao Li, Yejun, Kejia, Zhejia, Huakeng, Runnan, Chenhuai, Junjie, Dr. Jizhe, Yingzhi, Xiaojun, and many friends not listed, for sharing some memorable time with me.

Moreover, I also want to thank my family, my wife, my daughter, my parents and parents in law, and my brother. Without their help and understanding, I could not accomplish this task.

CHAPTER1 INTRODUCTION

1.1 Background

Knowledge of land use and land cover distributions and their dynamics is critical for understanding environmental characteristics and processes, including biodiversity, land productivity, and biogeochemical and hydrological cycles (Giri, 2012). Moreover, detection and monitoring of the distribution and dynamics of the world's water resources, grasslands, croplands, shrub lands, forests, barren lands, and urban lands are basic requirements for studies of daily planning and management, as well as global environmental change analysis (Giri, 2012). Land use and land cover information is a fundamental element of natural resource management and global environmental change monitoring (Loveland and Belward, 1997), and it has been employed in numerous studies, including biodiversity (Sala et al., 2000), soil degradation (Trimble and Crosson, 2000), global climatic change (Pyke and Andelman, 2007), resource management (Tallis and Polasky, 2009), and urban planning (Zhang et al., 2011).

Due to its importance, scientists and professionals have employed numerous means to acquire land use and land cover information, which can be grouped into two categories: traditional approaches and remote sensing techniques. Traditional approaches, such as field surveys and observations, can provide accurate and highly reliable results. These methods, however, are time consuming and labor intensive, thereby impractical for applications of large geographic regions. With the recent appearance of remote sensing and geographical information systems, the abovementioned drawbacks can be addressed because of the possibility of detecting and monitoring land use and land cover change at multiple spatial and temporal scales (Hansen and DeFries, 2004). Remote sensing provides an ideal tool for environmental monitoring and management, target identification, and hazard detection and simulation, etc. Information in all

wavelengths can be recorded by a sensor, removing the limitation of using only visual wavelengths (0.39um-0.7um) seen by humans. Remote sensing has been widely employed by natural resource departments, real estate companies, research institutions, and other environmental organizations, attributing to its convenience of acquiring up-to-date land use and land cover information over a large geographical area.

Advantages of remote sensing techniques are significant when compared to the conventional approaches. First, remote sensing provides an economical and rapid means of acquiring up-to-date LULC information. A scene of remotely sensed imagery can cover a large geographic area, whereas it may be time and labor intensive with field surveys. Second, remote sensing data is acquired in digital formats, which is convenient to store, analyze, and visualize. Third, as remote sensing techniques can collect objects' information without physical contact, they can be applied to acquire information from inaccessible geographic areas. Moreover, with remotely sensed imagery, an overview of landscape elements and their interrelations can be conveniently identified (De Jong and van der Meer, 2004). Finally, remote sensors can record information in wavelengths invisible to humans, enhancing characteristic information of land surfaces. In summary, remotely sensed imagery provides a better alternative in acquiring LULC information for large geographic areas.

With the advancement of digital storage and computer techniques, LULC classes can be directly classified from remotely sensed imagery, which greatly improves the efficiency of LULC mapping. In particular, three classification techniques, pixel-based, subpixel-based, and object-based methods, have been developed. Pixel-based approaches assume that each pixel only contains one LULC class. Accordingly, every pixel is assigned to the corresponding LULC class based on specific mathematical/statistical methods and rules. Traditional pixel-based methods, such as

maximum likelihood classification, minimum distance classification, and spectral angle mapper, are widely employed in remote sensing applications due to their convenience and simplicity. Unlike pixel-based classification, subpixel-based methods assume that more than one class exists in each pixel, and thereby attempt to estimate their areal coverage within a pixel. In contrast to pixel-based and subpixel-based method, object-based classifications view landscapes as aggregations of independent objects corresponding to ground entities and patches of surface cover (Arbiol et al., 2006). It has advantages in addressing the high spectral variability of very high resolution (VHR) imagery.

Within medium and coarse spatial resolution remote sensing imagery, subpixel approaches have been widely applied. With these approaches, a pixel is not assigned to only one particular land cover class, whereas several classes are assumed to co-exist in each pixel, and their areal fractions are estimated (Ling et al., 2012). Due to their better representation of LULC information in medium and coarse resolution remotely sensed imagery, subpixel approaches have been largely employed in the applications of LULC identification, vegetation-impervious surface area-soil fraction mapping, vegetation type estimation, etc. For subpixel analyses, three groups of techniques have been generally applied to estimate land cover fractions, and they include: soft classification, empirical estimation, and spectral mixture analysis (Eastman and Laney, 2002; Ling et al., 2012). Soft classification (in contrast to the hard classification) assigns one or more land cover classes to each pixel by computing the probabilities (or likelihood) that a class exists in that pixel. Many approaches, such as maximum likelihood classification (Foody et al., 1992), Fuzzy c-means (Pathirana and Fisher, 1991), Possibilistic c-Means (Krishnapuram et al., 1993), soft neural networks (Tso and Mather, 2001) have been proposed as soft classification techniques to estimate the fraction of each land cover class. In contrast to soft classification methods, empirical

approaches estimate the fractions based on the trained or calibrated models (Eastman and Laney, 2002). Spectral mixture analysis (SMA), another scheme of sub-pixel classifications, is one of the widely used models to address the mixed pixel problem (Deng et al., 2012; Wu and Murray, 2003). Two essential assumptions of SMA include: 1) a mixed pixel is composed by a few fundamental components (most often less than 5 endmembers), each of which is spectrally distinctive from others; and 2) the spectral signature for each component is a constant throughout the entire spatial extent of the analysis (Song, 2005). SMA has been commonly applied to impervious surface area extraction, vegetation fraction estimation, and LULC mapping.

Although SMA is a popular approach to address the mixed pixel problem, little research focuses on its uncertainties. Most studies simply employed SMA models for specific applications, and reported their performances for specific applications and study areas with a pre-determined remotely sensed imagery. Most efforts, however, focused on the model performance for specific applications, and ignored the factors that may influence results. Therefore, it is necessary to perform a thorough study of uncertainties of SMA modeling. The objectives of this research, therefore, are to examine the fundamental theories of SMA and to analyze the uncertainties of SMA, which should result in a better understanding of SMA and provide guideline for future SMA applications.

1.2 Literature Review

1.2.1 Spectral mixture analysis

Spectral mixture analysis (SMA) is one of the most popular methods for subpixel analysis. It emerged with the development of the first LANDSAT satellite launched in the early 1970s. SMA assumes that a pixel is composed by two or more land cover classes mixed linearly or nonlinearly. With the linear approach, a pixel is assumed to be large enough and no multiple scattering exists

among the components (Singer and McCord, 1979). Obviously, this condition rarely exists in most remote sensing images. Nonlinear models, to a certain degree, can better represent the actual multi-scattering process, but they are difficult to implement and the results are less than satisfactory because of complications from multiple scatterings. As a result, linear SMA has been largely employed for applications of vegetation information extraction (Alejandro and Omasa, 2007; Elmore et al., 2000; Liu and Yang, 2013), land use and land cover change detection (Franke et al., 2009; Pu et al., 2008), water quality monitoring (Rudorff et al., 2006), and forest degradation estimation (Souza et al., 2003) etc.

SMA can be divided into four steps, including: 1) data preprocessing, 2) endmember selection, 3) spectral unmixing, and 4) accuracy assessment. Each step is very important and may have a critical impact on the SMA results.

1) Data preprocessing. The original values of raw remotely sensed imagery are called digital numbers. These raw data need to be converted to radiance/reflectance before implementing SMA. In addition, atmospheric correction and geometric correction are generally necessary to mitigate the impacts of atmospheric and geometric errors. In addition to the abovementioned basic processes, spectral transformations, such as principle component analysis [PCA, (Jia and Richards, 1999; Singh, 1989)], discrete cosine transform(Ahmed et al., 1974; Chu and Zhu, 2006), minimum noise fraction [MNF, (Amato et al., 2009; Vermillion and Sader, 1999)], and band normalization etc., may be employed to enhance spectral characteristics.
2) Endmember selections. Endmembers, extracted from a pure pixel (only one land cover class in a pixel) or measured from a field survey, are the most representative spectra of the corresponding land cover classes. Selecting an appropriate endmember set is a key step

for a successful subpixel land cover estimation with SMA (Elmore et al., 2000; Tompkins et al., 1997). The accuracy of the estimated fractional land covers is highly dependent on the selection of endmember sets. Choosing the best-fit endmember set determines the proper number and type of endmembers and their corresponding spectra (Somers et al., 2011). Too many or too few of endmembers can lead to erroneous results that conflict with the reference data (Somers et al., 2011). Many endmember selection methods, e.g., manually selection, field measured, pixel purity index [PPI, (Plaza et al., 2006)], virtual endmember concept (Tompkins et al., 1997), iterative error analysis [IEA, (Neville et al., 1999)], convex cone analysis [CCA, (Chu et al., 2007)], automated morphological endmember extraction [AMEE, (Plaza et al., 2004)], simulated annealing algorithm [SAA, (Ogbu and Smith, 1990)], and N-FINDR (Winter, 1999), have been proposed to select the optimal endmember set. All have met with some success.

3) Spectral unmixing. This procedure involves the selection of a best-fit model, e.g., linear or nonlinear, and constrained or non-constrained. As landscapes vary from region to region, the selection of the optimal model may be different in different study areas. For example, in deserts, a linear model may be more appropriate as multi-scattering effects are insignificant due to the simplicity of land covers (e.g. shrubs and sand). In contrast to desert regions, forest areas and downtown urban regions may contain many types of land features, leading to significant multi-scattering effects, thereby causing obvious spectral variability in remotely sensed imagery. The selection of an inappropriate model may lead to inaccurate fractional land cover estimates.

Due to the limitations of the simple SMA model, where only a few endmembers can be involved in the unmixing process, many improved models have been proposed to mitigate

this drawback of simple SMA. In particular, Roberts et al. (1998) proposed a multiple endmember spectral mixture analysis (MESMA), with which endmember sets can be varied from pixel to pixel, to increase the accuracy of SMA. Results implied that MESMA is an ideal way to deal with endmember's within-class and between-class variability.

Generally, linear and nonlinear SMA models can be expressed as equations (1) and (2) respectively.

$$R = \sum_{k=1}^{n} f_k R_k + ER \quad (1)$$

$$nR = \sum_{k=1}^{n} f_k \times R_k + \sum_{x=1}^{n} \sum_{y=x+1}^{n} f_{xy} \times R_x \times R_y + ER \quad (2)$$

where $k = 1,\ldots, n$ (n: the number of endmember); f_k is the proportion of endmember k; R_k, R_x, and R_y are the known spectral reflectance of endmember k within a pixel; and ER is the estimation error. The fully constrained method should meet the requirements of sum-to-one ($\sum_{k=1}^{n} f_k = 1$) and non-negativity ($1 > f_k > 0$).

4) Accuracy assessment. This step is to assess the performance of an SMA model. Subpixel-based accuracy assessment, which assesses the fractions' accuracy of each land cover class in a pixel, is different from the traditional pixel-based classification, which evaluates the accuracy on a per-pixel basis. Traditional accuracy assessment methods, such as error matrix, kappa index, and overall accuracy, are not applicable to subpixel-based analysis. The most commonly used method for assessing the accuracy of an SMA model is the root mean square error (RMSE), which compares the fractional values between reference and modeling results. The higher the RMSE, the lower the modeling accuracy. Another method,

called mean absolute error (MAE), is also commonly applied to assess the accuracy. RMSE and MAE can be written as Equations (3) and (4).

$$RMSE = \sqrt{\sum_{i=1}^{N} \frac{(x_i - \hat{x})^2}{N}} \quad (3)$$

$$MAE = \frac{1}{N} \sum_{i=1}^{N} \left| x_i - \hat{x} \right| \quad (4)$$

where N is the total band number, i means the band i. x_i and $\hat{x}$ are the estimated and reference values respectively.

1.2.2 Weighted spectral mixture analysis

Weighted spectral mixture analysis (WSMA), a popular means to address spectral endmember variability, assumes that each waveband's contribution to SMA results is unequal. This is because of: 1) endmember similarity which adds instability to the unmixing (Barducci and Mecocci, 2005); and 2) the relationship between estimated error and the mixing scale of endmembers is positive (Somers et al., 2009). In particular, wavebands with highest reflectance/radiance have more impact on estimated result while wavebands with lower values play weaker roles in unmxing (Somers et al., 2009). Somers et al. (2009) emphasized that significant estimation errors might appear when differences in the reflected energy among wavebands is ignored.

WSMA has been discussed by serval scholars. Chang and Ji (2006) explored three types of weighted matrices in the linear unmixing model, expanding the abundance-constrained linear spectral mixture analysis (AC-LSMA). They constructed weighting schemes based on three aspects: parameter estimation, pattern classification, and orthogonal subspace projection. Results demonstrated that the within-class weighting scheme (WAC-LSMA) showed the best performance among the weighted and unweighted schemes. Liu et al. (2013) extended the WAC-LSMA to a

kernel-based linear spectral mixture analysis (KWAC-LSMA) by employing a kernelized weighting matrix. The new proposed weighting scheme was applied on both multispectral and hyperspectral images. Experimental results indicated that KWAC-LSMA outperformed the WAC-LSMA as well as the unweighted scheme when used on high spectral resolution but low spatial resolution data set. However, the KWAC-LSMA did not improve the accuracy when compared to WAC-LSMA using the HYDICE data (high spectral and spatial resolution) and SPOT data (high spatial resolution but only three wavebands are available). Somers et al. (2009) analyzed the relationship between the endmember variability and reflected energy and examined their impacts on fractional accuracy. They concluded that a waveband with the highest reflected energy contributes more to the spectral variability for fractional estimates. With this discovery, they proposed a two-step WSMA to address endmember variability in agricultural production systems. First, they constructed two schemes, a reflected energy fixed value weighting scheme (REFW) and an inverse InStability Index (ISIb). Second, a final weighting (WV) scheme was built using the products of REFW and ISIb. Mean absolute error of 0.06 could be reduced with the WV in this study. Veraverbeke et al. (2012) applied the WV on multiple endmember spectral mixture analysis (MESMA) to map fire severity and achieved promising results. In addition, a band weighting method was proposed by Pan et al. (2005) which assigned weighting scores based on how remarkable an edge is relative to its corresponding boundary. Results from the abovementioned studies demonstrated the better performance of weighted models compared to unweighted counterparts.

1.2.3 Transformed SMA (TSMA)

Spectral transformation, which changes the original spectra linearly and nonlinearly, is another technique used to address spectral endmember variability. Linear transformation keeps the linear

relationship between variables, while nonlinear transformation changes the linearity between variables. Like spectral weighting, a spectral transformation also aims to emphasize spectral characteristics to reduce within-class variability or to enhance between-class variability.

Spectral transformation has been widely applied by scholars. Wu (2004) developed a normalized spectral mixture analysis (NSMA) to derive vegetation, impervious surface areas, and soil information. Brightness variations were reduced after the NSMA, increasing the accuracy of fractional estimation. Asner and Lobell (2000) subtracted all spectral bands by the tie band (also named tie spectra) respectively. This method is named tie spectral transformation. Significant variation of canopy architecture, soil moisture, leaf and litter area index, and tissue optics could be detected, resulting in more accurate outputs in the unmixing process. Derivative spectral unmixing (DSU) is also promising for fractional estimation with hyperspectral data. Studies of Zhang et al. (2004), Tsai and Philpot (1998), Laba et al. (2005), and Huguenin and Jones (1986) also verified DSU's outstanding performance. Debba et al. (2006) summarized that higher-order derivatives contribute more to remote sensing imagery with higher signal-to-noise ratios. Li (2004) compared the performance of discrete wavelet transform (DWT) and principal component analysis (PCA), and he revealed that DWT could increase more separability than PCA, bringing significant improvement of fractional estimation. Similar conclusions were obtained from the studies of Bruce et al. (2002) and Zhang et al. (2006). Youngentob et al. (2011) examined the performance of continuum removal (CR) analysis using the hyperspectral data and results showed improvements of the overall accuracy. They believed that CR analysis can contribute to class separability through highlighting individual absorption features across a normalized spectrum. Principal component analysis (PCA) (Richards and Richards, 1999), minimum noise fraction transform (MNF) (Green et al., 1988), Tasseled Cap (TC) (Jensen and Lulla, 1987), and

independent component analysis (ICA) (Hyvärinen and Oja, 2000) are commonly applied for the land surface feature enhancement before applying SMA. Spectral characteristics of different land cover classes are enhanced in different output layers. Many researchers employed these transformation techniques to assist the selection of endmembers as well as to reduce the spectral within-class variability and enhance between-class variability. Further, different spatial filters, such as low pass (LP), high pass (HP), Gaussian high pass (GHP), Gaussian low pass (GLP), are commonly employed to enhance the spectral characteristics' edges or to smooth the surface of remote sensing imagery.

1.2.4 Class-based Multispectral mixture analysis

Traditional SMA approaches perform reasonably well in areas with relatively homogenous land covers, mostly due to the ease of identifying representative endmembers. It applies a fixed set of endmembers in fractional estimation. The capability of traditional SMA models in dealing with complex urban and suburban landscapes, however, has been questioned as: 1) inter-class and intra-class spectral variability widely exist in urban and suburban environments (Kumar et al., 2013; Roth et al., 2012; Settle, 2006; Thorp et al., 2013; Youngentob et al., 2011), and 2) the few endmembers may not be able to represent their corresponding land cover classes (Radeloff et al., 1999; Song, 2005; Tang et al., 2007).

As an improved SMA, multiple endmember spectral mixture analysis (MESMA) developed by Roberts et al. (1998), has successfully addressed the issues of spectral variability, and been widely applied to numerous fields, including impervious surface area (ISA) extraction (Fan and Deng, 2014; Franke et al., 2009), vegetation detection (Fernández-Manso et al., 2012; Fernandez-Manso et al., 2016; Thorp et al., 2013), and water management (Song et al., 2013; Xie et al., 2016), etc. Franke *et al.* (Franke et al., 2009) developed a hierarchical multiple endmember spectral

mixture analysis to divide an image into several land cover types (i.e., several levels). The distribution of endmembers could be better determined from the separated images, thereby improving classification accuracy. Similarly, Liu and Yang (2013) classified the study area into rural and urban subsets with the assistance of road network density. Then they applied MESMA to urban subsets with endmembers of vegetation, ISA, and soil, while employing a supervised classification model for the rural area. Results illustrated that this method could minimize the spectral confusion between some urban land cover classes and agricultural landscapes.

1.3 Problem statement

1.3.1 Weighted SMA (WSMA)

Several scholars have analyzed WSMA, however, it still has not been discussed adequately. The best method for WSMA to address endmember variability is still not clear. Existing studies show that accuracy improvement can be achieved. These improvements, nonetheless, may be limited to specified study areas and data sources. Chang and Ji (2006) and Liu et al. (2013) focused on the abundance-constrained linear spectral model. Their study area only included forests and farmlands, where endmember variability is relative low when compared to urban regions. Similarly, Somers et al. (2009) also highlighted the capability of WSMA in vegetation areas. Study sites with more spectral variability, such as the areas containing both impervious surfaces areas (ISAs) and vegetation, have yet to be explored. Therefore, it is imperative to examine the performance of WSMA in urban areas where spectral variability is large.

1.3.2 Transformed SMA (TSMA)

Although many researchers applied spectral transformation techniques in remote sensing applications, there is still a lack of comprehensive and systematic studies to examine their

effectiveness in addressing endmember variability. In particular, researchers employ different transformed schemes based on their own knowledge and expertise. The advantages and limitations of each transformed scheme are still unclear, and the necessity of applying transformed schemes has not been adequately discussed in the literature. Some researchers state that nonlinear transformations may violate the linear composition assumptions of SMA and it may decrease the accuracy of abundance estimation (Li, 2002). However, the selection criteria for linear or nonlinear transformation schemes is still unclear, and few scholars discuss the effects of linearity in their studies. Therefore, it is necessary to analyze the effectiveness of transformed SMA (TSMA) systematically.

1.3.3 Class-based Multispectral mixture analysis

MESMA chooses the best-fit endmember model by evaluating modeling errors, such as root mean square of the residual error [RMSRE, (Roberts et al., 1998; Tan et al., 2014)]. Generally, with the same number of endmembers, a model with a smaller RMSRE is chosen. In the case of the availability of different endmembers' numbers, the model with fewer number of endmembers is selected when their RMSRE's difference is trivial (Song, 2005). It is a key step to select an appropriate endmember set for successful spectral unmixing (Somers et al., 2011). In particular, over-estimated abundance will occur if an endmember is mistakenly included in an SMA model (Jia et al., 2010). Moreover, accepting minimized RMSRE as the best criterion may not be appropriate in the endmember selection. Some erroneously selected endmembers may have a better fit due to the existence of within-class and between-class spectral variability, which constitutes a major uncertainty of spectral mixture models.

A critical limitation of hierarchical MESMA (Franke et al., 2009) is that a pixel at level 1 is assigned to ISA or pervious surface class based on their corresponding fraction values results from

a linear SMA. In this case, mixed pixel issues are not addressed since the pixel-based classification is at level 1. Moreover, results from hierarchical MESMA are promising for application in higher spatial resolution images (4 meters). However, hierarchical MESMA still needs to be verified in middle and coarse resolution images. Liu and Yang (2013) applied a vegetation cover threshold to separate vegetation and non-vegetation. This threshold, however, is pixel-based, which would also contain mixed pixels in both vegetation and non-vegetation classes.

CHAPTER2 EXAMINING THE EFFECTIVENESS OF WEIGHTED SPECTRAL MIXTURE ANALYSIS (WSMA) IN URBAN ENVIRONMENTS[1]

2.1 Introduction

Spectral mixture analysis (SMA) is widely employed for extracting land cover information from remote sensing imagery due to its convenience, high accuracy, and easy implementation (Weng, 2012; Wu and Murray, 2003). SMA assumes that a mixed pixel is modeled by spectra of several pure land cover classes or endmembers (Deng et al., 2012; Deng and Wu, 2016; Wu and Murray, 2003). Four major characteristics of SMA have earned its broad acceptance in remote sensing applications. First, it converts the reflectance or radiance of a land surface feature to physical variables instead of probabilities or likelihood (Tompkins et al., 1997). Second, substances can be detected and their quantities can be represented in resultant fractional land cover imageries (Tompkins et al., 1997). Third, many computer programs, such as ENVI and ERDAS Imagine, have embedded SMA models. Results of SMA can be easily acquired and interpreted using these programs (Tompkins et al., 1997). Finally, SMA has been employed in a wide variety of research fields, such as land use and land cover change detection (Lu et al., 2004; Small, 2001; Wu and Murray, 2003), precision agriculture and production monitoring (Liu, 2008; Lobell and Asner, 2004), urban environmental ecology research (Deng and Wu, 2013a; Yuan and Bauer, 2007), terrestrial ecosystem research (Alejandro and Omasa, 2007), forest hazard risk detection and management (Wessman et al., 1997), water quality assessment (Mertes et al., 1993), and geological mapping (Bedini et al., 2009). Its advantages and limitations have been largely discussed by researchers, providing many meaningful resources for further studies. Due to the complexity of non-linear SMA, it is difficult to compare the result of different models. Therefore, linear SMA

[1]Portions of this chapter have been published in *International Journal of Remote Sensing*, coauthored with Dr. Changshan Wu, Xin Zhang, and Xiuping Jia

was the only focus in this study. SMA in the rest of this chapter means linear SMA.When applying SMA, most scholars assume that each waveband of remotely sensed imagery equally contributes to the unmixing result. However, some researchers doubted this assumption since weighted SMA (WSMA) results had outperformed the results of simple SMA in their studies (Chang and Ji, 2006; Somers et al., 2009). This can be attributed to two major reasons: 1) existence of within-class variability complicates endmember separability (Barducci and Mecocci, 2005); and 2) estimated error is positively related to the mixing scale of endmembers (Somers et al., 2009). With the second reason, estimation results are mainly affected by wavebands with the highest reflectance/radiance while disregarding wavebands with low values (Somers et al., 2009). Somers et al. (2009) highlighted that significant fraction estimation errors might appear when the difference in the reflected energy among wavebands is ignored.

Several researchers have discussed the feasibility of applying WSMAs in their studies. Chang and Ji (2006) explored three types of weighted matrices in the unmixing model, expanding the abundance-constrained linear spectral mixture analysis. Liu et al. (2013) extended the WSMA proposed by Chang and Ji (2006) to a kernel-based linear spectral mixture analysis by employing a kernelized weighting matrix. Somers et al. (2009) analyzed the relationship between the endmember variability and reflected energy and examined their impacts on fraction estimate accuracy. The authors summarized that a waveband with the highest reflected energy contributes more to the spectral variability of fraction estimates. With this discovery, they proposed a two-step WSMA to address the endmember variability in agricultural production systems. A band weighting method was proposed by Pan et al. (2005) which assigned weighting scores based on how remarkable an edge was relative to its corresponding boundary. Results from the

abovementioned studies demonstrated the superior performance of weighted models compared to unweighted counterparts.

However, more attentions should be paid to WSMAs, as they have not been discussed adequately and few researchers have employed WSMA in their studies. The reasons for applying a WSMA are still not clear. There is no doubt that accuracy improvement can be achieved according to previous studies. These improvements, however, may be limited to specified study areas and data sources. Chang and Ji (2006) and Liu et al. (2013) focused on applying the weighted matrix on an abundance-constrained linear spectral model. The study area they employed included forests and farmlands, where endmember variability is relative low compared to urban regions. Somers et al. (2009) highlighted the capability of WSMA in vegetated areas. Study sites with more spectral variability, such as areas containing both impervious surfaces areas (ISAs) and vegetation, have not been explored yet. To examine the effectiveness of WSMA in urban environments, the Vegetation-High albedo-Low albedo (V-H-L) model proposed by Small (2001) was adopted. This model assumed that most of the urban regions consist of vegetation (tree and grass), high albedo areas (cloud, sand, concrete), and low albedo areas (asphalt, water etc.). Land cover classes of commercial areas, parking lots, residential areas, and roads can be categorized as one component in the V-H-L model. Further, cities located in humid area are mostly covered by vegetation and ISA, with only a few areas of sand and soil. Therefore, when water areas were masked, the V-H-L model can be simplified as Vegetation-High albedo impervious surface area-Low albedo impervious surface area (V-ISAh-ISAl) model in urban environments with a humid climate. This study aims to examine the performances of WSMA and unweighted SMA models in urban environments. To reach this objective, existing and potential weighting schemes were tested 100 times using different endmember classes' spectra. Accuracies of corresponding weighting schemes

were evaluated using mean absolute error (MAE). Paired-samples T test was employed to examine whether there are significant differences between weighted and unweighted schemes.

The next section introduces the background of SMA and weighting schemes. Section 3 presents two experiments in Janesville, WI and in Asheville, NC, USA respectively. Weighting scores as well as WSMA results are also reported in Section 3. Finally, discussion and conclusions are provided in Sections 4 and 5 respectively.

2.2 Background

2.2.1 Weighted Spectral Mixture Analysis

Spectral mixture analysis assumes that the spectra of a mixed pixel is a combination of several pure land cover classes' spectra or endmembers (Adams et al., 1995; Roberts et al., 1998). The Spectral mixture analysis model can be expressed as Equation (5).

$$R_k = \sum_{j}^{n} f_j \times R_{k,j} + \varepsilon_k \tag{5}$$

where R_k is the spectral reflectance of a mixed pixel on band *k*; f_j is the fraction of endmember *j* within the pixel; $R_{k,j}$ is the spectral reflectance of endmember *j* on band *k*; ε_k is the error of band *k*; *n* is the number of endmembers. For a fully constrained SMA, two constraints, summation to one ($\sum_{j}^{n} f_j = 1$) and nonnegativity ($0 \le f_j \le 1$), should be met. Generally, the process of solving the least squares error estimation is to find out the smallest ε_k (Barducci and Mecocci, 2005). Thus, Equation (1) can be interpreted as Equation (6).

$$\sum_{k=1}^{z} \varepsilon_k{}^2 = \sum_{k=1}^{z} \left(\sum_{j}^{n} (f_j \times R_{k,j}) - R_k \right)^2 \tag{6}$$

where *z* is the number of spectral band. Weighting vector $\boldsymbol{A}$ can be introduced to Equation (2) in

order to address the problem of unequal contribution of wavebands (Chang and Ji, 2006; Somers et al., 2009). Equation (7) shows the weighing vector-added format.

$$\sum_{k=1}^{z} \varepsilon_k{}^2 = \sum_{k=1}^{z} \left(A_{k,j} \times \sum_{j}^{n} (f_j \times R_{k,j}) - R_k \right)^2 \quad (7)$$

Mean absolute error (MAE), which compares the estimated fraction to the reference fraction, was employed to evaluate the performances of the unmixing results. Calculation of MAE is presented in Equation (8).

$$\text{MAE} = \sum_{i=1}^{m} ABS(f_{e,i} - f_{r,i}) / m \quad (8)$$

where $f_{e,i}$ and $f_{r,i}$ are the estimated and reference fraction of sample *i* respectively; *m* is the number of samples.

2.2.2 Weighting Schemes

Five existing weighting schemes, including Shannon Entropy-weighted method [Entropy, (Wang and Bao, 2007)], reflected energy fixed weighting vector [REFWV, (Somers et al., 2009)], InStability Index-based weighting method [ISIb, (Somers et al., 2009)], combined weighting vector [WV, (Somers et al., 2009)], and within-class variance [V_W, (Chang and Ji, 2006)], were implemented in this study based on published research papers. We also developed five potential weighting schemes as extensions of existing weighting methods, including between-class variance [V_B, (Chang and Ji, 2006)], total-class variance [V_T, (Rogerson, 2014)], inversed Optimum Index Factor (IOIF), mean (Mean), and standard deviation (SD). Details of computing the existing weighting vectors are shown in Equations (9-14) and the potential weighting schemes are displayed in Equations (15-20).

2.2.2.1 Weighting schemes selected for investigation

Shannon entropy is an established variability measurement in information theory (Wang and Bao, 2007). It has been widely employed in a number of research fields, such as social sciences, physics, remote sensing, etc. In remote sensing, Shannon's entropy indicates the scale of information of each band (Wang and Bao, 2007). Theoretically, a band containing more energy may achieve a higher entropy value. Thus, Shannon entropy is widely employed to be a weighting scheme. The detailed calculation of Shannon entropy (*E*) is shown in Equation (9).

$$E_k = -\sum_{i=1}^{m} P(R_{k,i}) \log_2 P(R_{k,i}) \quad (9)$$

where E_k is the entropy value of band *k*, *m* is the number of selected samples, $R_{k,i}$ is the sample *i*'s reflectance value in band *k*, $P(R_{k,i})$ is the probability of obtaining a particular reflectance value $R_{k,i}$. It can be expressed as $P(R_{k,i}) = f(R_{k,i}) / \sum_{j=1}^{m} f(R_{k,j})$ (Cloude and Pottier, 1997), where $f(R_{k,i})$ is the frequency of $R_{k,i}$, $\sum_{j=1}^{m} f(R_{k,j})$ is the total frequency of all reflectance values.

Reflected energy fixed weighted vector (REFWV) (R_k in equation 10) is a weighting method proposed by (Somers et al., 2009). It utilizes the maximum value of reflectance in each band divided by the mean value of the corresponding band to keep the relative relationship between endmember classes as well as erasing variability between wavebands (Somers et al., 2009). Detailed calculation can be expressed in Equation (10).

$$R_k = R_{\max,k} / R_{mean,k} \quad (10)$$

R_k is the reflected energy fixed weighted value of band *k*; $R_{\max,k}$ and $R_{mean,k}$ are the maximum and mean reflectance of band *k* respectively.

InStability index-based (ISIb) (I_k in equations 7 and 8) weighting method, Equation (11), was

also proposed by (Somers et al., 2009) to address vegetation endmember variability. It takes both within-class and between-class variability into account. The ratio between the sum of endmember classes' standard deviations and the average Euclidean distance between endmember classes' means are viewed as the weighting scores of the corresponding bands. Equation (11) is calculated based on two land cover classes.

$$I_k = 1/ISI_k = 1/\left(\frac{s_{k,x} + s_{k,y}}{\left|\bar{R}_{k,x} - \bar{R}_{k,y}\right|}\right) = \frac{\left|\bar{R}_{k,x} - \bar{R}_{k,y}\right|}{s_{k,x} + s_{k,y}} \quad (11)$$

where $\bar{R}_{k,x}$ and $\bar{R}_{k,y}$ are the mean reflectance of class x and y in band *k* separately. $s_{k,x}$ and $s_{k,y}$ are the corresponding standard deviation of class *x* and *y* in band *k*. For a more than 2-endember scheme, equation (11) can be represented as Equation (12):

$$I_k = 1/ISI_k = 1/\left(\frac{2}{n \times (n-1)} \sum_{x}^{n-1} \sum_{y=x+1}^{n} \frac{s_{k,x} + s_{k,y}}{\left|\bar{R}_{k,x} - \bar{R}_{k,y}\right|}\right) \quad (12)$$

where *n* is the number of endmembers.

The combined weighting vector (WV, W_k in equation 13) is calculated as reflected energy fixed weighted vector multiplies the ISIb (Somers et al., 2009). It is shown in Equation (13).

$$W_k = REFWV_k * ISIb_k \quad (13)$$

Within-class variance (V_W) describes the variability of each land cover class. Chang and Ji (2006) employed the within-class variance as the weighting vector in the weighted abundance constrained linear spectral mixture analysis. It can be expressed as Equation (10).

$$(V_W)_k = \sum_{j=1}^{n} \sum_{i=1}^{m_j} (R_{k,i} - \bar{R}_{k,j})^2 \quad (14)$$

Where $(V_W)_k$ is the within-class variance weighting vector's value in band *k*. $\bar{R}_{k,j}$ is the mean reflectance of land cover class *j* in band *k*. $R_{k,i}$ represents a particular reflectance of sample *i* of corresponding land cover class *j* in band *k*. m_j is the number of samples in class *j*.

2.2.2.2 Potential weighting schemes

In addition to the existing weighting schemes, five potential weighting schemes were also proposed based on wavebands' variances and energies/information. Waveband's variance-based potential weighting schemes include between-class variance (V_B), total-class variance (V_T), and standard deviation (SD), while the energy/information-based potential weighting schemes contain the inversed optimum index factor (IOIF) and mean (Mean).

2.2.2.2.1 Variance-based potential weighting schemes.

Waveband's variance, such as within-class variance, has been verified for use as a weighting scheme for SMA (Chang and Ji, 2006). In addition to within-class variance, between-class variance and total-class variance were also used to describe the variance of a data set. However, they have not been discussed in most previous studies. Hence, between-class variance (VB) and total-class variance (VT) are explored in this study. They are written as Equations (15) and (16) respectively.

$$(V_{\mathrm{B}})_k = \sum_{j=1}^{n} m_j (\bar{R}_{k,j} - u_k)^2 \qquad (15)$$

where $(V_{\mathrm{B}})_k$ is the between-class variance weighting vector's value in band *k*. m_j is the number of sample in land cover class *j*. u_k is the mean reflectance of all classes in band *k*. $\bar{R}_{k,j}$ represents the mean reflectance of land cover class *j* in band *k*.

$$(V_{\mathrm{T}})_k = (V_{\mathrm{W}})_k + (V_{\mathrm{B}})_k \qquad (16)$$

where $(V_{\mathrm{T}})_k$ is the total-class variance weighting vector's value in band k.

Further, standard deviation (SD, S_k in equation 17), the square root of the variance, is another method to measure the divergence of a data set. It can be expressed as Equation (17).

$$S_k = \sqrt{\sum_{i=1}^{m} (R_{k,i} - \bar{R}_{k,i})^2 / m} \quad (17)$$

where $R_{k,i}$ and $\bar{R}_{k,i}$ are the reflectance of sample *i* and mean reflectance in band *k* respectively. *m* is the number of samples of the corresponding class.

2.2.2.2.2 Information/Energy-based potential weighting schemes.

Waveband's information/energy may be another factor that affect the accuracy of SMA. A number of scholars state that the least square error method adopted in SMA ignores the bands with low reflectance/radiance values as determined by wavebands with relatively high reflectance/radiance (Somers et al., 2009). Therefore, parameters that measure a waveband's information/energy information can be viewed as potential weighting schemes to minimize the unmixing error. Two weighting schemes that evaluate the waveband's information/energy, IOIF and Mean, are employed in this study.

The purpose of OIF (***O*** in equation 18) is to find a three-band combination which can maximize the overall information content (Chavez et al., 1982; Qaid and Basavarajappa, 2008). It is calculated based on the ratio between total variance and total correlation of any two bands (Equation 18). Bands with high variances and low pair-wise correlation may match the purpose of OIF.

$$\boldsymbol{O} = Max\left[\frac{\sum_{k=1}^{z}\sigma(k)}{\sum_{j=1}^{z}|r(j)|}\right] \quad (18)$$

where $\sigma(k)$ is the standard deviation of k^{th} band; $|r(j)|$ is the absolute correlation coefficient between any two bands; *z* is the number of bands.

According to Chavez et al. (1982), the three bands with the highest OIF values should contain

the majority of information. The remaining bands, accordingly, contain the smallest amount of information. Hence, the calculation of OIF, to a certain degree, can indicate the amount of information of selected bands and remaining bands. In this research, an inversed OIF (IOIF) that expanded the OIF calculation from 3 bands to *z-1* bands (*z* is the number of bands) is proposed. Since the amount of information of all bands is consistent, the more information the *z-1* bands contain, the less amount of information the remaining band will include. Therefore, the remaining band contains more information when the *z-1* bands' OIF value is low. Thus, the reciprocal of *z-1* bands' OIF value can be used to indicate the amount of information in the remaining band. IOIF (F_k) can be expressed as Equation (19).

$$F_k = 1 / \frac{\sum_{i=1, i\neq k}^{z} \sigma(i)}{\sum_{j=1, j\neq k}^{z} |r(j)|} \tag{19}$$

where I_k is the IOIF value of band *k*; $\sigma(i)$ is the standard deviation of band *i*; $|r(j)|$ is the correlation coefficient.

The reflectance/radiance of each band could also affect SMA results, and the bands with a higher reflectance/radiance values may play a larger role. Therefore, the mean value of each band is employed to examine its possibility to be a weighting scheme. The mean value of each band can be calculated as Equation (20).

$$\text{Mean}_k = \sum \frac{R_k}{m} \tag{20}$$

where R_k is the radiance/reflectance of band *k*; and *m* is the total number of samples.

For a clear illustration, all aforementioned weighting schemes are summarized in

Table *1*.

Table 1 weighting schemes

Schemes	Expression	Reference
Entropy	$-\sum_{i=1}^{m} P(R_{k,i}) \log_2 P(R_{k,i})$	Wang and Bao (2007)
REFWV	$R_{\max,k} / R_{mean,k}$	Somers et al. (2009)
ISIb	$1/(\frac{2}{n\times(n-1)}\sum_{x}^{n-1}\sum_{y=x+1}^{n}\frac{s_{k,x}+s_{k,y}}{\left\|\bar{R}_{k,x}-\bar{R}_{k,y}\right\|})$	Somers et al. (2009)
WV	$R_k * I_k$	Somers et al. (2009)
V_W	$\sum_{j=1}^{n}\sum_{i=1}^{m_j}(R_{k,i}-\bar{R}_{k,j})^2$	Chang and Ji (2006)
V_B	$\sum_{j=1}^{n} m_j(\bar{R}_{k,j}-u_k)^2$	Chang and Ji (2006)
V_T	$(V_W)_k+(V_B)_k$	Rogerson (2014)
SD	$\sqrt{\sum_{i=1}^{m}(R_{k,i}-\bar{R}_{k,i})^2/m}$	
IOIF	$1/\frac{\sum_{i=1,i\neq k}^{z}\sigma(i)}{\sum_{j=1,j\neq k}^{z}\left\|r(j)\right\|}$	Chavez et al. (1982)
Mean	$\sum\frac{R_k}{m}$	

2.3 Experiments

2.3.1 Study areas and data sources

The cities of Janesville (Wisconsin), and Asheville (North Carolina) in the United States were selected as the study areas (Figure 1). Janesville is within the Great Lakes region (humid continental climate) with a geographic area of 80.95 km^2. It is dominated by land cover classes of ISA (e.g. roof, sidewalk, road, and parking lot) and vegetation (e.g. trees and grass). Single-family houses are distributed along streets, surrounding by lawns. Industrial areas and freeways can also be found in the study area. In addition to Janesville, Asheville was selected to examine whether consistent results can be obtained. Asheville is in western North Carolina, and has a similar landscape with Janesville. It has a humid subtropical climate with a cooler summer compared to eastern cities in the state. The area of Asheville is 117.2 km^2 with an estimated population of 83,393 in 2010.

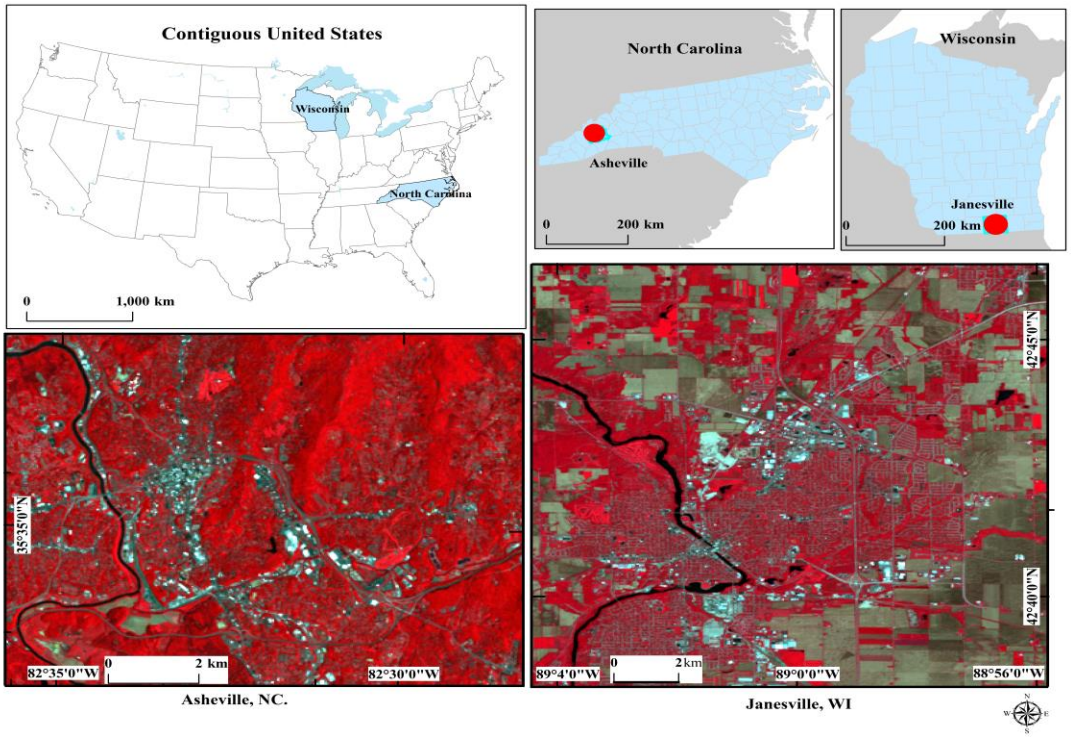

Figure 1 Study areas of Janesville, WI and Asheville, NC, USA.

A scene of Landsat 8 Operational Land Imager (OLI) acquired on June 3rd, 2014 and a scene of Landsat 5 Thematic Mapper (TM) acquired on June 2nd, 2009 were downloaded from the U.S. Geological Services (USGS) website for the study areas of Janesville and Asheville respectively. Image preprocessing, such as Radiance calibration, atmospheric correction, were applied on OLI and TM images. Historical Google Earth Pro images of Janesville acquired on June 12th, 2014 and of Asheville acquired on May 30th, 2009 were employed as the references to verify the accuracy of the unmixing results. Soil was not taken into consideration since the amount of soil is limited. Thus, soil was masked before SMA using a support vector machine (SVM) classification.

2.3.2 Sample selection

Two types of samples: training samples and testing samples, were selected. Training samples were pure pixels selected within the preprocessed images. They were chosen directly from the comparison referenced images to avoid erroneous pixels. Generally, training samples were only selected within large pure land cover classes. For example, the training samples of vegetation were selected from forest areas and large-scale grasslands. Trees or grass within residential areas were avoided to prevent the selection of mixed pixels. Similarly, training samples of impervious surface areas were selected in large shopping malls or parking lots. The numbers of vegetation samples (V), high albedo impervious surface area samples (ISAh), and low albedo impervious surface area samples (ISAl), were 40, 40, 40 in Janesville and were 50, 50, 50 in Asheville.

Testing samples (64 samples for Janesville and 61 samples for Asheville) were randomly selected (including pure and mixed pixels) within the study area to verify the accuracy of unmixing results. Each sample was designed as 90m ×90m (3pixels×3pixels) to reduce the geometric error impact from data acquisition.

Three spectra libraries were constructed using land cover class training samples respectively.

Thus, each spectral library contains 40 spectra in Janesville and 50 spectra in Asheville.

2.3.3 SMA and accuracy assessment

In this study, each weighted scheme as well as unweighted scheme were tested 100 times. For each test, we randomly selected one spectrum from each spectral library as the endmember for SMA. Therefore, 100 spectra combinations were selected under the V-ISAh-ISAl endmember model. All weighting schemes as well as the unweighted scheme employed the same endmember set in each test to provide a comparable result. Fully constrained linear spectral mixture analysis was applied for each test to derive the fractions of vegetation, high albedo impervious surface area, low albedo impervious surface area, and soil.

Mean absolute error (MAE) of ISA was employed to evaluate SMA performance. Estimated fractions of ISA were combined by fractions of ISAh and ISAl in the same pixel. Referenced fractions of ISA in google earth images were extracted through digitizing the corresponding areas within samples (Figure 2).

Figure 2 Calculation of referenced ISA

2.4 Results

2.4.1 Weighting vectors

Weighting schemes were constructed through four types of samples: high albedo ISA samples (ISAh), low albedo ISA samples (ISAl), vegetation samples (V), and all samples (ALL, including ISAh, ISAl, and V samples). The original weighting scores of each scheme are shown in Table 2 and Table 3. Since weighting schemes of ISIb, WV, V_W, V_B, V_T, involve more than one land cover classes, they were only constructed in ALL samples.

Table 2 weighting scores of Janesville

Samples	Schemes	B1	B2	B3	B4	B5	B6	B7
V	Entropy	1.100	0.980	1.380	1.370	3.510	2.130	1.620
	REFWV	1.310	1.400	1.290	1.640	1.200	1.270	1.380
	SD	0.004	0.004	0.007	0.005	0.033	0.013	0.008
	IOIF	163.93	164.06	171.19	167.86	313.30	210.49	183.35
	Mean	0.040	0.030	0.060	0.030	0.430	0.170	0.070
ISAh	Entropy	4.775	4.844	4.538	4.853	4.758	4.474	4.709
	REFWV	1.713	1.738	1.659	1.689	1.716	1.331	1.547
	SD	0.117	0.119	0.123	0.132	0.143	0.083	0.160
	IOIF	12.675	12.606	12.564	12.719	13.194	14.849	16.558
	Mean	0.394	0.397	0.427	0.445	0.457	0.561	0.496
ISAl	Entropy	2.161	2.196	2.416	2.633	3.158	2.870	2.588
	REFWV	1.442	1.482	1.483	1.529	1.678	1.411	1.388
	SD	0.011	0.011	0.013	0.015	0.026	0.021	0.017
	IOIF	103.97	104.04	102.80	103.84	127.26	125.82	117.81
	Mean	0.074	0.065	0.068	0.071	0.090	0.088	0.079
ALL	Entropy	4.020	3.962	3.704	4.247	5.051	4.581	3.875
	REFWV	4.328	4.562	4.080	4.478	2.207	2.763	3.731

	ISIb	2.508	2.544	2.641	2.534	2.173	4.545	2.352
	WV	10.86	11.60	10.77	11.35	4.79	12.56	8.78
	V_W	0.014	0.014	0.015	0.018	0.022	0.008	0.026
	V_B	3.101	3.288	3.446	4.187	3.169	4.572	4.511
	V_T	3.115	3.302	3.461	4.205	3.191	4.579	4.537
	SD	0.173	0.178	0.183	0.200	0.174	0.203	0.214
	IOIF	9.759	9.797	9.796	10.007	11.965	10.854	10.840
	Mean	0.156	0.151	0.174	0.168	0.355	0.270	0.206

Table 3 weighting scores of Asheville

Samples	Schemes	B1	B2	B3	B4	B5	B6
V	Entropy	0.881	1.240	0.958	3.295	2.579	1.637
	REFWV	2.870	1.378	1.419	1.124	1.249	1.480
	SD	0.003	0.005	0.002	0.029	0.015	0.007
	IOIF	0.007	0.007	0.007	0.013	0.007	0.006
	Mean	0.004	0.028	0.015	0.425	0.164	0.060
ISAh	Entropy	4.229	4.821	4.999	4.974	4.261	4.543
	REFWV	1.335	1.945	1.819	1.607	1.349	2.302
	SD	0.094	0.150	0.150	0.144	0.096	0.161
	IOIF	0.001	0.001	0.001	0.001	0.001	0.001
	Mean	0.333	0.424	0.432	0.462	0.419	0.362
ISAl	Entropy	3.523	3.723	3.765	3.888	3.736	3.418
	REFWV	2.080	2.151	2.027	1.885	1.727	1.831
	SD	0.040	0.048	0.051	0.063	0.047	0.034
	IOIF	0.003	0.003	0.003	0.004	0.003	0.003
	Mean	0.102	0.128	0.135	0.182	0.170	0.144
ALL	Entropy	4.399	4.775	4.754	5.336	4.649	4.731
	REFWV	3.044	4.266	4.047	2.083	2.252	4.409

	ISIb	2.318	1.899	2.034	0.521	0.260	1.554
	WV	7.055	8.100	8.230	1.086	0.585	6.850
	V_W	0.512	1.219	1.226	1.254	0.571	1.327
	V_B	2.862	4.249	4.595	2.308	2.116	2.414
	V_T	3.375	5.468	5.821	3.561	2.687	3.742
	SD	0.150	0.192	0.198	0.155	0.134	0.158
	IOIF	0.012	0.013	0.012	0.027	0.015	0.014
	Mean	0.146	0.194	0.194	0.356	0.251	0.189

Weighting patterns are diverse when constructed from different samples. Highlighted and suppressed bands are different from different samples. For example, Entropy highlights near infrared (NIR, band 5 of OLI) in V, ISAl, and ALL sample, but enhances blue band (band 2 of OLI) and red band (band 4 of OLI) in ISAh samples in Janesville. In addition, the scale of weighting scores varies from schemes to schemes. The highest scale of weighting score is IOIF in V and ISAl samples, the weighting scores in these weighting schemes are larger than 100 in Janesville but are small in Asheville. The scores of SD, Mean, and V_W are also very small scale. Most of them are less than 0.5, and scores in V and ISAl samples can only reach 0.1. Weighting scores of Entropy, REFWV, V_B, and V_T are between 1 to 10.

To compare differences between different weighting schemes, all weighting scores were normalized and classified into five categories: Highly Emphasized (0.8-1), Medium Emphasized (0.6-0.8), Slightly Changed (0.4-0.6), Medium Compressed (0.2-0.4), and Highly Compressed (0-0.2) (Table 4 and Table *5*).

Table 4 Normalized weighting scores classification of Janesville

Samples	Schemes	Highly Emphasized	Medium Emphasized	Slightly Changed	Medium Compressed	Highly Compressed

V	Entropy	B5		B6	B7	B1 B2 B3 B4
	REFWV	B4		B2 B7	B1 B3	B5 B6
	SD	B5			B6	B1 B2 B3 B4 B7
	IOIF	B5			B6	B1 B2 B3 B4 B7
	Mean	B5			B6	B1 B2 B3 B4 B7
ISAh	Entropy	B2 B4	B1 B5 B7			B3 B6
	REFWV	B1 B2 B3 B4 B5		B7		B6
	SD	B7	B4 B5	B1 B2 B3		B6
	IOIF	B7		B6		B1 B2 B3 B4 B5
	Mean	B6	B7		B4 B5	B1 B2 B3
ISAl	Entropy	B5	B6	B4 B7	B3	B1 B2
	REFWV	B5		B4	B2 B3	B1 B6 B7
	SD	B5	B6	B7	B4	B1 B2 B3
	IOIF	B5 B6	B7			B1 B2 B3 B4
	Mean	B5 B6		B7	B1 B4	B2 B3
All	Entropy	B5	B6	B4	B1	B2 B3 B7
	REFWV	B1 B2 B4	B3 B7		B6	B5
	ISIb	B6				B1 B2 B3 B4 B5 B7
	WV	B2 B4 B6	B1 B3	B7		B5
	V_W	B7	B5	B3 B4	B1 B2	B6
	V_B	B6 B7	B4		B3	B1 B2 B5
	V_T	B6 B7	B4		B3	B1 B2 B5
	SD	B7	B4 B6		B3	B1 B2 B5
	IOIF	B5		B6 B7		B1 B2 B3 B4
	Mean	B5		B6	B7	B1 B2 B3 B4

Table 5 Normalized weighting scores classification of Asheville

Samples	Schemes	Highly Emphasized	Medium Emphasized	Slightly Changed	Medium Compressed	Highly Compressed
V	Entropy	B4	B5		B6	B1 B2 B3
	REFWV	B1			B6	B2 B3 B4 B5
	SD	B4		B5		B1 B2 B3 B6
	IOIF	B4				B1 B2 B3 B5 B6
	Mean	B4			B5	B1 B2 B3 B6
ISAh	Entropy	B3 B4	B2	B6		B1 B5
	REFWV	B6	B2	B3	B4	B1 B5
	SD	B2 B3 B6	B4			B1 B5
	IOIF	B6			B5	B1 B2 B3 B4
	Mean	B4	B2 B3 B5		B6	B1
ISAl	Entropy	B4	B2 B3 B5		B1	B6
	REFWV	B1 B2	B3		B4 B6	B5
	SD	B4		B2 B3 B5		B1 B6
	IOIF	B4			B6	B1 B2 B3 B5
	Mean	B4 B5		B3 B6	B2	B1
All	Entropy	B4		B2	B3 B5 B6	B1
	REFWV	B2 B3 B6		B1		B4 B5
	ISIb	B1 B3	B2 B6			B4 B5
	WV	B1 B2 B3 B6				B4 B5
	V_W	B2 B3 B4 B6				B1 B5
	V_B	B2 B3			B1	B4 B5 B6
	V_T	B2 B3			B1 B4 B6	B5
	SD	B2 B3			B1 B4 B6	B5
	IOIF	B4			B5	B1 B2 B3 B6
	Mean	B4		B5	B2 B3 B6	B1

Note: B1-B6 in TM5 image are equal to B2-B7 in OLI image. Thus, B1-B6 in Asheville are equal to B2-B7 in Janesville.

(1) Vegetation samples (V). The weighting patterns are similar between the two study areas in V sample. The emphasized band in V samples is almost the same except REFWV. All other weighting schemes highlight near infrared red (NIR) while REFWV emphasizes red (Janesville) and blue (Asheville) band. In scheme of REFWV, the near infrared band, is compressed, acquiring the lowest score among all bands.

(2) High albedo ISA samples (ISAh). Weighting scores as well as highlighted bands vary from schemes to schemes. Entropy highly enhances the red band. At the same time, the short wave infrared band 1 (SWIR1, band 5 in TM) is highly compressed. SWIR1 is compressed by schemes of SD, REFWV, and Entropy. IOIF's weighting scores increase with the band number.

(3) Low albedo ISA samples (ISAl). Almost all the weighting schemes have the same highlighted NIR. For other bands, especially the visible bands, their scores are much lower than short wave infrared (SWIR).

(4) All (Vegetation- high albedo ISA-low albedo ISA) samples. Entropy, IOIF, and Mean have a similar pattern, assigning a higher score to NIR and compressing blue band. On the contrary, REFWV and WV emphasize green and red bands while they both compress NIR band. V_W emphasizes NIR and SWIR2 (band 6 in TM) and strongly compresses SWIR1.

2.4.2 MAE

All weighting schemes as well as the unweighted scheme (all weighting scores are equal to one) were applied to fully constrained spectral mixture analysis. Mean absolute error (MAE) between the estimated and referenced fractions was utilized to evaluate each model's accuracy. The distribution of MAE of each scheme was described in boxplot (Figure 3 and 4. Paired-samples T tests (Table 6 and Table *7*) were employed to examine if there were significantly different means between each weighted and unweighted scheme's MAE. In addition, the number of improved tests

was counted. The improved test was referred to the test which the weighted scheme has a smaller MAE compared to the unweighted scheme. The improved MAEs as well as improved percentages were calculated to explore the scale of improvement (Table 6 and Table *7*).

The descriptive MAE statistics for each scheme are shown in Figures 3 and 4. Median MAEs of all weighting schemes as well as unweighted scheme are larger than 0.1 in Janesville and many median MAEs are larger than 0.15 in Asheville. Only a few weighting schemes improved the accuracy when compared to the unweighted SMA.

The range of MAEs are different in each weighting scheme (Figure 3 and Figure *4*). Generally, ranges of MAE in Janesville are smaller than the ranges for Asheville. The range of unweighted scheme is about 0.1 in Janesville and is about 0.22 in Asheville. Many weighting schemes have similar or slightly larger ranges compared to unweighted scheme in both study areas.

It can be seen from Figure 3 and Figure *4* that, weighting schemes in Janesville have smaller maximum MAEs but larger minimum MAEs compared to the schemes in Asheville. Many minimum MAEs in Janesville are larger than 0.1 and small than 0.2. On the contrary, minimum MAEs in Asheville can be less than 0.1 and the maximum MAE can reach 0.3.

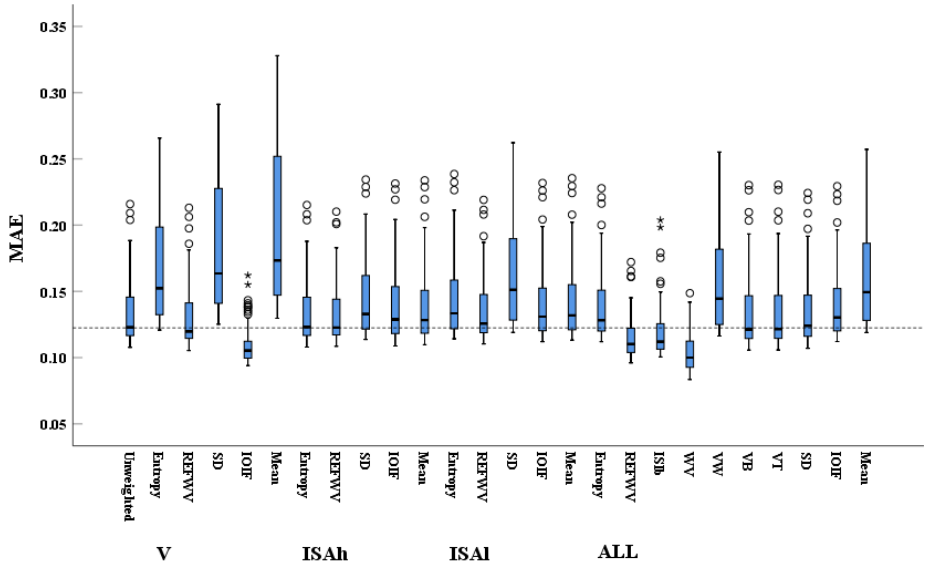

Figure 3 Boxplot of MAEs in Janesville. The Entropy- Mean from left side to right side belongs to V, ISAh, ISAl, and ALL samples respectively.

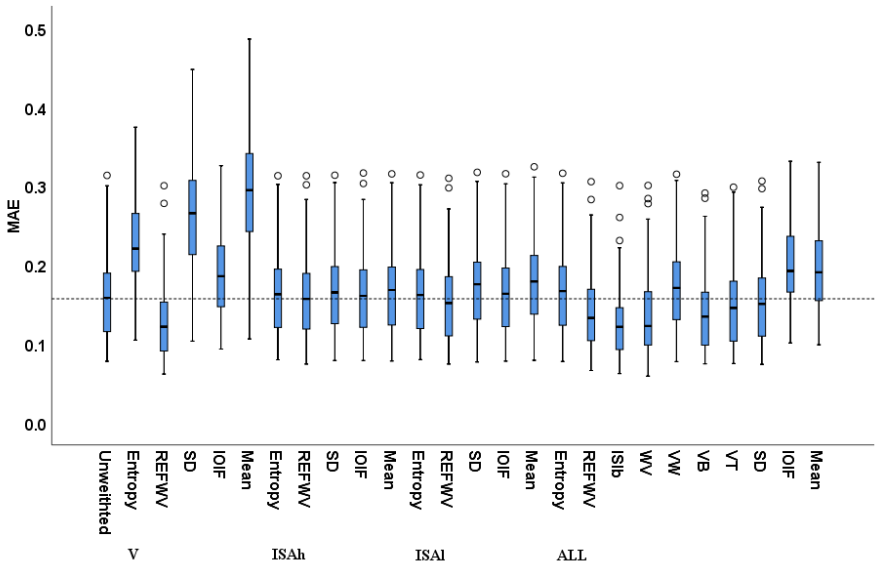

Figure 4 Boxplot of MAEs in Asheville. The Entropy- Mean from left side to right side belongs to V, ISAh, ISAl, and ALL samples respectively.

As depicted in Figure 3 and Figure *4*, several weighting schemes, including IOIF in V samples (in Janesville area), REFWV in V sample, REFWV, ISIb, and WV in All samples, showed that their accuracies are better than the unweighted scheme. To statistically prove their performances, paired-samples T tests were employed to analyze their differences (Table 6 and Table *7*). In Table 6 and Table *7*, the third column (Mean Difference (Unweighting-weighted)) shows the mean MAE difference between each weighting scheme and unweighted scheme. Negative values in the third column indicates that the mean MAE of weighted scheme was larger than the unweighted scheme. The fourth column shows the t values and the sixth column indicates the significances of differences.

Mean MAEs of REFWV and IOIF (only in Janesville) in V samples as well as REFWV, ISIb, and WV in All samples are lower than the mean MAE of unweighted scheme. Their p values are

much lower than 0.025 values (Sig.(2-tailed) in Table 6 and Table 7), indicating that their means are statistically different from the unweighted scheme's. Thus, these statistics prove that the weighting schemes perform better than the unweighted SMA. Weighting schemes of REFWV in ISAh samples as well as V_B and V_T in ALL samples acquire slightly lower mean MAE compared to the unweighted scheme. Their p values, however, are larger than 0.05 in Janesville but are smaller than 0.05 in Asheville, which implies that their differences are not significant in Janesville but are significant in Asheville. All remaining weighting schemes' mean MAEs are larger than the unweighted scheme and their p values are equal to zero, illustrating that they weaken the SMA result significantly.

Moreover, the MAE of each test between weighted and unweighted schemes was compared and the number of tests that has a lower MAE than unweighted scheme was counted (Num. of improved test in Table 6 and Table *7*). Additionally, the average improved MAEs were calculated as well as their improved percentages among the outperformed tests. Results indicate that almost all the tests of REFWV and IOIF (only in Janesville) in V samples and REFWV, ISIb, and WV in ALL samples perform better than the unweighted scheme. In Janesville, the improvement of REFWV in V samples is limited with the averagely improved MAE of 0.0036 (2.7%). In contrast, REFWV in V sample in Asheville improved about 20% of the MAE. IOIF in V samples and REFWV, ISIb, and WV in ALL samples reduce the MAE by 19.12%, 13.76%, 10.51%, and 26.97% respectively in Janesville. Although more than 50% of the tests (71% in V_B, 69% in V_T, and 50% in SD) in V_B, V_T, and SD in ALL samples in Janesville have lower MAEs than the unweighted scheme, their improvements are less than 1%, which is negligible. The average improvements in Asheville for the REFWV in V sample, REFWV, ISIb, and WV in ALL sample are larger than in Janesville. V_B, V_T, and SD in Asheville improved more by having higher average

improved MAEs as well.

Table 6 Statistical analysis between each weighting scheme and unweighted scheme in Janesville

Samples	Schemes	Paired Samples Test			Num. of improved test	Ave. improved (%)
		Mean Difference (Unweighted-Weighted)	t	Sig. (2-tailed)		
V	Entropy	-0.0329	-15.555	0.000	0	0
	REFWV	0.0036	18.044	0.000	99	2.7%
	SD	-0.0498	-15.020	0.000	0	0
	IOIF	0.0238	14.006	0.000	94	19.12%
	Mean	-0.0644	-14.331	0.000	0	0
ISAh	Entropy	-0.0001	-4.089	0.000	32	0.15%
	REFWV	0.0002	1.283	0.203	45	1.06%
	SD	-0.0109	-14.551	0.000	0	0
	IOIF	-0.0058	-10.367	0.000	3	0.88%
	Mean	-0.0055	-10.701	0.000	3	0.09%
ISAl	Entropy	-0.0107	-15.068	0.000	1	0.69%
	REFWV	-0.0027	-16.723	0.000	1	0.45%
	SD	-0.0279	-14.947	0.000	0	0
	IOIF	-0.0077	-14.671	0.000	0	0
	Mean	-0.0093	-14.874	0.000	0	0
ALL	Entropy	-0.0060	-16.408	0.000	1	0.36%
	REFWV	0.0179	15.196	0.000	98	13.76%
	ISIb	0.0135	12.249	0.000	97	10.51%
	WV	0.0287	9.983	0.000	84	26.97%
	V_W	-0.0220	-14.354	0.000	0	0
	V_B	0.0003	0.642	0.522	71	1.68%
	V_T	0.0001	0.190	0.850	69	1.68%

	SD	-0.0011	-4.089	0.000	50	0.59%
	IOIF	-0.0070	-15.588	0.000	0	0
	Mean	-0.0266	-15.383	0.000	0	0

Table 7 Statistical analysis between each weighting scheme and unweighted scheme in Asheville

Samples	Schemes	Paired Samples Test			Num. of improved test	Ave. improved (%)
		Mean Difference (Unweighted-Weighted)	t	Sig. (2-tailed)		
V	Entropy	-0.0675	-14.636	0.000	1	0.19%
	REFWV	0.0311	18.552	0.000	98	20.10%
	SD	-0.1055	-14.697	0.000	1	1.02%
	IOIF	-0.0317	-11.116	0.000	1	2.38%
	Mean	-0.1315	-16.138	0.000	0	0
ISAh	Entropy	-0.0035	-11.955	0.000	10	0.59%
	REFWV	-0.0013	-1.850	0.067	47	2.63%
	SD	-0.0067	-13.187	0.000	8	1.51%
	IOIF	-0.0039	-6.094	0.000	27	2.28%
	Mean	-0.0078	-12.995	0.000	4	0.79%
ISAl	Entropy	-0.0027	-10.733	0.000	8	0.61%
	REFWV	0.0048	15.658	0.000	97	3.13%
	SD	-0.0147	-11.063	0.000	6	1.51%
	IOIF	-0.0048	-13.037	0.000	2	1.47%
	Mean	-0.0216	-15.366	0.000	1	1.67%
ALL	Entropy	-0.0071	-13.395	0.000	2	1.72%
	REFWV	0.0172	9.292	0.000	84	14.00%

ISIb	0.0319	10.023	0.000	87	24.92%
WV	0.0206	4.053	0.000	67	30.11%
V_W	-0.0126	-14.291	0.000	6	1.65%
V_B	0.0192	14.548	0.000	96	12.83%
V_T	0.0106	11.640	0.000	95	7.23%
SD	0.0055	11.584	0.000	95	3.69%
IOIF	-0.0418	-11.907	0.000	1	2.48%
Mean	-0.0369	-13.033	0.000	1	1.08%

2.5 Discussion

Spectral mixture analysis (SMA) has been widely employed by researchers due to its simplicity and adequate accuracy (Wu and Murray, 2003). However, the assumption that each waveband has an equal weighting score needs more examination because of: 1) the existence of between- and within-class variability and 2) the correlation between unmixing error and scale of mixed signal (Barducci and Mecocci, 2005; Somers et al., 2009). These two limitations, especially the second one, affect the performance of SMA (Somers et al., 2009).

2.5.1 Which weighting scheme to select?

Several scholars have applied weighting scheme in remotely sensed image analysis, such as WSMA (Chang and Ji, 2006; Somers et al., 2009), band selection (Pan et al., 2005) and image enhancement (Ma et al., 2014). Results from these studies illustrate that weighting scheme is constructive and it can improve the performance of proposed models. Generally, a weighting scheme can be constructed based on variance or information/energy.

2.5.1.1 Variance-based weighting scheme

Variance, including the within- and between-class variance, as stated by Barducci and Mecocci (2005) that it complicates endmember separability. Consequently, it affects the result of SMA. However, simple form of variance, such as standard deviation, within-class variance, between-class variance, and total-class variance, cannot be viewed as weighting scheme directly since results demonstrated their poor performance in this study. Within-class variance, though proves its outperformance in Chang and Ji (2006)'s research, does not perform well in this study. Major reasons may be attributed to 1) spectral variability in different study areas and 2) different training samples. Chang and Ji (2006)'s study focused on vegetated landscapes. Their research area is located in the intersection between forest and glass land. Instead, we employed urban environments that contain one more land cover class: impervious surface area. Variance of ISA, to some degree, is larger than vegetation. ISA's spectral reflectance does not have a unique pattern. Mixing the ISA with the vegetation to construct a weighting scheme may lead to huge difference comparing to pure vegetation samples. Besides, as Chang and Ji (2006) stated that a good set of training samples is key to constructing a meaningful weighting scheme. Since study areas is differ, it is impossible to select the same training samples especially in different study regions with different landscapes. Therefore, the results of WSMA may be different between this study and Chang and Ji (2006)'s study.

Weighting schemes of WV and ISIb, though, are constructed by variance. They take both the between-class and within-class variance into account. Moreover, reflected energy is considered as well when the weighting scheme of WV is constructed. Through the analysis of the variance-based weighting schemes, it seems that the variance does affect the performance of WSMA. However, directly constructed variance-based schemes had limited ability to improve the unmixing accuracy.

Variance may need to be incorporated with other indices to construct an effective weighting scheme.

2.5.1.2 Information/energy-based weighting scheme

Some endmembers are more sensitive to specific wavebands because highly reflected land surface features contribute more to the SMA result (Somers et al., 2009). Based on this assumption, weighting schemes can be composed from waveband information/energy. Some scholars constructed a weighting vector by evaluating the contribution of a pixel to increase the spatial resolution (Ma et al., 2014). Other scholars also admit that spectral characteristics are key factors to impact the construction of weighting scheme(Pan et al., 2005). Some bands can be viewed as "good" bands since they can separate two land cover classes clearly by providing a remarkable edge along their boundaries. Thus, these bands are assigned higher weighting scores (Pan et al., 2005). However, these weighting schemes except Somers et al. (2009)'s REFWV and WV are not utilized for SMA. Further, the information based weighting schemes examined in this study do not demonstrate significant improvement. Of course, some of REFWV tests perform better than the unweighted scheme. But paired-samples T test results do not indicate any significant difference between them. Other information/energy based schemes, such as Mean, does not show an impressive improvement either. IOIF weighting schemes constructed by ISAh, ISAl, and ALL have similar results with Mean. However, IOIF created by vegetation samples highlight the capability of improving the SMA accuracy. That may be due to the smaller variability of vegetation compared to other land cover classes. They have a clear pattern of low spectral reflectance in blue and red band, and have a small peak in the green band and very high reflectance in near infrared and shortwave infrared bands. ISAs' reflectance varies more than for vegetation. They do not have a unique pattern. Further, their within-class variance is much larger than for vegetation.

2.5.2 Uncertainties of endmember selection

Unlike the studies of Chang and Ji (2006) and Somers et al. (2009), this research examined current and potential weighting schemes based on 100 tests using different spectra as endmembers. Though some studies have compared several weighting schemes with the unweighted scheme (Chang and Ji, 2006; Somers et al., 2009), they were only based on one test. The selection of endmembers, however, may introduce a lot of uncertainties. Researchers select the potential endmembers according to their background. Some of them select spectra from the spectral library, other may use *in situ* measured spectral reflectance, and some others may choose endmembers from imagery. Researchers may choose different spectra as endmembers even when they work on the same study area with the same data source. Moreover, endmember selection is one of the most important steps in SMA. Selecting different spectra as endmembers can affect the unmixing result directly. In this case, other researchers cannot repeat the previous studies' result because they use different spectra as endmembers. To avoid the uncertainties of endmember selection, we tested the same weighted and unweighted schemes 100 times by using randomly selected spectra in a corresponding spectral library. 100 times of repeated testing can cover most of the potential endmember selections. Thus, their results can reflect the true performance of each weighting scheme. Therefore, the WSMA's results can be more meaningful and reliable.

2.6 Conclusions

This study explored different weighting schemes and their performances. Five existing weighting vectors (including Shannon Entropy weighting method (Entropy), reflected energy fixed weighting vector (REFWV), InStability Index-based weighting method (ISIb), combined weighting vector (WV), within-class variance (V_W)) and five potential weighting schemes (e.g., between-class variance (V_B), total-class variance (V_T), inversed Optimum Index Factor (OIF),

mean (Mean), and standard deviation (SD)) were examined in Janesville, WI, USA and Asheville, NC, USA. Each weighting scheme was tested 100 times using different spectra with the V-ISAh-ISAl endmember model. Weighted and unweighted schemes' performances were evaluated by MAE. Then Paired-Samples T test was employed to analyze if there were significant differences of MAE between weighted and unweighted schemes. Analyses of results suggest several conclusions.

(1) REFWV, ISIb, and WV constructed by ALL samples illustrated significant improvement comparing to the unweighted scheme since statistical analysis indicated their significance with the p values of 0. These weighting schemes could be applied in analyzing urban environments with a three-endmember model (vegetation - high albedo impervious surface area - low albedo impervious surface area) to improve the performance of SMA. (2) Weighting scheme of IOIF, SD, V_B, and V_T, showed unstable performances in different study areas as they significantly performed better than the unweighted scheme in one study area but weakened the accuracy in another study area (p values were less than 0.05). (3) Some potential weighting schemes, such as Entropy, Mean, and V_W, seemed not to be necessary for SMA in urban/suburban areas. (4) Future weighting schemes would be better constructed with consideration of spectral variance since the better preforming schemes in this study were built with spectral variance.

CHAPTER 3 EXAMINING THE EFFECTIVENESS OF SPECTRALLY TRANSFORMED SPECTRAL MIXTURE ANALYSIS IN URBAN ENVIRONMENTS[2]

3.1 Introduction

Spectral mixture analysis (SMA) has become more and more attractive in remote sensing applications, especially for medium and coarse spatial resolution imagery. SMA assumes that a mixed pixel is constructed by several pure land cover types (endmembers). It aims to extract the land covers' fractions within a pixel using spectral mixture models. Results of SMA are physically meaningful fractions instead of possibilities. Therefore, it is widely employed in the field of forest services (Peddle et al., 2001), urban planning and management (Small and Lu, 2006; Small et al., 2005), land use and land cover change (Lu and Weng, 2006; Lu et al., 2006), water quality management (Tyler et al., 2006), geology (Drake et al., 1999), and others.

With the differences of physical construction, and atmospheric environment, the spectral signature of a specified land surface material may vary from different locations and periods while spectral signatures of different materials may be similar. The previous drawback is called within-class variability, indicating the spectral differences within a class. The second limitation is named between-class variability, meaning the spectral similarity in different classes. Large within-class variability and small between-class variability are major reasons for spectral confusion in remotely sensed imagery classification.

Many techniques, including spectral weighting, iterative mixture analysis, spectral feature selection, spectral modeling, and spectral transformation, can be employed to address the spectral variability (Somers et al., 2011). Spectral transformation, which changes the original spectra linearly and nonlinearly, is one of the widely applied approaches used in SMA to solve spectral

[2]Portions of this chapter have been submitted to *ASPRS Photogrammetric Engineering & Remote Sensing*, coauthored with Dr. Changshan Wu

variability problems. The major purpose of spectral transformation is to enhance spectral characteristics. With enhanced spectra, spectral variability is expected to be reduced within the same class and to be increased between different classes.

Many scholars have employed spectral transformation in their remote sensing applications. Wu (2004) proposed a normalized spectral mixture analysis (NSMA) to extract land use and land cover information in the city of Columbus, Ohio. Each band reflectance in the NSMA is divided by the mean reflectance of all bands. Results indicated that brightness variation were reduced and improvement could be acquired from the NSMA. Asner and Lobell (2000) applied a tie spectral transformation before estimating the fractions of vegetation and soil. All other band reflectance was subtracted by tie band (point). The authors concluded that significant variation of soil moisture, canopy architecture, leaf and litter area index, and tissue optics could be compressed by using the tied spectra, resulting in more accurate output from the unmixing process. Zhang et al. (2004) employed a second order derivative spectral unmixing (DSU) method in rock and lichen fractions estimation. They summarized that DSU is promising for fraction estimation using hyperspectral data. Similar studies include the research of Tsai and Philpot (1998), Laba et al. (2005), and Huguenin and Jones (1986). Debba et al. (2006) compared the results of first derivative and second derivative spectra in laboratory mineral applications. They concluded that higher-order derivatives contribute more to remote sensing images with higher signal-to-noise ratios. Li (2004) compared the discrete wavelet transform (DWT) with the principal component analysis (PCA). He found that DWT could increase more separability than the PCA, leading to improvement of fraction estimation. Similar conclusions were achieved from the studies of Bruce et al. (2002) and Zhang et al. (2006). Youngentob et al. (2011) assumed that continuum removal (CR) analysis can contribute to class separability through highlighting individual absorption features across a

normalized spectrum. They examined the performance of CR analysis using hyperspectral data, and results showed overall accuracy improvement. Principal component analysis [PCA, (Richards and Richards, 1999)], minimum noise fraction transform [MNF, (Green et al., 1988)], Tasseled Cap [TC, (Jensen and Lulla, 1987)], and independent component analysis [ICA, (Hyvärinen and Oja, 2000)] are commonly employed for land surface feature enhancement before applying SMA. Spectral characteristics of different land cover classes are highlighted in different output layers of these transformations. Many researchers employed these transformation techniques to assist the selection of endmember as well as to reduce the spectral within-class variability and to enhance between-class variability. Further, different spatial filters, such as low pass (LP), high pass (HP), Gaussian high pass (GHP), Gaussian low pass (GLP), are commonly employed to enhance the spectral characteristics' edges or to smooth the surface of remote sensing imagery.

Spectral transformation can be divided into two categories: linear and nonlinear. Many scholars applied spectral transformations, however, few of them discussed the effect of linearity in their studies. Linear transformation will maintain the linear relationship between variables while the nonlinear transformation will change the linearity relationship among variables. Some researchers state that nonlinear transformation may not be good for linear spectral mixture analysis, as it may decrease the accuracy of abundance estimation (Li, 2002). However, he did not imply that applying the nonlinear transformation in nonlinear spectral transformation guarantees improvement. The selection between using linear or nonlinear transformed schemes is still unclear.

Although many researchers applied spectral transformations in remote sensing applications, there is still not a study that examines all of them systematically. In particular, researchers employed different transformed schemes to their application based on their project requirement or their own knowledge. The advantages and limitations of all these transformed schemes are still not

clear. The necessity of applying a transformed scheme has not been discussed. Moreover, there is still not a standard of how to choose the transformed scheme. Therefore, the objectives of this study are: 1) to examine if there is a significant difference of SMA results after applying spectral transformation; 2) to find out which spectral transformation is better, and 3) to discuss how to select the transformed scheme in a specified landscape. The structure of this chapter is as follows. The next section talks about the background of spectral mixture analysis and spectral transformed techniques. Section 3 presents the experiments as well as results in three locations with Landsat data. Section 4 discusses the results and the strategy to select the transformed scheme. Finally, section 5 gives conclusions of this study.

3.2. Background

3.2.1 Spectral mixture analysis

Spectral mixture analysis (SMA) assumes that more than one land cover classes are combined in a mixed pixel. The objective of SMA is to estimate the fraction of each endmember within a mixed pixel. SMA can be expressed as equation (21). Generally, two constraints, the sum-to-one constraint ($\sum_{j}^{n} f_j = 1$) and nonnegative constraint ($0 \le f_j \le 1$), should be met in the fully constrained SMA.

$$R_k = \sum_{j}^{n} f_j R_{k,j} + \varepsilon_k \tag{21}$$

where R_k is the spectral reflectance of mixed pixel on band *k*; f_j is the fraction of endmember *j* within the pixel; $R_{k,j}$ is the spectral reflectance of endmember *j* on band *k*; ε_k is the error of band *k*; *n* is the number of endmembers.

Mean absolute error (MAE) is employed to evaluate the performance of SMA. It calculates the absolute difference between the estimated fraction and the reference fraction of corresponding land cover class. MAE can be expressed as equation (22).

$$MAE = \sum_{i=1}^{m} ABS(f_{e,i} - f_{r,i}) / m \quad (22)$$

where $f_{e,i}$ and $f_{r,i}$ are the estimated and reference fraction of sample i respectively; m is the number of samples.

3.2.2 Spectral transformations

Thirteen linear and thirteen nonlinear transformed schemes as well as an untransformed scheme were examined in this study. The major reason to select these schemes was that they are the most common schemes in the literature. Many commercial software packages, such as ERDAS and ENVI, have been embedded with these models. Researchers can easily implement these transformed schemes in their many applications.

3.2.2.1 Linear spectral transformation

Seven categories of linear spectral transformation were examined, namely derivative analysis [DA, (Tsai and Philpot, 1998)], principal component analysis [PCA, (Richards and Richards, 1999)], independent components analysis [ICA, (Hyvarinen, 1999; Hyvärinen and Oja, 2000)], Minimum Noise Fraction [MNF, (Boardman and Kruse, 1994; Green et al., 1988)], Tasseled Cap [TC, (Kauth and Thomas, 1976)], Band normalization (BN), and Discrete wavelet transformation [DWT, (Li, 2002; Strang and Nguyen, 1996; Vetterli and Herley, 1992), see Table 8]. Detailed descriptions of these methods are as follows.

Derivative analysis (DA) is sensitive to curve shape instead of the scale of reflectance. With this advantage, DA, especially higher order DA, is good for eliminating background signals and illumination effects caused by cloud coverage, sun angle, and topography (Tsai and Philpot, 1998). The first derivative analysis can be expressed as equation (23).

$$\left.\frac{dR}{d\lambda}\right|_i \approx \frac{R_{\lambda_i} - R_{\lambda_j}}{\Delta\lambda} \tag{23}$$

where $dR/d\lambda|_i$ represents the first derivative at wavelength λ_i. $\Delta\lambda = \lambda_i - \lambda_j$ is the difference between two consecutive wavebands and $\lambda_i > \lambda_j$. R_{λ_i} and R_{λ_j} are spectral reflectance of wavelength λ_i and λ_j. Similarity, second and third derivative can be expressed as equations (24-25).

$$\left.\frac{d^2R}{d\lambda^2}\right|_j \approx \frac{R_{\lambda_i} - 2R_{\lambda_j} + R_{\lambda_k}}{(\Delta\lambda)^2} \tag{24}$$

$$\left.\frac{d^3R}{d\lambda^3}\right|_k \approx \frac{R_{\lambda_i} - 3R_{\lambda_j} + 3R_{\lambda_k} - R_{\lambda_l}}{(\Delta\lambda)^3} \tag{25}$$

where $\lambda_i > \lambda_j > \lambda_k > \lambda_l$.

Independent components analysis (ICA) serves as a blind source separation tool for electronic signal analysis. Unlike PCA, ICA is based on a non-Gaussian assumption of the independent sources with higher-order statistics to extract focused characteristics in non-Gaussian datasets (Hyvarinen, 1999; Hyvärinen and Oja, 2000). A common ICA contains three steps: 1) the sample data are centered and whitened with the mean, eigenvectors, and eigenvalues. PCA is applied for data whitening; 2) negentropy maximization is employed as the whitened sample to estimate the ICA transform matrix; and 3) the original data is transformed using the ICA transform matrix (Hyvarinen, 1999; Hyvärinen and Oja, 2000).

Minimum noise fraction (MNF) transform, like PCA, is the method of separating noise and reducing data dimension (Boardman and Kruse, 1994; Green et al., 1988). MNF is modified from PCA. It includes two steps. The first step is called noise whitening. It employs the noise covariance matrix of PCA to decorrelate and rescale the noise in the data. The second step is to conduct the rotation again based on the first step's outcome. Specific channel information can be maintained in MNF since each component's weighting is contributed by all original bands. Most of the variance can be explained in the first three components, while the remaining components are contributed mainly by noise (Boardman, 1993).

Principal components analysis (PCA) is commonly used in remote sensing image analysis to produce uncorrelated output bands. It can be employed to reduce the dimension of a data set and to separate the noise from major components (Richards and Richards, 1999). The purpose of PCA is to create a new set of orthogonal axes which can maximize the data variance. Original dataset bands are correlated in multispectral and hyperspectral images. PCA compresses the original intercorrelated data into serval uncorrelated variables, named as principal components. The amount of variance decreases with the increase of the component's number. Generally, the first three components of PCA contribute more than 90% of the variance in the original dataset.

Tasseled Cap (TC) transformation orthogonally transforms the original data into a three-dimensional space (Kauth and Thomas, 1976), including brightness, greenness, and wetness (Jensen and Lulla, 1987). If the dataset is Landsat 7 enhanced thematic plus (ETM+), the results will contain three more outputs, e.g., fourth, fifth, and sixth. The first TC band relates to the overall brightness of the image while the second output band corresponds to the degree of greenness. The third band indicates the wetness of the land surface. TC transformation was originally designed to maximize separation of the different growth status of vegetation.

Band normalization (BN) reassigns the range of the pixel value in each band linearly. Contrasting information will be well presented in the stretched output. BN includes two steps: 1) finding out the maximum and minimum values in a band, and 2) calculating equation (26) in each pixel. With BN, light materials will display as lighter while dark regions appear darker, improving the efficacy of visual interpretation.

$$BN_k = (R_k - R_{k,\min}) / (R_{k,\max} - R_{k,\min}) \quad (26)$$

where BN_k is the band normalization value in band *k*. R_k is original spectral reflectance in band *k*. $R_{k,\max}$ and $R_{k,\min}$ are the maximum and minimum values of band *k* respectively.

Discrete wavelet transformation (DWT) can be implemented through fast wavelet transform [FWT, (Li, 2002; Strang and Nguyen, 1996; Vetterli and Herley, 1992)]. Mother wavelet is represented by a set of high-pass and low-pass filters in the filter bank. At the beginning, the original image signal goes through the filter bank. Then the result of the high-pass filter is named detail coefficients while the consequence of low-pass filter is called approximation coefficients. In the single-step discrete wavelet transformation, the original signal goes through the filter once. The image can be well reconstructed by using the approximation coefficients and setting other coefficients to zeros (Li, 2002). In this study, only single-level decomposition was performed with different wavelets (e.g., bior1.1 (DWT1), coif1 (DWT2), db1 (DWT3), rbio1.1 (DWT4), and sym2 (DWT5)).

3.2.2.2 Nonlinear spectral transformation

In addition to linear spectral transformation methods, we also examined four major non-linear transformation techniques, including continuum removal [CR, (Kruse, 1988)], spatial filtering transformation [e.g. Low pass (LP) filter, high pass (HP) filter, Gaussian low pass (GLP) filter,

and Gaussian high pass (GHP) filter], normalized spectral mixture analysis [NSMA, (Wu, 2004)], and Tie spectral (Tie) transformation (Asner and Lobell (2000). These transformation methods are summarized in Table 8, and described as follows.

Continuum removal (CR) is a method of spectral reflectance normalization. During the CR, straight-line segments connect every peak of local spectra to construct a convex hull (Kruse, 1988). The first and last peak in the local spectra are set to 1 in the continuum removal data while other data points in the original spectral curve are assigned as less than 1. It can enhance the absorption features from a spectral curve, eliminating the slope effects, topography, illumination, and grain-size effect. CR can be expressed as equation (27).

$$CR_k = R_k / C_k \tag{27}$$

where CR_k is Continuum removed spectrum in band *k*, R_k is original spectral reflectance in band *k*, and C_k is the corresponding continuum curve value in band *k*.

Spatial filtering is another type of spectral transformation. Generally, it involves a 3×3 or 5×5 moving window to construct a filter. The center value of the original pixel is replaced by a mathematical computation with the pixel value and their corresponding filter value (moving window value). Filters can be defined as high pass or low pass which highlights the corresponding frequency and suppresses the other frequency. If a filter is defined as high pass, rough areas where the spectral reflectance changes dramatically will be enhanced while smooth areas will be compressed. The low pass filter emphasizes the smooth areas instead of rough regions. Low pass (LP) filter, high pass (HP) filter, Gaussian low pass (GLP) filter, and Gaussian high pass (GHP) filter are commonly employed in remote sensing to enhance the corresponding land surface characteristics.

Normalized spectral mixture analysis (NSMA) was proposed by Wu (2004). Reflectance is divided by the mean value of the corresponding pixel in all band. Brightness can be eliminated or reduced through the NSMA, improving the separability of urban land cover classes. It can be calculated through equation (28).

$$NSMA_k = R_k / u \times 100 \tag{28}$$

where $u = (1/b) \times \sum_{k=1}^{b} R_k$, $NSMA_k$ is normalized value of band *k*, R_k is the original reflectance of band *k*. *u* is the mean reflectance of the corresponding pixel. *b* is the number of band.

Tie spectral (Tie) transformation was introduced by Asner and Lobell (2000). They employed the waveband of 2080nm as the tie point, then all other bands minus the tie point to get the tie transformation. Consequences indicated that tie spectra could reduce the variation caused by soil moisture, leaf and litter area index, tissue optics, and canopy architecture. However, only shortwave infrared bands were examined in their study. It is still meaningful to explore the potential tie points in visible and near infrared wavebands in urban and suburban areas. Thus, all bands were viewed as potential tie points and each tie transformation was calculated respectively.

Table 8 Spectral transformation

Transformation	Linearity	Reference
DA(1-3)	Linear	Tsai and Philpot (1998)
ICA	Linear	Hyvarinen (1999)
MNF	Linear	Green et al. (1988)
PCA	Linear	Richards and Richards (1999)
TC	Linear	Kauth and Thomas (1976)
BN	Linear	
DWT(1-5)	Linear	Vetterli and Herley (1992), Strang and Nguyen (1996)
CR	Nonlinear	Kruse (1988)
GHP, GLP, HP, LP	Nonlinear	
NSMA	Nonlinear	Wu (2004)
Tie (1-7)	Nonlinear	Asner and Lobell (2000)

3.3 Experiments

3.3.1 Study areas and data sources

Three cities were examined in this study, including Janesville, WI, Asheville, NC, and Columbus, OH (Figure 5). Janesville is on the western shore of Lake Michigan, within the humid continental climate. It has long nights in the winter and cool temperatures in summer. Flat plain is the major landscape in Janesville. Asheville is the largest city in western North Carolina. It is in the Blue Ridge Mountains where two rivers, the Swannanoa and French Broad, merge together. The climate in Asheville is humid subtropical, which is cool in winter and not as hot as other eastern cities in summer. Mountainous characteristics are significant in the Asheville area. Residential buildings are constructed based on its local terrain. Columbus, the largest city in Ohio, has relatively flat topography. Like Janesville, its climate is humid continental. Winter is cold and dry while summer is hot and muggy. The landscapes of the three study areas are similar. They are mainly occupied by commercial buildings, freeways, parking lots, residential houses, soil, and vegetation (trees and grass).

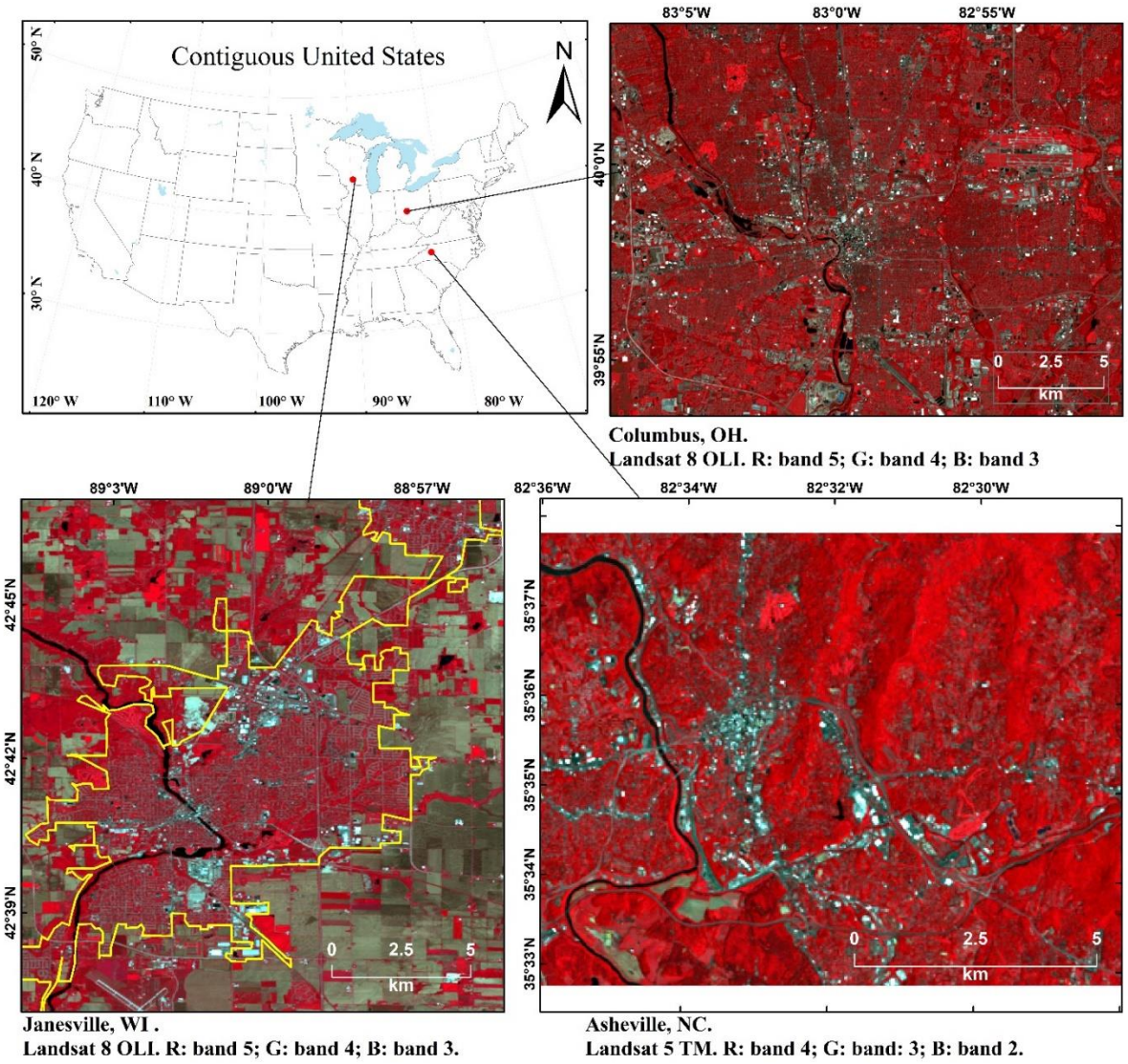

Figure 5 Study areas of Columbus OH, Janesville WI, and Asheville NC.

A scene of Landsat 8 Operational Land Imager (OLI) imagery acquired on September 14th, 2015 for Columbus, Ohio, a scene of Landsat 8 OLI imagery acquired on June 3rd, 2014 for Janesville, Wisconsin, and a scene of Landsat 5 Thematic Mapper (TM) imagery acquired on June 2nd, 2009 for Asheville, North Carolina were employed in this study. Image preprocessing, such as radiometric calibration, atmospheric correction using Fast Line-of-sight Atmospheric Analysis of Hypercube (FLAASH) with corresponding parameters, and reprojection to Universal Transverse

Mercator (UTM) (Janesville: Zone 16; Asheville and Columbus: Zone 17), were applied. Historical high spatial resolution images (Columbus: August 22nd, 2015; Janesville: June 12th, 2014; Asheville: May 30th, 2009) acquired on Google Earth were employed for accuracy assessment.

3.3.2 Method

3.3.2.1 Sample selection

Four land cover classes were selected in corresponding Landsat images, including vegetation (V), high albedo impervious surface area (ISAh), low albedo impervious surface area (ISAl), and soil (S). They were collected with the assistance of high spatial resolution images to avoid incorrect pixels. The number of training samples of V, ISAh, ISAl, and S are the same in each study area. They are 50, 50, and 50 in study areas of Janesville, Asheville, and Columbus respectively. Each training sample set was used for corresponding spectral library construction.

Testing samples were collected to access each scheme's performance. We selected 44, 60, and 50 testing samples in the Janesville, Asheville, and Columbus regions. Each testing sample is 3pixels×3 pixels (90m ×90m) to avoid the geometric error impact acquired from reprojection and data acquisition. Fractions of impervious surface area within the testing samples were calculated through digitizing the corresponding area in high spatial resolution images.

3.3.2.2 SMA and repeat test

Twenty-six transformed schemes (e.g., DA1-3, ICA, MNF, PCA, TC, BN, CR, GHP, GLP, HP, LP, NSMA, Tie1-7, and DWT1-5) were applied on the original data to get the transformed results in three different study areas (Janesville, Asheville, and Columbus). Fully constrained linear spectral mixture analysis was applied to transformed and untransformed data using the V-ISAh-

ISAl-S model. Each scheme was tested 100 times using randomly selected spectra in the corresponding spectral library.

3.3.2.3 MAE comparison

The performance of each transformed scheme was evaluated with mean absolute error (MAE). MAE was calculated based on comparison between estimated and referenced ISA fractions. Estimated fractions of ISA were calculated by the sum of ISAh's and ISAl's fractions in the same pixel. Boxplot and description of MAE were applied to detail the MAE distribution in each scheme. Statistical description, such as range, maximum value, minimum value, mean, and standard deviation, were employed to describe the MAE distribution. Boxplots can reveal the distribution of MAE using quantiles. The 25%, 50%, and 75% of the MAE can be mapped in the boxplot.

Since Boxplots only depicts the distribution of each scheme, the difference between transformed and untransformed schemes are still unclear, as they do not compare each test's performance. Therefore, paired-samples T tests were employed to test if there were significant differences of SMA mean between transformed and untransformed schemes. Unlike the analysis of variance (ANOVA), paired-samples T test compares the differences test by test. It can reveal the difference of each test. Mean difference is calculated by using the MAE of untransformed subtracting the transformed scheme. Positive values mean the MAE of untransformed schemes is larger than transformed schemes while negative values represent the opposite consequence. In addition the number of improved tests as well as their improved percentages were also counted to demonstrate their performance.

3.3.3 Results

The Landsat 8 OLI has one more band than Landsat 5 TM imagery. The second band of OLI matches the first band of TM. Thus, tie spectral transformation in Asheville (Landsat 5 TM) started naming from Tie2 to match the same Tie2 of Janesville and Columbus (Landsat 8 OLI).

The range and the standard deviation of the MAE in each transformed scheme can indicate the stability (Table 9). Large ranges imply relatively unstable performance. Many schemes' ranges varied dramatically across the three study areas. Some schemes show small ranges in one study area but display large ranges in other study areas (range differences between study areas are larger than 0.1), such as CR, GHP, LP, Tie1, Tie5, and DWT2. Other schemes, such as the untransformed scheme, DA2, DA3, ICA, PCA, GLP, Tie3, Tie4, Tie6, and Tie 7, showed a stable performance as their range differences among the three study areas are less than 0.05.

Table 9 Description of MAE in three study areas

Schemes	Janesville					Asheville					Columbus				
	Range	Min.	Max	Mean	SD	Range	Min.	Max	Mean	SD	Range	Min.	Max.	Mean	SD
Original	0.15	0.07	0.22	0.11	0.03	0.18	0.05	0.23	0.11	0.04	0.17	0.10	0.26	0.14	0.03
DA1	0.19	0.07	0.26	0.12	0.03	0.15	0.04	0.20	0.09	0.04	0.12	0.09	0.21	0.12	0.03
DA2	0.16	0.08	0.24	0.12	0.03	0.19	0.04	0.23	0.09	0.03	0.15	0.08	0.23	0.13	0.03
DA3	0.14	0.08	0.22	0.12	0.03	0.17	0.04	0.21	0.10	0.04	0.16	0.08	0.24	0.14	0.03
ICA	0.16	0.07	0.23	0.12	0.03	0.19	0.05	0.24	0.12	0.05	0.16	0.07	0.23	0.12	0.03
MNF	0.18	0.07	0.25	0.12	0.03	0.15	0.05	0.20	0.10	0.04	0.10	0.07	0.17	0.11	0.02
PCA	0.16	0.07	0.24	0.11	0.03	0.18	0.05	0.22	0.11	0.04	0.17	0.09	0.26	0.14	0.03
TC	0.16	0.07	0.23	0.11	0.03	0.20	0.05	0.25	0.11	0.05	0.13	0.09	0.22	0.14	0.03
BN	0.17	0.08	0.25	0.14	0.04	0.25	0.05	0.30	0.12	0.06	0.19	0.10	0.29	0.15	0.04
CR	0.22	0.08	0.30	0.20	0.06	0.28	0.06	0.34	0.14	0.06	0.10	0.08	0.18	0.11	0.02
GHP	0.22	0.10	0.33	0.18	0.05	0.33	0.13	0.47	0.21	0.06	0.23	0.17	0.40	0.25	0.05
GLP	0.16	0.08	0.23	0.11	0.04	0.16	0.05	0.21	0.11	0.04	0.20	0.09	0.28	0.13	0.04
HP	0.25	0.11	0.36	0.18	0.05	0.30	0.14	0.43	0.21	0.05	0.23	0.15	0.39	0.25	0.05
LP	0.33	0.08	0.41	0.12	0.06	0.23	0.05	0.28	0.12	0.05	0.17	0.09	0.25	0.13	0.04
NSMA	0.12	0.06	0.18	0.10	0.03	0.18	0.05	0.23	0.09	0.04	0.13	0.08	0.21	0.12	0.02
Tie1	0.18	0.08	0.26	0.13	0.04						0.29	0.09	0.38	0.14	0.04
Tie2	0.17	0.08	0.25	0.12	0.04	0.20	0.05	0.25	0.11	0.05	0.23	0.09	0.32	0.15	0.04
Tie3	0.15	0.08	0.23	0.12	0.03	0.19	0.05	0.24	0.10	0.04	0.16	0.07	0.23	0.13	0.03

Tie4	0.15	0.08	0.23	0.11	0.03	0.14	0.05	0.18	0.09	0.03	0.17	0.08	0.25	0.14	0.03
Tie5	0.17	0.08	0.24	0.11	0.03	0.28	0.05	0.33	0.10	0.04	0.19	0.07	0.26	0.13	0.03
Tie6	0.18	0.08	0.26	0.12	0.04	0.15	0.05	0.20	0.10	0.04	0.15	0.09	0.24	0.14	0.03
Tie7	0.15	0.09	0.24	0.12	0.03	0.19	0.05	0.24	0.10	0.04	0.15	0.08	0.23	0.15	0.03
DWT1	0.29	0.08	0.38	0.13	0.05	0.20	0.05	0.24	0.11	0.04	0.20	0.08	0.29	0.13	0.04
DWT2	0.27	0.08	0.35	0.13	0.05	0.16	0.05	0.21	0.12	0.04	0.21	0.09	0.30	0.15	0.04
DWT3	0.27	0.08	0.35	0.13	0.05	0.17	0.05	0.22	0.11	0.04	0.18	0.10	0.28	0.14	0.04
DWT4	0.17	0.08	0.25	0.12	0.03	0.26	0.05	0.31	0.12	0.05	0.18	0.09	0.27	0.14	0.04
DWT5	0.25	0.08	0.32	0.12	0.05	0.28	0.06	0.33	0.12	0.05	0.18	0.09	0.26	0.13	0.04

However, range as well as standard deviation of MAE only illustrate stability. They do not indicate how good the performance is. Mean, to a certain degree, implies the average performance of a scheme. Most of the transformed schemes' mean MAE are like the untransformed scheme except the schemes of CR, GHP, HP, and Tie1 (MAE difference is larger than 0.05). Unfortunately, the mean MAEs of CR, GHP, HP, and Tie1 are 0.05 larger than the untransformed scheme. In particular, the mean MAE of GHP and HP are larger than the untransformed scheme in all study areas, implying their poor performance.

As described in Figure 6, about 50 percentage of the untransformed scheme's (Original) MAE are less than 0.11 in Janesville area. Other schemes, like the PCA, TC, GLP, LP, and Tie4, Tie5, Tie7, DWT1-5, have similar number of tests which their MAEs are less than 0.11. NSMA has a significantly higher percentage (more than 60%) and the MAE is less than 0.11. Transformed schemes of DA1-3, ICA, BN, Tie1-3, and Tie have slightly less tests that their MAEs are less than 0.11. The remaining transformed schemes, such as BN, CR, GHP, and HP, almost all tests' MAE are larger than 0.11, indicating that they would weaken SMA results.

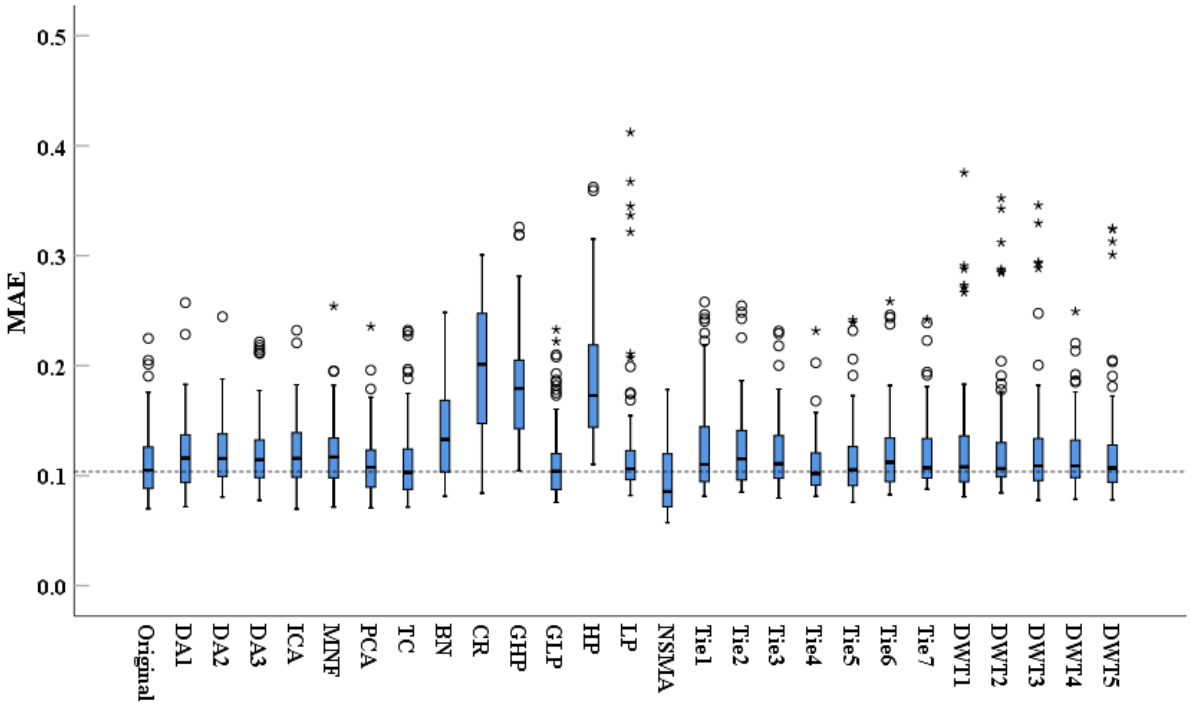

Figure 6 Boxplot of MAE of Janesville

MAE distributions in Asheville are generally different from Janesville (Figure 7). There are higher percentages of MAE less than 0.1 in Asheville. However, the range of the schemes looks larger than Janesville as well. The mean MAE of untransformed scheme is about 0.1, which is close to the mean MAE of the Janesville study area. Schemes of DA1-3, GLP, and Tie1-6 have slightly better performances than the untransformed scheme, as their medians are lower than 0.1. NSMA performance is the best among the other schemes. More than 75% of the MAEs are less than 0.10. However, schemes of ICA, CR, GHP, HP, and DWT2-3 weaken SMA performance, resulting in larger percentage of high MAE values.

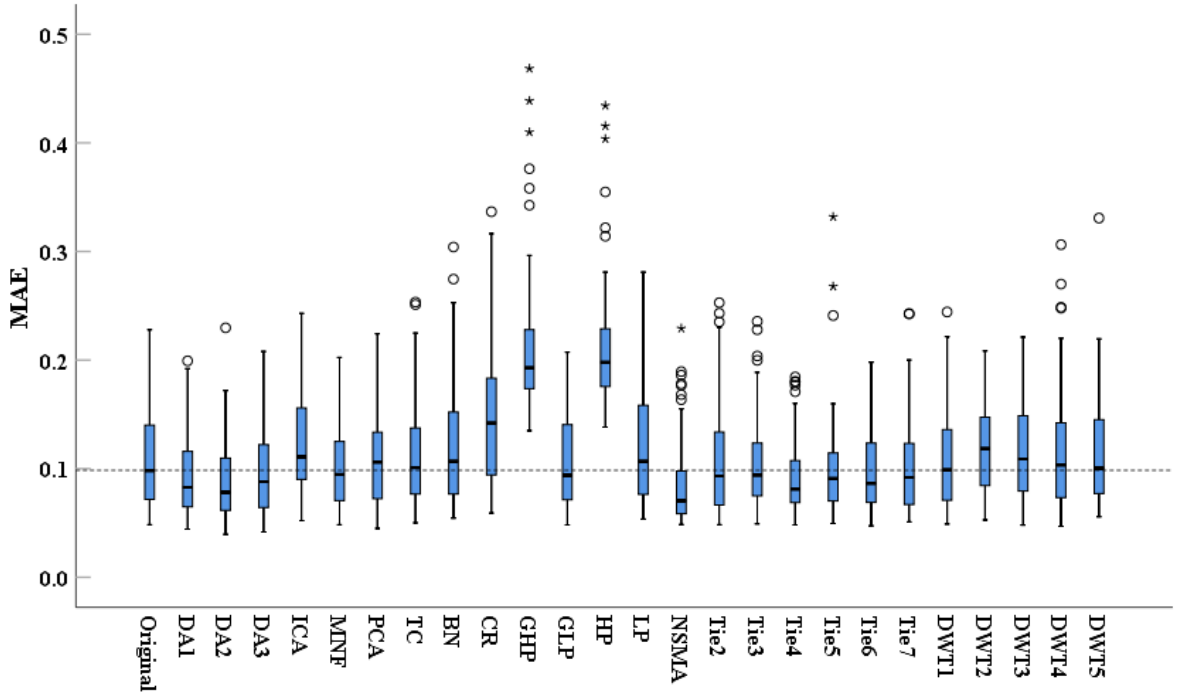

Figure 7 Boxplot of MAE of Asheville

The median MAE of the untransformed scheme in Columbus (Figure 8) is about 0.13, which is worse than the performances in the Janesville and Asheville study areas. Schemes of GHP and HP illustrate extreme high MAEs in all study areas. Other schemes, such as DA1-2, ICA, CR, GLP, LP, NSMA, Tie3, Tie5, DWT1, DWT4 and DWT5, have higher percentage of MAEs that are less than 0.13. In particular, the performance of MNF and CR are much better than the untransformed scheme, as most of their MAEs are less than 0.13. DA3, PCA, TC, Tie1-2, Tie6-7, and DWT2-3 have similar MAE distributions with the untransformed scheme.

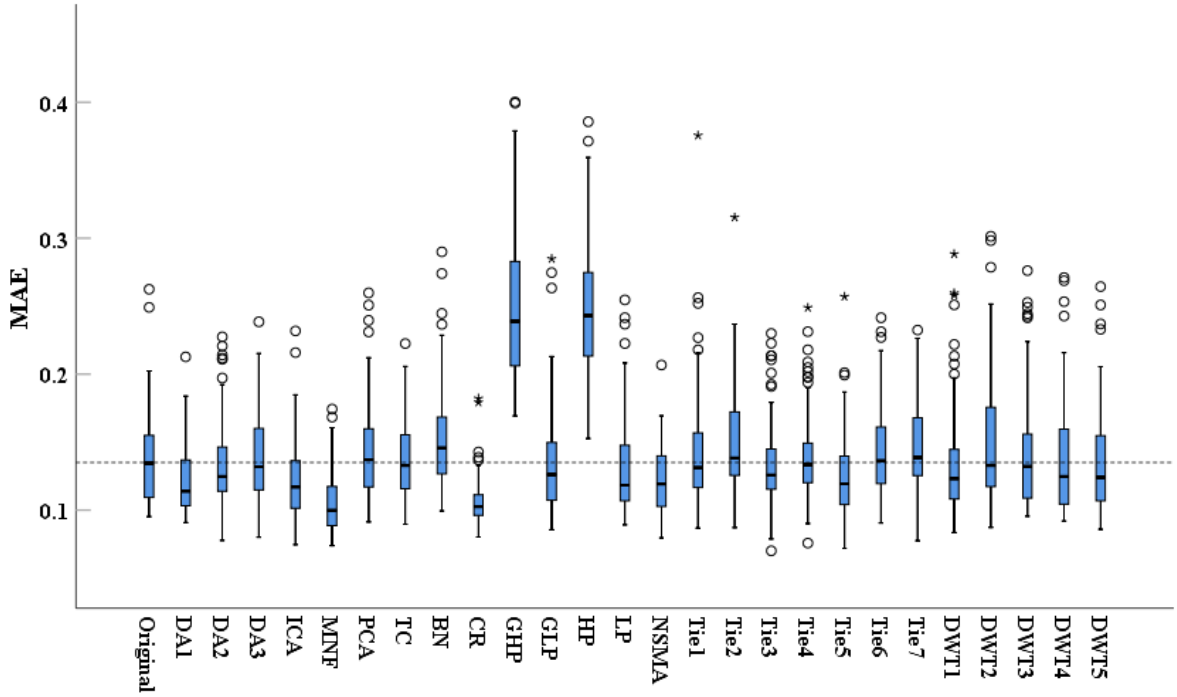

Figure 8 Boxplot of MAE of Columbus

Table 10 reveals that only NSMA shows improvement. Its mean MAE is lower than the untransformed scheme in all study areas. Paired-samples T test results illustrate that differences between NSMA and untransformed scheme are significant, as their p values are less than 0.05. Some schemes, such as DA1-2, MNF, GLP, and Tie3-5, have slightly lower mean MAEs in two study areas but have larger mean MAEs in another study area compared to the untransformed scheme. However, paired-samples T tests cannot indicate the significant difference since many of these transformed schemes' p values are larger than 0.05. DA1-3, CR, NB, Tie4, and Tie 6-7 perform better only in one study area and the other two areas weaken SMA results. Other transformed schemes, such as TC, BN, GHP, HP, Tie1, and DWT2-4 all decrease the accuracy as the mean differences are negative in all three study areas. However, significant differences between the untransformed scheme and transformed schemes except BN, GHP, and HP cannot be determined as their p values are larger than 0.05.

In addition, we counted the number of improved tests as well as the mean improved percentage for each scheme. Generally, transformed schemes in Asheville perform better than the other two study areas as the number of improved tests is generally larger than the other two areas, such as the schemes of DA2-3, NSMA, Tie2, Tie4, Tie 6-7. The NSMA performs better than the untransformed scheme in Janesville, Asheville, and Columbus as 67%, 69%, and 62% of the tests have lower MAEs. The performance of CR is very unstable. The number of improved tests varies greatly with number of 11, 32, and 87 in Janesville, Asheville, and Columbus respectively. Only a few numbers of tests of GHP and HP perform better than the untransformed scheme. The improved percentages in each scheme are relative high. Many of the transformed schemes can have more than 30% mean improvement in the improved test.

Table 10 Results of Paired-Samples T test and comparison

Schemes	Paired-Samples T Test						Numbers of improved test			Improved percentage (%)		
	Mean difference			Sig. (2 tailed)								
	Jane.	Ash.	Col.	Jane.	Ash.	Col.	Jane.	Ash.	Col.	Jane.	Ash.	Col.
DA1	-0.008	**0.015**	**0.012**	0.054	0.011	0.003	38	58	66	28.0%	47.3%	23.8%
DA2	-0.008	**0.020**	**0.002**	0.043	0.001	0.618	36	67	53	29.3%	54.9%	27.2%
DA3	-0.009	**0.012**	-0.003	0.059	0.058	0.429	40	59	46	31.0%	58.5%	23.1%
ICA	-0.009	-0.015	**0.014**	0.031	0.024	0.002	37	37	59	28.0%	55.0%	29.6%
MNF	-0.009	**0.007**	**0.030**	0.069	0.219	0.000	45	52	79	28.4%	43.2%	35.3%
PCA	**0.001**	-0.001	-0.006	0.894	0.864	0.208	49	47	41	29.2%	53.0%	32.2%
TC	-0.001	-0.002	-0.001	0.908	0.763	0.890	52	49	49	28.6%	46.5%	21.5%
BN	-0.028	-0.014	-0.016	0.000	0.050	0.002	25	44	40	26.0%	44.6%	22.8%
CR	-0.087	-0.036	**0.030**	0.000	0.000	0.000	11	32	87	26.5%	43.6%	24.1%
GHP	-0.069	-0.102	-0.113	0.000	0.000	0.000	11	6	2	21.7%	15.6%	48.6%
GLP	-0.001	**0.001**	**0.002**	0.848	0.912	0.753	55	52	55	26.0%	21.2%	14.5%
HP	-0.073	-0.103	-0.112	0.000	0.000	0.000	10	5	1	19.8%	11.1%	11.7%
LP	-0.013	-0.013	**0.005**	0.061	0.100	0.318	46	46	59	25.6%	24.8%	13.5%
NSMA	**0.015**	**0.022**	**0.014**	0.001	0.000	0.001	**67**	69	**62**	32.8%	38.9%	29.2%

Tie1	-0.014		-0.009	0.003		0.081	37		47	23.6%		21.6%
Tie2	-0.012	**0.002**	-0.016	0.009	0.774	0.003	35	54	41	27.3%	59.3%	6.2%
Tie3	-0.008	**0.005**	**0.001**	0.051	0.381	0.870	37	52	55	25.3%	18.5%	18.4%
Tie4	**0.003**	**0.016**	-0.005	0.544	0.002	0.281	49	58	45	30.4%	48.5%	22.7%
Tie5	-0.002	**0.011**	**0.010**	0.623	0.063	0.024	46	57	61	33.1%	51.8%	25.1%
Tie6	-0.009	**0.012**	-0.008	0.054	0.049	0.093	39	54	46	27.6%	57.5%	24.9%
Tie7	-0.009	**0.008**	-0.010	0.071	0.152	0.023	44	54	38	28.7%	51.1%	23.2%
DWT1	-0.013	0.000	**0.002**	0.030	0.977	0.682	43	55	56	27.8%	46.4%	25.2%
DWT2	-0.014	-0.010	-0.013	0.024	0.073	0.018	45	43	35	25.9%	37.2%	30.7%
DWT3	-0.014	-0.007	-0.004	0.027	0.272	0.424	43	45	48	29.0%	38.5%	25.1%
DWT4	-0.007	-0.007	-0.004	0.094	0.294	0.527	40	52	50	25.6%	37.0%	29.1%
DWT5	-0.009	-0.008	**0.002**	0.133	0.232	0.711	43	44	57	30.3%	40.0%	23.2%

3.4 Discussion

Spectral variability, including between- and within-class variability, is widely present in remotely sensed imagery. Factors, such as materials' spectral characteristics, geometry, and other environmental elements, contribute to differences of spectral reflectance (Portigal et al., 1997; Zhang et al., 2006). These spectral variabilities cause significant confusion in image classification. Efforts (e.g., weighted spectral mixture analysis, spectral transformation) are made by researchers to minimize the within-class variability and to maximize the between-class variability.

Although many scholars have applied spectral transformation in their applications, there is still not a consensus about which transformed scheme should be used. This study compared most of the spectral transformations and applied them in three different study areas to test their performance. Moreover, 100 times repeated tests with different endmembers' spectra as well as tests in different regions could reveal the reliability of each scheme. Janesville, Asheville, and Columbus are far from each other. Residential areas, commercial areas, soil, tree, and grass are the major land feature types in each of these areas. These regions can be viewed as typical urban and

suburban environments in the U.S.A. Therefore, it is meaningful to compare these three locations with the same endmember model, to test the reliability of each transformed scheme.

3.4.1 Linear or nonlinear transformation?

Results in this study indicate that there is not a significant difference between linear and nonlinear spectral transformation. It cannot be concluded that linear (nonlinear) transformation is better than nonlinear (linear) in SMA. Theoretically, the linear transformation maintains the linear relationship while the nonlinear change the linearity. Li et al. (2002) stated that abundance estimation accuracy of the linear spectral mixture model (LSMM) decreased when the nonlinear wavelet transformation was applied. Nonlinear transformation might be good for the nonlinear spectral mixture model (NSMM) instead of LSMM. However, results in this study and the earlier results of Wu (2004) illustrate that this conclusion might not be true when the study area is located in an urban area, since NSMA in the three study areas as well as in the study of Wu (2004) performed better than the untransformed scheme. Further, statistical tests also implied their differences were significant.

3.4.1.1 Linear transformed schemes

Many linear spectral transformations have different performance in each study area. Results of DA1 and DA2 are slightly worse than the results in the study of Zhang et al. (2004). This can be attributed to the different data sources. Zhang et al. (2004) applied hyperspectral data while multispectral data were employed in this study. Hyperspectral data can provide more spectral information than multispectral imagery, which may be good for SMA unmixing. However, Zhang et al. (2004) did not provide a comparison with untransformed data, which make it difficult to evaluate the performance of the derivative spectral unmixing (DSU). DA can get rid of unnecessary signal components and highlight minor absorption features by using spectral

smoothing and the feature reduction method. However, it can also raise the possibility of ignoring essential spectral features (Youngentob et al., 2011). Different locations may have different essential spectral features. DA may miss different features in different study areas. Thus, the performance of DA varies from place to place. Results in this study also illustrate an unstable performance of DA, since DA only performed better in some regions while weakening the result in other areas.

ICA showed an opposite result compared to the study of Wang and Chang (2006). It did not perform better than the second-order statistics-based methods like PCA and MNF. That may be due to the theory of ICA--that it only conserves crucial and critical information such as anomalies, endmembers, and small targets instead of variance which preserved by PCA and MNF (Wang and Chang, 2006). However, there is not a clear pattern about the ICA, PCA, and MNF, as the results indicated that their performance varied from place to place.

The performance of PCA, MNF, TC, and BN are not satisfactory in this study. PCA evaluates the components based on eigenvalues while the MNF employs the signal-noise ratio (SNR) to rank the importance of each components. The limitation of PCA and MNF may be attributed many subtle material substances in Landsat imageries not being identified by second-order statistics (Wang and Chang, 2006), which may provide confusion between classes. The last three bands of PCA, TC and MNF contain little variance, so they may reduce the between-class variance and increase the within-class variance, adding more confusion during the classification. BN does not seem to be necessary in SMA since it weakened the results in all three study areas.

DWT's performance conflicted with the result of Li (2004). The differences between this study and Li (2004)'s study are due to the land cover types, data sources, wavelet types, and endmember

model. Li employed higher-level wavelet types (e.g., Db3, Sym3) while only lower-level wavelet transformation (e.g., db1, Sym2) is applied. Further, the land cover types in Li (2004)'s study are agriculture lands that contains soybean, large crabgrass, and soil. Only two and three endmember models in Li's study were tested while this study used an applied four-endmember model. Another major limitation about Li (2004)'s study is that he did not test the untransformed scheme, which limits knowledge of how DWT improved the SMA result. Paired-samples T tests in this study demonstrated that lower-level DWT might not be good for SMA as they could not improve the accuracy.

3.4.1.2 Nonlinear transformed schemes

CR's performance varies dramatically. Result in Columbus are similar to the result of Youngentob et al. (2011). However, the Janesville and Asheville results demonstrate the opposite. Though CR produced a promising result in chemical concentrations estimation in leaves by removing irrelevant background reflectance and emphasizing absorption features of interest, it did not show a stable performance in this study. This may be due to the difference of spectral characteristics between the leaves and impervious surface and the complexity of spectral reflectance in urban and residential areas. CR can enlarge the band depth differences, reducing the error in spectroscopic estimation of vegetation quality (Mutanga et al., 2005). However, the variability in impervious surface area, both of high albedo and low albedo, are larger than vegetation, implying CR may enlarge the within-class variance as well. Some scholars state that CR may introduce more signature to noise interference, increasing the within-class variability of the same class (Carvalho Junior and Guimaraes, 2001). That may explain why CR weakened the SMA results in Janesville and Ashville.

Spatial filters, especially HP and GHP, are not suitable for SMA as they all reduce the large scale accuracy in all three study areas. GLP and LP still provided limited improvement in some areas. However, statistically tests could not indicate the significance. Therefore, spatial filters may be good for the edge detection or image smoothing instead of SMA.

NSMA can address the confusion between impervious surface areas and soil effectively. Between-class variance between soil and impervious surface increased after NSMA. Moreover, the effect of shade can be removed by the brightness normalization. Both aspects can improve the accuracy of SMA. Janesville and Asheville's landscapes are like Columbus, and NSMA has similar performance in these three study areas, proving the stability of NSMA in urban and suburban environments.

3.4.2 Change after transformation

Linear and nonlinear transformations show both better performance and drawbacks in SMA. It is impossible to conclude which type of transformation, linear or nonlinear, should be used in SMA. Therefore, the change of each transformed scheme needs exploration. Many transformed schemes' objectives are to minimize the within-class variance and to enlarge the between-class variance. However, there is not an index to quantify the change of between- and within-class variance. Therefore, a between-class and within-class variance index (BWVI) was constructed to explore the change of within- and between-class variance. The BWVI is a ratio between the sum of differences of between- and within-class variance and sum of total variance. Theoretically, higher between-class variance and lower within-class variance will lead to a higher value of BWVI. BWVI can be expressed as equation (29).

$$BWVI = \sum_{k}^{b} \left(\frac{Bv_k - Wv_k}{Tv_k} \right) \tag{29}$$

where

$Bv_k = \sum_j^n m_j \times (\bar{R}_{k,j} - \bar{R}_k)^2$, $Wv_k = \sum_j^n \sum_i^{m_j} (R_{k,ij} - \bar{R}_{k,j})^2$, $Tv_k = Bv_k + Wv_k$, $\bar{R}_{k,j}$ is the mean reflectance of endmember j's sample in band k. $\bar{R}_k$ is the mean reflectance of all endmember's sample in band *k*. *b* is the number of band. Bv_k , Wv_k and Tv_k are the between-class variance, within-class variance, and total-class variance in band *k*. *m* is the number of sample.

3.4.3 Which transformation to choose?

The relationships between BWVI and mean MAE were explored in all three areas. Regressions indicate significant linear relationships between these two parameters with p values of 0.049, 0.043, and 0.000 in Janesville, Asheville, and Columbus, respectively (Table 11, *Figure 9, Figure 10,* and *Figure 11*). In addition, linear models in the three study areas had similar patterns. Constant values are positive and b1 values are negative in all study areas. Moreover, the scale of the corresponding parameters are close to each other, implying that the relationship between BWVI and MAE is reliable.

Table 11 Linear regression summary

Study areas	Model Summary					Parameter Estimates	
	R Square	F	df1	df2	Sig.	Constant	b1
Janesville	0.147	4.291	1	25	0.049	0.136	-0.004
Asheville	0.159	4.550	1	24	0.043	0.124	-0.006
Columbus	0.567	32.765	1	25	0.000	0.166	-0.008

The dependent Variable: MAE. The independent variable: BWVI.

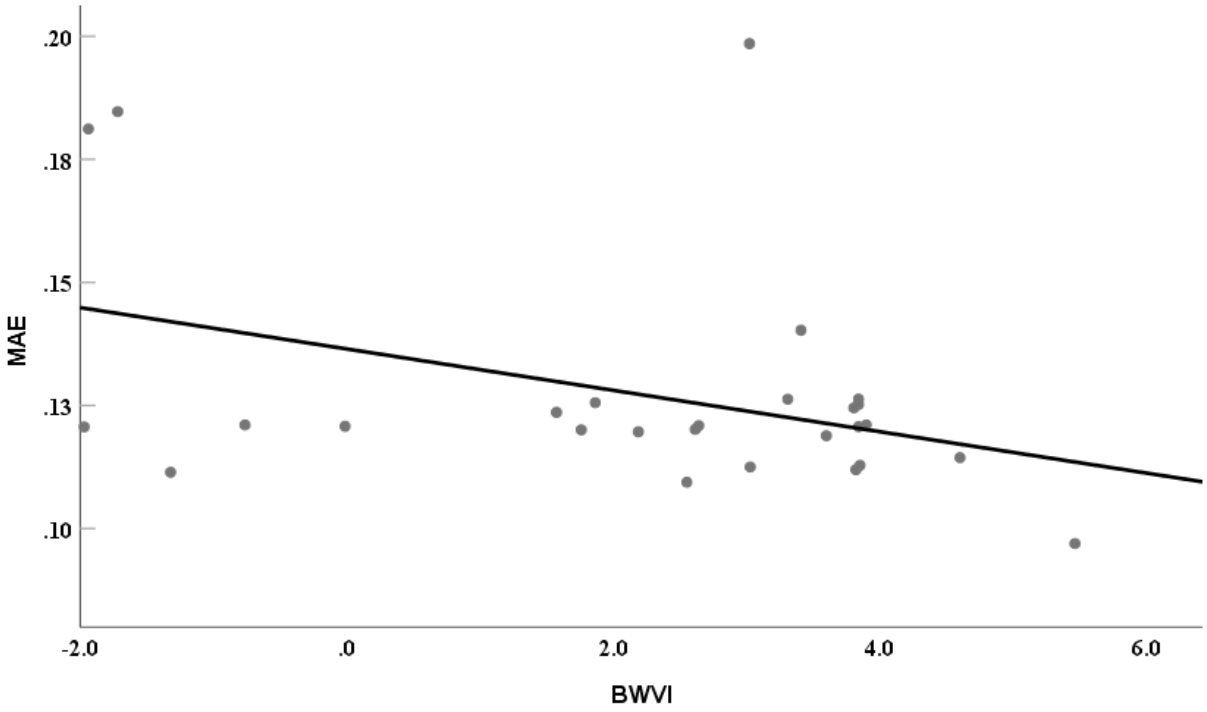

Figure 9 Scatterplot of MAE and BWVI of Janesville

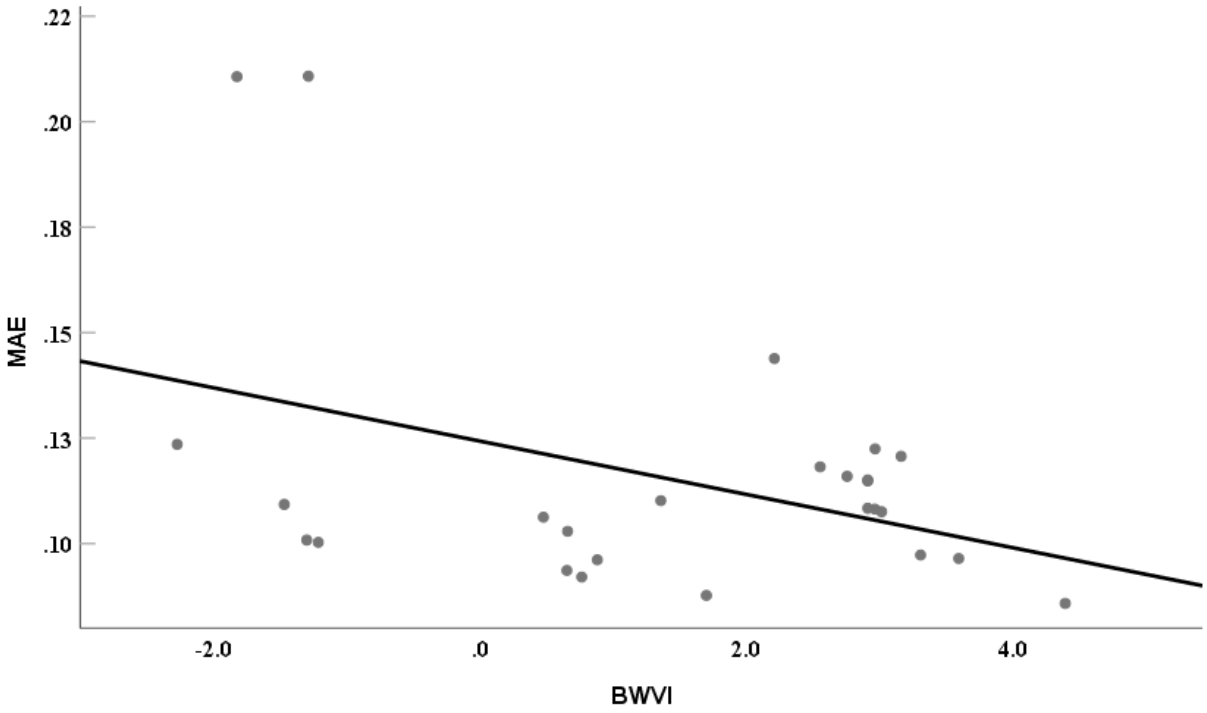

Figure 10 Scatterplot of MAE and BWVI of Asheville

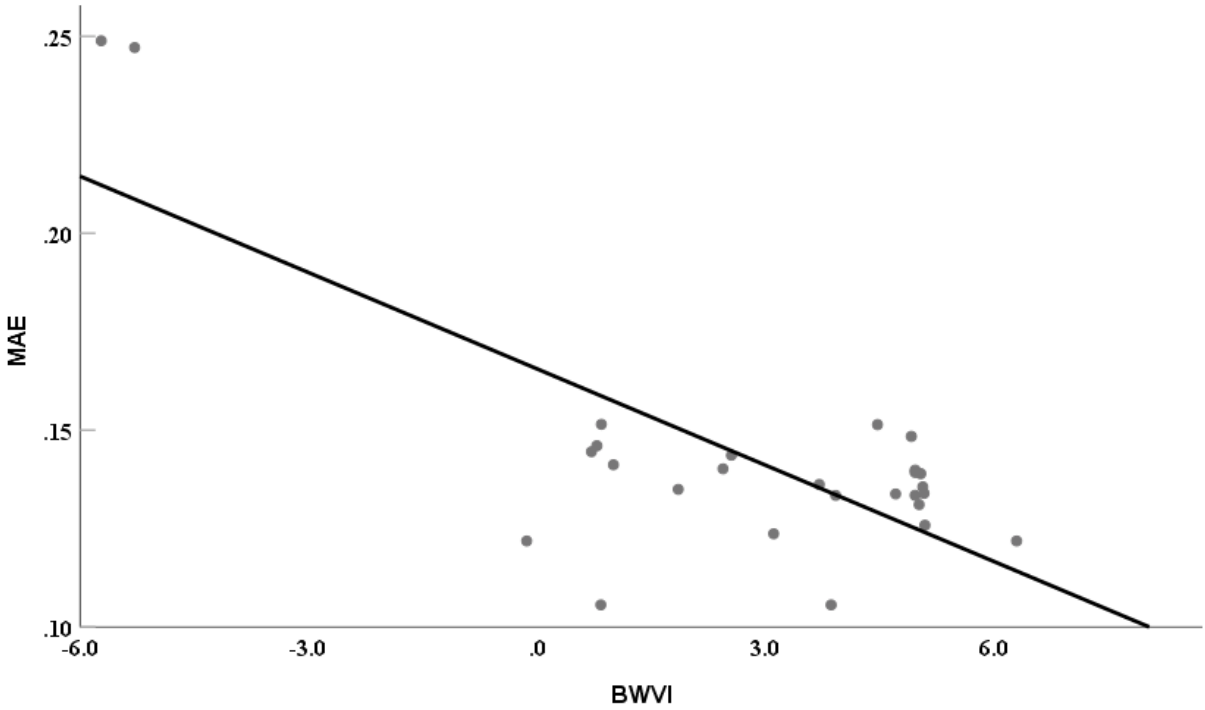

Figure 11 Scatterplot of MAE and BWVI of Columbus

With the relationship between BWVI and MAE, the decision of which transformation to choose in a specified area can be made. A transformed scheme with a higher BWVI value will have a higher possibility to acquire low MAE (*Figure 9*, *Figure 10*, and *Figure 11*). Thus, if a transformed scheme has a higher BWVI, it may perform better in the SMA. In this case, researchers only need to compare the BWVI values instead of calculating the MAEs to decide which scheme to use in their applications. This will save a lot of time by reducing the unmixing calculation and MAE calculations. Researchers can find out the most accurate scheme quickly with the BWVI.

3.4.4 Limitations and future work

This study only focused on multispectral images and humid urban regions. More data sources, such as hyperspectral images and coarse spatial resolution images, and more study areas, e.g., arid and semi-arid areas, should be tested in the future. Further, different endmember models, such as three endmember models, need to be examined in the future.

3.5 Conclusions

This study examined the performance of several linear and nonlinear transformations in Janesville, Asheville, and Columbus respectively. Many transformed schemes except NSMA could not illustrated a stable performance in all three study areas. Some transformed schemes only improved the SMA in one or two study area but weakened the results in other regions. Some transformed scheme weakened the performance in all three study areas. NSMA showed reliable improvement in all three areas. Paired-samples T tests also indicated NSMA's significance in reducing MAE. Although some transformed schemes' mean MAE was less than the untransformed scheme, statistically tests demonstrated that these improvements were not significant. Both linear and nonlinear transformed schemes have advantages and disadvantages in subpixel unmixing. It is not possible to select the spectral transformed scheme based on linearity. It is time consuming to evaluate the performance of a transformed scheme by calculating its MAE. Therefore, this study constructed an index to guide the selection of a transformed scheme. The BWVI was designed based on a ratio between the sum of differences of between- and within-class variance and sum of total variance. Results demonstrated that there was a negative linear relationship between BWVI and MAE. Larger BWVI has a higher possibility to acquire lower MAE. Researchers can calculate the BWVI instead of MAE to decide if it is necessary to apply spectral transformation in SMA, which will save a lot of time and work by reducing the number of unmixing calculations.

CHAPTER4 DEVELOPMENT OF A CLASS-BASED MULTIPLE ENDMEMBER SPECTRAL MIXTURE ANALYSIS (C-MESMA) APPROACH FOR ANALYZING URBAN ENVIRONMENTS[3]

4.1 Introduction

Spectral mixture analysis (SMA) has been widely applied to address the mixed pixel problem, a typical issue associated with medium- and coarse-resolution remote sensing imagery (Powell et al., 2007; Roberts et al., 1992; Sabol et al., 1992; Settle and Drake, 1993). SMA assumes that each image pixel is comprised of several land cover classes, each of which has distinctive spectral signatures (Settle and Drake, 1993; Tompkins et al., 1997). Traditional SMA approaches, with a fixed set of endmembers, perform reasonably well in areas with relatively homogenous land covers, mostly due to the ease of identifying representative endmembers. In urban and suburban environments, however, inter-class and intra-class spectral variability widely exist (Kumar et al., 2013; Roth et al., 2012; Settle, 2006; Thorp et al., 2013; Youngentob et al., 2011). Therefore, the capability of traditional SMA models to deal with complex urban and suburban landscapes has been questioned, as the few endmembers may not be able to represent their corresponding land cover classes (Radeloff et al., 1999; Song, 2005; Tang et al., 2007).

As an improved version of SMA, multiple endmember spectral mixture analysis (MESMA) developed by Roberts *et al.* (Roberts et al., 1998) has successfully addressed the issues of endmember variability, and been widely applied to numerous fields, including impervious surface area (ISA) extraction, vegetation detection, and water management, etc. With MESMA, modeling errors, such as root mean square of the residual error [(RMSRE, (Tan et al., 2014)], have been typically considered as important criteria for selecting the best-fit model (Roberts et al., 1998). Generally, with the same number of endmembers, a model with a smaller RMSRE is chosen due

[3]Portions of this chapter have been published to *Remote Sensing*, coauthored with Dr. Changshan Wu

to higher modeling accuracy. In the case of the availability of different endmembers' numbers, the model with the fewer number of endmembers is selected when their RMSRE ' difference is trivial (Song, 2005). For successful spectral unmixing, the selection of an appropriate endmember set is essential, and the selection may greatly impact the performances (Somers et al., 2011). In particular, if an endmember is mistakenly included in an SMA model, its abundance is likely to be over-estimated [e.g. greater than zero, (Jia et al., 2010)]. Moreover, with the minimization of RMSRE as the criterion, some erroneously selected endmembers may have a better fit due to the existence of within-class and between-class spectral variability. As an example, spectral signatures of ISAs are similar to those of dry soils (Deng and Wu, 2013b; Lu and Weng, 2009), and they are often mistakenly considered as endmembers in farmlands (Deng et al., 2012), where major land covers should only include vegetation and soil. This is primarily due to the selection of the ISA-vegetation model instead of the vegetation-soil model if only RMSRE are considered. As a result, the abundance of ISAs in farmlands is mistakenly over-estimated while that of soil is underestimated by MESMA.

Recently, several approaches have been proposed to address the abovementioned deficiency. Franke *et al.* (Franke et al., 2009) proposed a hierarchical multiple endmember spectral mixture analysis to divide an image into several land cover types (several levels) to limit the spatial distribution of endmembers. Sub-classes' fractions were extracted from the upper level classification results. They found that the distribution of endmembers could be well constrained from the results obtained from the upper level, thereby improving classification accuracy. Liu and Yang (2013) introduced a similar method which classified the study area into rural and urban subsets with the assistance of road network density. Then MESMA was carefully applied to urban subsets using three types of endmembers (vegetation, ISA, and soil), while a supervised

classification model was employed for the rural area. Results illustrated that this method could minimize the spectral confusion between some urban land cover classes and agricultural landscapes.

Although these two methods can spatially constrain the distribution of endmembers, they cannot fully address the mixed-pixel problem. A critical limitation of hierarchical MESMA (Franke et al., 2009) is that a pixel at level 1 is assigned to the ISA or the pervious surface class based on their corresponding fraction values resulted from a linear SMA. For instance, at level 1, a pixel is assigned to the impervious class with the ISA fraction higher than 50%, otherwise it is assigned to the pervious class. In other words, mixed pixels still exist in both pervious surface and ISA classes. Results from hierarchical MESMA is promising. However, these outcomes were only from high spatial resolution imagery (4 meters). This method still needs to be verified in the middle and coarse resolution images. In Liu and Yang's research (Liu and Yang, 2013), a vegetation cover threshold was utilized to separate vegetation and non-vegetation. This threshold, however, is pixel-based, which would also contain mixed pixels in both vegetation and non-vegetation classes.

To address these problems, this chapter proposes a land cover class-based MESMA (C-MESMA) to map the land cover fractions of urban/suburban environments using a Landsat image. This method was developed through combining supervised classification and MESMA techniques. At the first level, a support vector machine (SVM) was applied to classify the study area into six land cover classes, three pure land cover classes (e.g., ISA, vegetation, soil) and three mixed land cover classes (e.g., ISA-vegetation, vegetation-soil, and vegetation-ISA-soil). For pure land cover classes, a fraction value of one is assigned to the corresponding class. For mixed land cover classes, a MESMA was implemented with corresponding spectral libraries to extract each endmember's fractional coverage. Finally, fractions of ISA, vegetation, and soil of each land cover class were

merged together to produce final fractional maps of ISA, vegetation, and soil. Performance of the developed C-MESMA was tested through comparing to results of the standard MESMA.

The next section introduces the study area and data sources. Section 3 presents the method of C-MESMA, as well as comparative analyses with traditional MESMA. Results of C-MESMA and accuracy assessment are reported in Section 4. Finally, discussion and conclusions are provided in Sections 5 and 6.

4.2 Study area and data source

Two counties (Figure 12): Milwaukee and Waukesha in Wisconsin, United States were selected as the study area. Geographically, both counties are in the Great Lake Region with a humid continental climate. They cover about 2,665km^2 with a population of 1.3 million (DeNavas-Walt et al., 2009). Milwaukee is dominated by urban and suburban land uses (e.g., commercial, residential and industrial area etc.), while Waukesha is mostly covered by suburban and rural lands (e.g., farmland and forest). A large amount of ISA, bare soil, and vegetation exist in this study area, making it an ideal site for examining the effectiveness of the proposed C-MESMA model.

A Landsat 7 Enhanced Thematic Mapper plus (ETM+) image (path 23, row 30) acquired on September 11th, 2001 was used as the primary data. Six spectral bands (except the thermal band) with a spatial resolution of 30 m were utilized for C-MESMA. Digital numbers (DNs) of the image were converted into calibrated radiance image using the Landsat calibration model provided by ENVI, a commercial remote sensing image processing software package. An atmospheric correction model, Fast Line-of-sight Atmospheric Analysis of Spectral Hypercubes (FLAASH) (Atmospheric Model: Mid-Latitude Summer, Aerosol Model: Rural, Aerosol Retrieval: 2-Band (K-T), Output Reflectance Scale Factor: 1), was applied to accurately compensate for atmospheric

effects (FLAASH, 2009). A Digital Orthophoto Quarter Quadrangle (DOQQ, Scale: 1: 24,000) image of Milwaukee and Waukesha (April 13, 2000) was utilized as the reference data to evaluate the performance of supervised classification and the MESMA results. Water area was masked with a supervised classification method before applying C-MESMA. All the images were re-projected to the Universal Transverse Mercator (UTM) with zone 16 and datum WGS84.

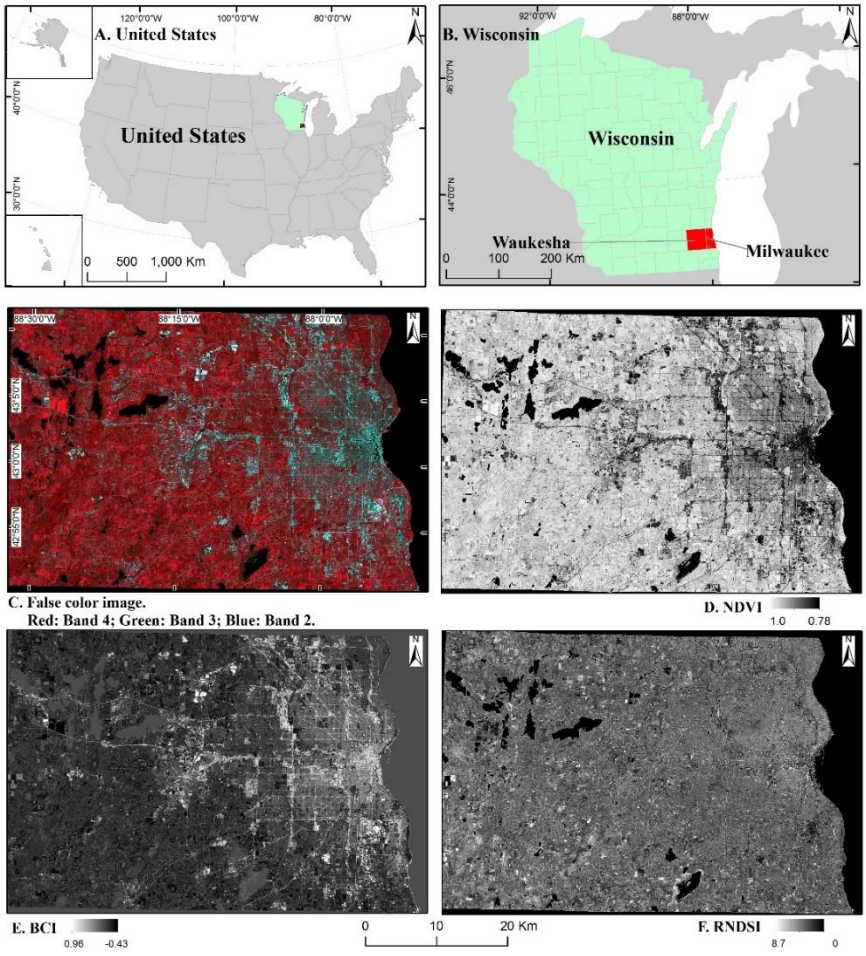

Figure 12 Study area. (A) United States. (B) Wisconsin. (C) False color of Landsat 7 ETM+. (D) NDVI. (E) BCI. (F) RNDSI.

4.3 Methods

C-MESMA includes two processes: supervised classification and MESMA (see Figure 13). Specially, supervised classification comprises the spectral indices generation and layer stacking

while the MESMA contains subpixel unmixing (MESMA) and fraction image merging. Three spectral indices: normalized difference vegetation index (NDVI) (Rouse et al., 1973), biophysical composition index (BCI) (Deng and Wu, 2012), and ratio normalized difference soil index (RNDSI) (Deng et al., 2015) were calculated and stacked with the Landsat reflectance image. Spectral characteristics of all land cover classes were expected to be enhanced by adding these three spectral indices (Shao and Liu, 2014). Then, a support vector machine (SVM) was applied to the stacked image with six classes of elaborately selected training samples. They were selected with the reference of DOQQ image to avoid the potential mixed pixel and to validate the correctness of the sample. These training samples contain three pure land cover classes: ISA (60 samples), soil (37 samples), and vegetation (60 samples), and three mixed land cover classes: vegetation-ISA (60 samples), vegetation-soil (60 samples), and vegetation-ISA-soil (26 samples). The ISA-soil land cover type was merged into the class of vegetation-ISA-soil as very few pixels belong to the ISA-soil land cover type. The whole study area was partitioned into six layers based on the SVM results. Since the land cover classes of ISA, vegetation, and soil were considered as pure pixels, they were not involved in the unmixing process. Instead, fraction value of one was assigned to the corresponding class directly. MESMAs were applied to the three mixed land cover classes with corresponding spectral libraries. Three fractional maps of ISA, vegetation, and soil were finally produced through merging the pure land cover classes resulted from SVM and the fraction images acquired from MESMA. Figure 13 shows the flowchart of the C-MESMA.

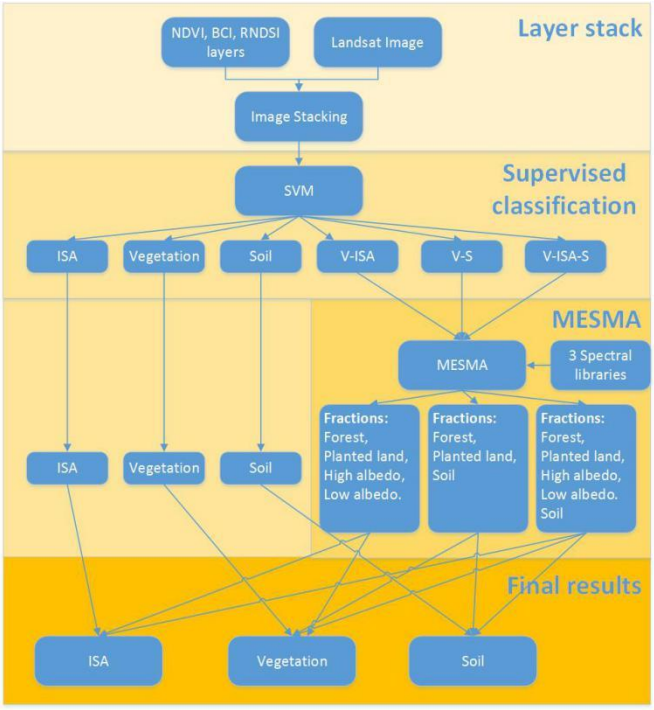

Figure 13 Flowchart of class-based MESMA. High albedo, low albedo, and ISA were combined as ISA. Forest, planted land, and vegetation were combined as vegetation. Soil in soil pure land cover class and soil in fraction images were combined as soil.

4.3.1 Supervised classification

Spectral indices have been widely applied to remote sensing imagery to achieve better performances for image classification and visual interpretation (Zhang, 2010). In this study, this strategy was applied to emphasize the spectral signatures of different land cover classes, aiming to mitigate spectral confusion between high albedo ISA and dry soil, low albedo ISA and water, as well as shadow and water covers.

Three spectral indices, including biophysical composition index (BCI), normalized difference vegetation index (NDVI), and ratio normalized difference soil index (RNDSI), were stacked into the original reflectance bands of Landsat image. BCI, which is calculated by a reexamination of Tasseled Cap Transformation, can enhance the ISA information in the urban/suburban area. It shows a better performance to reduce soil effect when compared to the normalized difference ISA

index (NDISI) and normalized built-up index (NDBI) (Deng and Wu, 2012). Normalized difference vegetation index (NDVI) is a spectral indicator that represents vegetation cover and condition. It is the most successful attempts to quickly identify vegetation area and their "condition" from remotely sensed imagery (Rouse et al., 1973). Further, RNDSI can suppress ISA and vegetation values, as well as highlight soil information (Deng et al., 2015). With each of these indices, only one land cover can be emphasized while others are suppressed, leading to enhanced differences between land cover types. These three indices can be calculated from Equations (30-32).

$$BCI = \frac{(H+L)/2 - V}{(H+L)/2 + V} \tag{30}$$

Where $H = \frac{TC1 - TC1_{\min}}{TC1_{\max} - TC1_{\min}}$, $V = \frac{TC2 - TC2_{\min}}{TC2_{\max} - TC2_{\min}}$, and $L = \frac{TC3 - TC3_{\min}}{TC3_{\max} - TC3_{\min}}$.

TC1, TC2, and TC3 represent the first, second, and third component in the tasseled cap transformation.

$$NDVI = \frac{B_{NIR} - B_{RED}}{B_{NIR} + B_{RED}} \tag{31}$$

BNIR and BRED refer to the reflectance in near-infrared and red bands respectively.

$$RNDSI = \frac{NNDSI}{NTC1} \tag{32}$$

where $NNDSI = \frac{NDSI - NDSI_{min}}{NDSI_{max} - NDSI_{min}}$, and $NTC1 = H$. H has the same values in equation (26) and the NDSI can be written as equation (33):

$$NDSI = \frac{(band7 - band2)}{(band7 + band2)} \quad (33)$$

where band7 and band2 are the seventh and second band of Landsat TM/ETM+ image. X_{max} and X_{min} are the maximum and minimum values of corresponding bands respectively.

SVM is a widely used approach for the classification of remotely sensed imagery (Melgani and Bruzzone, 2004). Its objective is to find the hyperplane that separates the dataset into a discrete predefined number of classes in a fashion consistent with the training samples (Mountrakis et al., 2011). A large number of applications have shown that SVM can produce a better performance than other pattern recognition techniques, like maximum likelihood and neural network classifiers (Melgani and Bruzzone, 2004). Therefore, a SVM classification method was adopted in this research. With these three spectral indices (see Figure 12), as well as six Landsat spectral bands, an SVM classification was performed to classify the image into six land cover classes, namely ISA, vegetation, soil, ISA-vegetation, vegetation-soil, and vegetation-soil-ISA. Training samples were acquired from the Landsat image with a careful check from DOQQ image. In a total of 330 reference samples (55 samples for each class) were employed to calculate the confusion matrix and to evaluate the performance SVM classification.

4.3.2 MESMA

4.3.2.1 Endmember selection and spectral library construction

Endmember selection is a critical step for successfully implementing SMA (Elmore et al., 2000). Deciding the number of endmembers and their corresponding spectral signature is the first step to select proper endmembers. In this study, endmembers were extracted through choosing "pure" pixels in the Landsat image. The endmembers were selected with the following steps, including: 1) examining the entire study area carefully through visualizing the DOQQ image, 2)

figuring out the number of endmembers in this study area, 3) overlapping the Landsat ETM+ image with the DOQQ image, 4) identifying regions containing corresponding endmembers, 5) extracting ETM+ pixels that locate in the center of each individual region, 6) comparing these selected pixels to the pixels of same location in the SVM image and removing erroneously labeled pixels, 7) averaging the spectra of selected pixels of each endmember and employing the mean spectrum as endmember. Finally, five endmembers: forest, planted lands, high albedo features, low albedo features, and soil, were selected to build the spectral library. As it is unnecessary to perform an MESMA for pure land cover types, three spectral libraries were constructed, each of which is corresponding to each mixed land cover class (e.g. ISA-vegetation, vegetation-soil, and vegetation-soil-ISA) (see Table 12). Spectral reflectance values and spectral indices of each endmember are shown in Figure 14.

Table 12 Spectral libraries and endmembers

Libraries (Number of endmember)	**Endmembers**
ISA-Vegetation (4)	High albedo, Low albedo, Forest, Planted land
Vegetation-Soil (3)	Forest, Planted land, Soil
Vegetation-Soil-ISA (5)	High albedo, Low albedo, Forest, Planted land, Soil

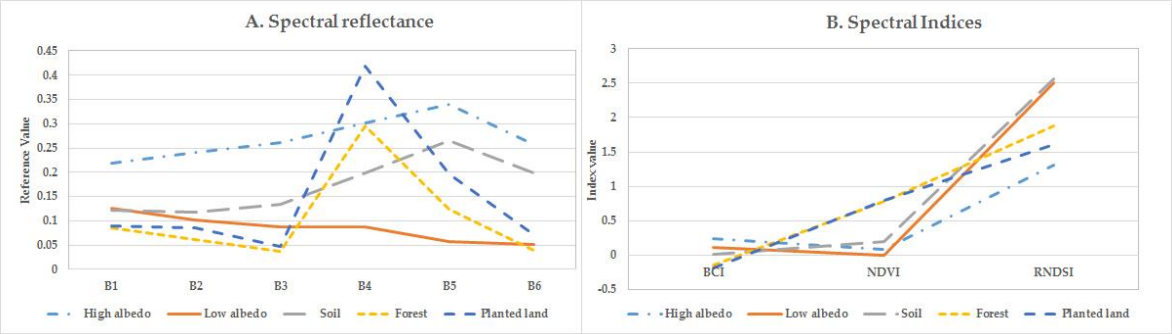

Figure 14 Spectral reflectance(A) and Spectral indices (B) of each endmember.

4.3.2.2 Model Construction

SMA assumed that a spectrum of a mixed pixel is combined by several endmembers' spectra. It centers on applying a mathematical method to derive the fraction of each endmember. Linear SMA is one of the most commonly used SMA with the assumption that each land cover was combined linearly to form a pixel's spectrum. LSMA can be expressed as equation (34).

$$R_i = \sum_{k=1}^{n} f_k R_{ik} + ER_i \tag{34}$$

Where $i = 1,\ldots, m$ (m: number of bands); $k = 1,\ldots, n$ (n: number of endmembers); R_i is the spectral reflectance of band i; f_k is the proportion of endmember k within the pixel; R_{ik} is the known spectral reflectance of endmember k within the pixel on band i; and ER_i is the estimation error for band i. A fully constrained least squares solution [24] was applied which assuming that the following two conditions are satisfied simultaneously: $\sum_{k=1}^{n} f_k = 1$, and $0 \le f_k \le 1$.

Although simple, LSMA is not suitable for complex urban environments with many manmade materials. As only one endmember is allowed for each cover type, LSMA cannot adequately address spectral variability in complex urban areas (Okujeni et al., 2013; Quintano et al., 2013;

Roberts et al., 2012; Song, 2005). Multiple Endmember Spectral Mixture Analysis (MESMA), which was proposed by Roberts (Roberts et al., 1998), is an improved method accounting for within-class and between-class spectral variability. The number of spectra is not limited in the spectral library and the endmember combination can vary from pixel to pixel, which effectively solves the spectral variability issue in LSMA. In this study, MESMA was applied to three mixed land cover types with their corresponding spectral libraries. RMSRE (equation 35) was utilized as the parameter to select the best-fit endmember model. In other world, it is used to evaluate the performance of the endmember combination. Here the abbreviation of RMSRE is used in order to differentiate the root mean square error (RMSE) which was utilized for assessing the accuracy between estimated and reference fractions in MESMA results.

$$RMSRE = \sqrt{\sum_{i=1}^{N} \frac{ER_i^2}{N}} \tag{35}$$

where ER_i is estimation error of band i, which was calculated using equation (5), and N is the total number of band.

Generally, a model with more endmembers may lead to a lower RMSRE when compared to that with fewer endmembers. However, inappropriate endmembers may be included, and therefore lead to erroneous estimation of fractional land covers. To address this problem, a model with fewer endmembers may be selected as the best-fit model if, when compared to the model with a larger number of endmembers, the RMSRE difference is small (e.g. less than 0.1) (Franke et al., 2009). With land cover fractions derived from MESMA, vegetation fractions were derived as the summation of those of forest and planted lands, and ISA fractions were calculated through adding the fractions of low-albedo and high-albedo materials. Finally, the fractional land cover maps were generated through combining the fraction images resulted from SVM and MESMA.

4.3.3 Accuracy assessment

Accuracy assessment is a required procedure for evaluating the model performance. Traditional accuracy assessment methods, such as confusion matrix, Kappa coefficient, and overall accuracy, however, are not applicable for subpixel-based mixture analysis (Finn, 1993; Foody, 1996, 2002). The most commonly used approach is root mean square error (RMSE) which compares the fraction values between reference and modeled results. Reference fraction values were measured from the DOQQ imagery in the same sample sites as samples in MESMA result. In this study, only the fraction of ISA is chosen to be analyzed, owning to the facts that 1) soil and vegetation change extremely between seasons and 2) the acquisition date of DOQQ image was not perfectly matched to the date of the Landsat image. Therefore, accuracy analysis of vegetation and soil was ignored. RMSE can be written as equation (36).

$$RMSE = \sqrt{\frac{\sum_{i=1}^{N} (\hat{X}_i - X_i)^2}{N}} \tag{36}$$

Where $\hat{X}_i$ is the modeled ISA fraction value of sample *i*, and X_i is the reference ISA fraction value of sample *i*, and *N* is the number of samples.

In total, 351 samples were selected (vegetation: 62, soil: 20, ISA: 32, vegetation-soil: 37, vegetation-ISA: 128, and vegetation-ISA-soil: 72) using a stratified random strategy. Each sample was designed as 90m×90m (3 pixels × 3 pixels in Landsat image) to mitigate the impact of geometric errors introduced in data acquisition and projection transformation. Fractions of ISA in the DOQQ image were extracted by digitalizing ISAs within the sample (See Figure 15). For examining the performance of C-MESMA, we identified eleven categories, including all samples, ISA samples, vegetation samples, soil samples, vegetation-soil samples, vegetation-ISA samples,

vegetation-ISA-soil samples, ISA-excluded samples, ISA-included samples, all pure land cover type samples, and all mixed land cover types samples. The accuracy of each category was also compared to the corresponding results of the traditional MESMA.

Figure 15 Illustration of reference land cover fraction calculation. Background is a portion of a DOQQ image; red rectangle represents the 90m×90m (3×3 pixel in Landsat image) sample; green region is the area with impervious surfaces. The reference fraction was calculated through dividing the area of impervious surfaces by the area of the sample (8100 m2).

4.4 Results

4.4.1 SVM Classification

With SVM, the whole study area was classified into six land cover classes. Classification results (see Figure 16) indicate that ISA areas were mainly located in the Milwaukee County, especially in the downtown area and large shopping malls. Vegetation was primarily distributed in the southern region. Soil, which was much more dispersed than vegetation and ISA, was majorly distributed in the rural area. Vegetation-ISA was the major land cover type in the residential area, which was located outside the central business district (CBD) region. Vegetation-soil areas mainly occupied the farmland area. Vegetation-ISA-soil areas were mainly close to roads and residential lands.

Confusion matrix and Kappa statistics were calculated to illustrate the accuracy of SVM classification. With the overall accuracy of 87.58% and Kappa coefficient of 0.85, SVM result is acceptable for further analysis. Details of classification accuracy are shown in Table 13.

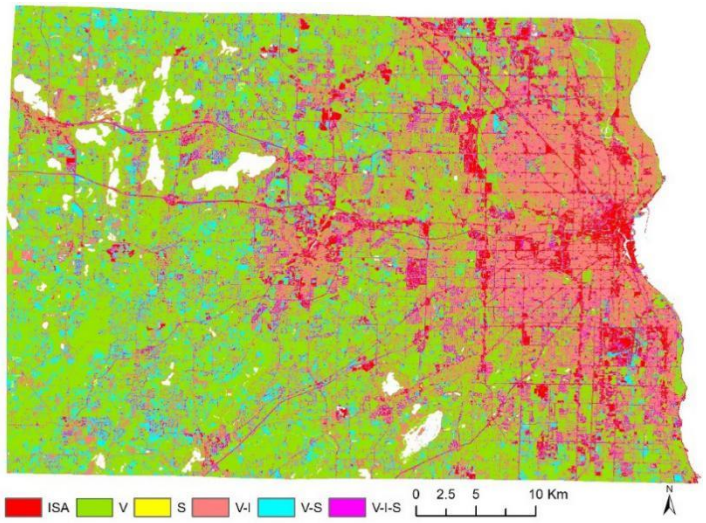

Figure 16 Result of SVM. ISA: impervious surface area, V: vegetation, S: soil, V-I: vegetation-ISA, V-S: vegetation-soil, V-I-S: vegetation-ISA-soil. Water was marked before applying the SVM.

Table 13 Confusion matrix of SVM classification

	Reference Data							
Classified	IS	V	S	I-V	V-S	V-I-	Tota	User Acc.
ISA	54	0	6	2	1	1	64	84.38
V	0	55	0	2	12	0	69	79.71
S	0	0	43	0	1	0	44	97.73
I-V	0	0	3	50	7	1	61	81.97
V-S	0	0	3	1	34	0	38	89.47
V-I-S	1	0	0	0	0	53	54	98.15
Total	55	55	55	55	55	55	330	
Prod. Acc.	98.	10	78.1	90.9	61.8	96.3		
Overall Accuracy=87.58%			Kappa Coefficient=0.85					

Note: ISA, V, S, I-V, V-S, and V-I-S mean classes of impervious surface area, vegetation, soil, impervious surface-vegetation, vegetation-soil, and vegetation-impervious surface-soil respectively.

4.4.2 MESMA

Five endmembers, including planted land, forest, high albedo, low albedo features, and soil, were selected to build the spectral libraries of corresponding land cover types. For each mixed land cover type (i.e. ISA-vegetation, vegetation-soil, and vegetation-soil-ISA), an individual MESMA was applied to estimate the fraction of these endmembers. Subsequently, the ISA fractional map was generated through adding the fractions of low and high albedo features for these mixed land cover types, and merging the fractional maps for the pure land cover classes (see Figure 17A). Similarly, the vegetation fractional map was derived through adding the fractions of forest and planted lands for the mixed land cover types, as well as merging those for the pure classes (see Figure 18A). Finally, the soil fractional map was created through merging the fractional soil maps for the mixed and pure soil fractional maps (see Figure 19A). For a better comparative analysis, the resultant fractions of ISA, vegetation, and soil generated from the traditional MESMA with the same endmembers, data source, and unmixing algorithm were also shown in Figure 17B, Figure 18B, and Figure 19B.

Visualization of the ISA fractional map (Figure 17A) suggests that high percentage of ISAs (%ISA) is concentrated in the CBD of Milwaukee City and large shopping malls. Besides, major roads and highways also contribute to high values of %ISA as well. Medium %ISA mainly dominated residential areas surrounding the CBD of Milwaukee. Comparatively, a consistent spatial pattern of ISA distribution was found with C-MESMA and MESMA. Major differences, though, lie in the ranges of the estimated %ISA values in urban and rural areas. With C-MESMA, higher %ISA values were obtained in urban areas, while lower %ISA values were derived in rural areas (see Figure 17A and B). Taking rural areas as an example, the %ISA of planted lands and forest areas is near zero with C-MESMA, while the values are approximately 20% with MESMA.

This overestimation is primarily due to the mistakenly inclusion of ISA endmembers in MESMA. Conversely, for urban areas, %ISA values are higher with C-MESMA, mostly due to the exclusions of soil members.

In addition to %ISA, there are also differences in terms of the estimation of vegetation and soil fractions (see Figure 18 and Figure 19). It appears that, with C-MESMA, the fractions of vegetation are relatively higher when compared to those derived from MESMA (see Figure 18). For soil fractions, it appears that less soil was estimated in urban Milwaukee, and a higher amount of soil was derived in rural areas with C-MESMA (see Figure 19).

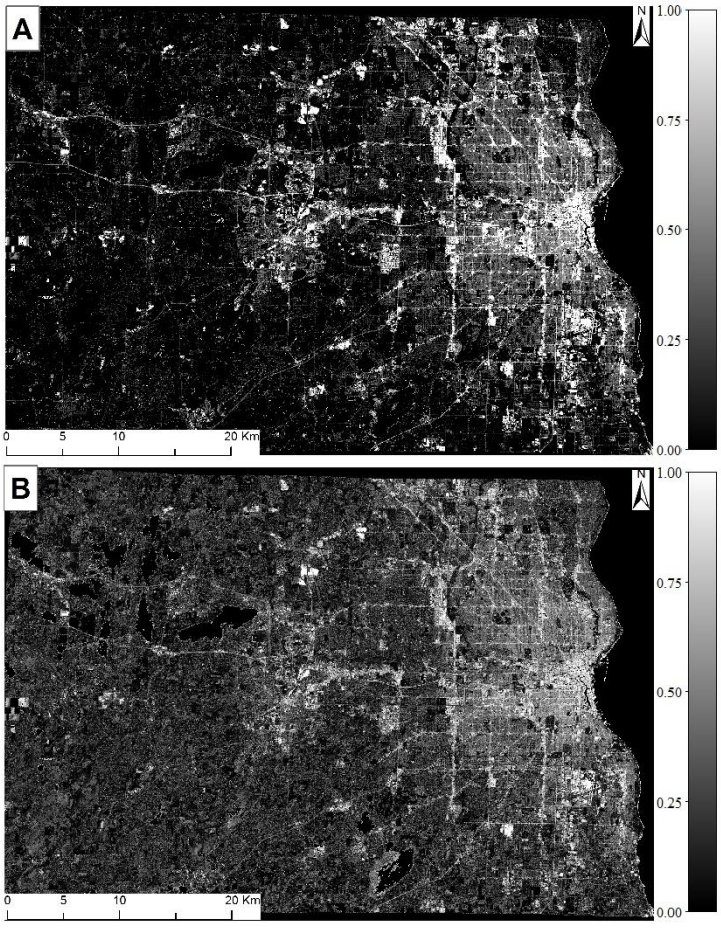

Figure 17 ISA fraction. (A) ISA fraction of C-MESMA. (B) ISA fraction of MESMA.

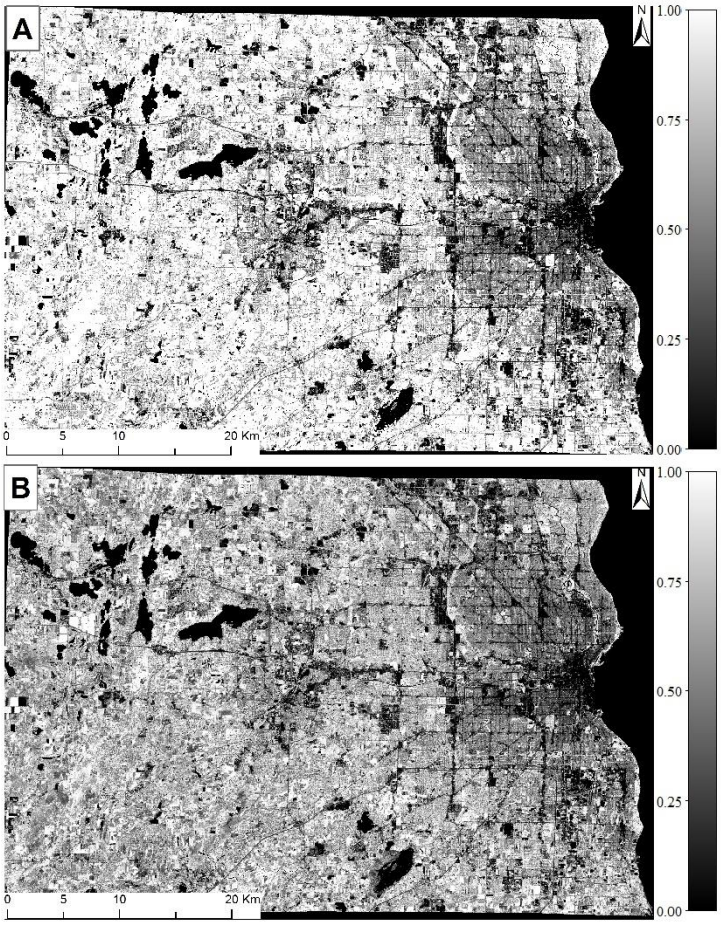

Figure 18 Vegetation fraction. (A) Vegetation fraction of C-MESMA. (B) Vegetation fraction of MESMA.

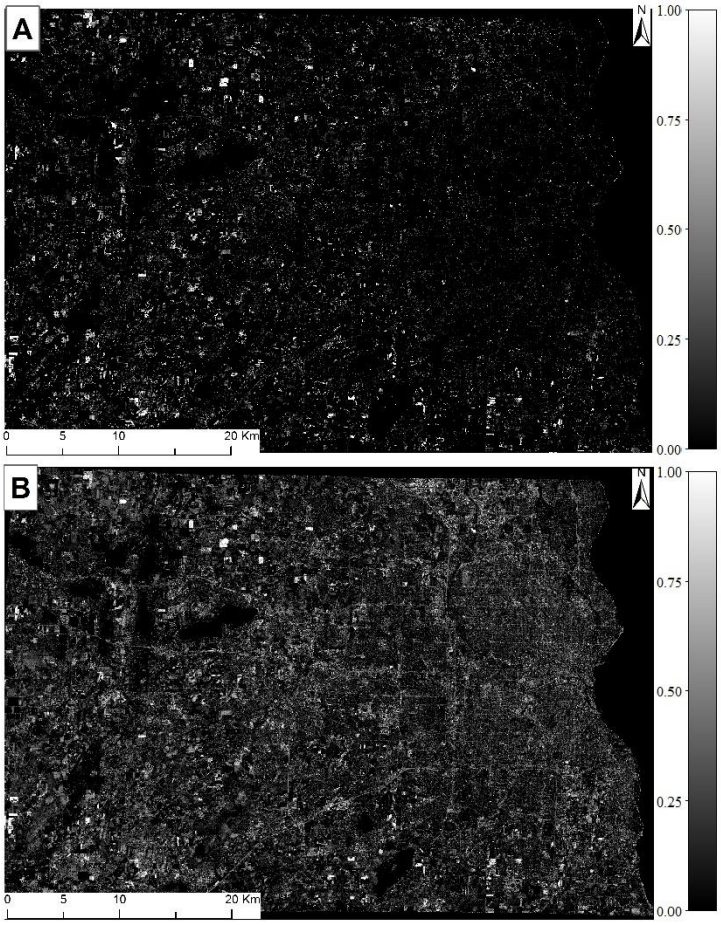

Figure 19 Soil fraction. (A) Soil fraction of C-MESMA. (B) Soil fraction of MESMA.

4.4.3 Accuracy assessment and comparative analysis

In addition to the visual examinations of the fractional maps of ISA, vegetation, and soil, quantitative accuracy assessment was also applied. As discussed in Section 4.3, the accuracy of %ISA estimation for eleven groups of samples was examined, namely ISA, vegetation, soil, vegetation-soil, vegetation-ISA, vegetation-ISA-soil, ISA-excluded, ISA-included, all pure land cover types, and all mixed land cover types. RMSE of each group of samples was calculated for both C-MESMA and MESMA (see Figure 20). Results revealed that, for almost all categories except soil, RMSE values of C-MESMA were significantly lower than those of MESMA. With C-MESMA, the overall RMSE was 0.12, which is significantly lower than that (0.18) with MESMA.

RMSE of soil with C-MESMA (0.35) was slightly higher than that in MESMA (0.34). Of course, both were relative high compared to those of the other land cover types, indicating the difficulty of separating ISA and bare soil. In addition to accuracy assessment for all samples, with C-MESMA, RMSEs of vegetation, vegetation-soil, vegetation-ISA-soil, ISA-included, and mixed land cover samples were less than 0.1. Especially, the RMSE of vegetation land cover type was 0.01, meaning that almost all fractions in the C-MESMA matched perfectly with the reference data. RMSEs in the corresponding land cover types of MESMA were at least 0.05 higher than those with C-MESMA. The RMSEs of ISA, vegetation-soil, ISA-excluded, and pure pixel with C-MESMA were a little bit high, but their values were much lower than those with MESMA. In summary, these comparative analyses show that the performance of C-MESMA is better than MESMA for almost all land cover types in this research.

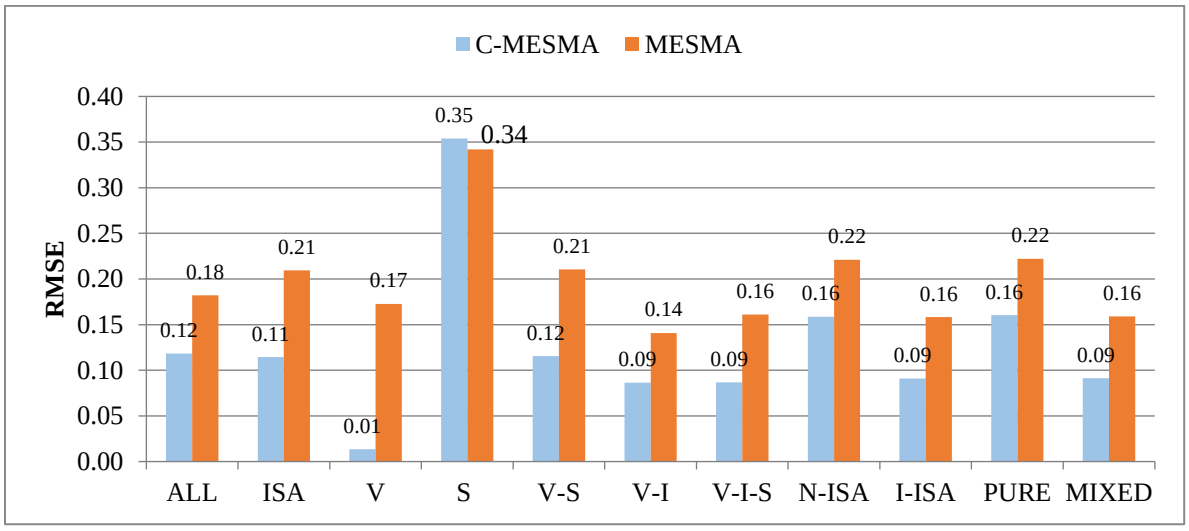

Figure 20 RMSEs of ISA in C-MESMA and MESMA methods. All: global RMSE; ISA: ISA; V: vegetation; S: soil; V-S: vegetation- soil; V-I: vegetation-ISA; V-I-S: vegetation-ISA-soil; N-ISA: ISA-excluded; I-ISA: ISA-included; PURE: pure land cover type (ISA, soil, and vegetation); MIXED: mixed land cover types (vegetation- soil, vegetation-ISA, and vegetation-ISA-soil)

To further investigate the relationship between the estimated fractions in the result of C-MESMA and the reference data, a scatter plot was employed to display their correlation (Figure 21). The trend line which indicates the linear relationship showed that the slope was close to one, and the R square value was 0.88, indicating a significant correlation between the estimated fractions and the reference values.

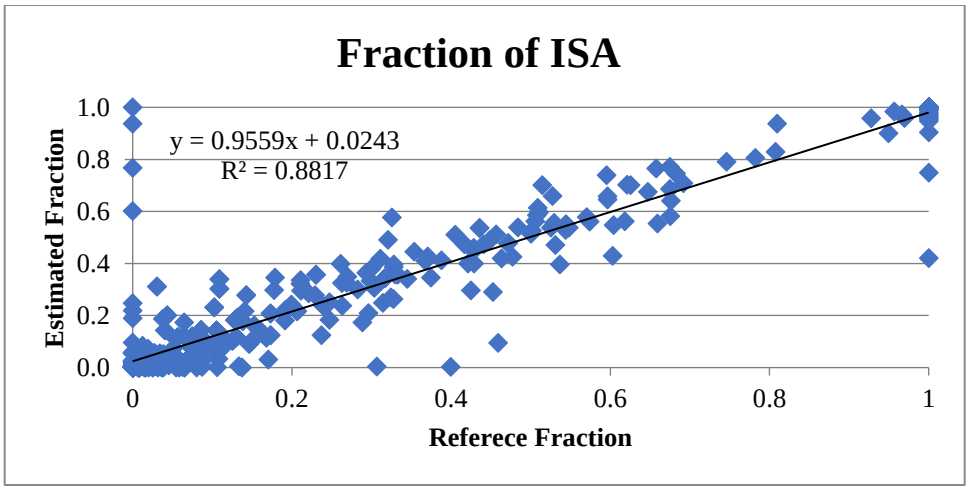

Figure 21 Scatter plot of ISA fraction

4.5 Discussion

Although MESMA allows endmembers and their combinations to vary from pixel to pixel, the "best-fit" model may still choose an inappropriate endmember set, majorly due to inter-class and intra-class variations of endmember spectra. As a result, erroneous fractional estimates of land covers may be obtained due to the mistakenly inclusion or exclusion of endmembers in the model (Jia et al., 2010). Unfortunately, few SMA/MESMA techniques have addressed this problem in previous studies, and most scholars ignore the fact that endmembers are not equally distributed spatially. Franke *et al.* (Franke et al., 2009) and Liu and Yang (Liu and Yang, 2013) did partially address this limitation by dividing the whole study areas into several regions, which, to some degree, restricts the distribution of endmembers. Their methods are also with limitations. Mixed

pixels cannot be fully separated with the classes of impervious surface and non-impervious surface areas/vegetation, thereby leading to the misclassification in the resultant segmented images. To accommodate the mixed pixel problem, mixed land cover types were introduced in the SVM classification. That is, the entire study area is classified into three pure land cover types (e.g., ISA, soil, vegetation) and three mixed land cover types (e.g., ISA-vegetation, soil-vegetation, and ISA-soil-vegetation). With this approach, a major limitation of pixel-based hard classifications, that only one land cover class can be assigned to a pixel (Deng et al., 2012; Tang et al., 2007), has been successfully addressed by allowing the assignment of pixels into a mixed land cover class.

C-MESMA not only constrains the spatial distribution of endmembers but also improves the computational efficiency. An issue of the traditional MESMA approach is the employment of a global spectral library for an entire study area. Although it can address the inter-class and intra-class spectral variability to some degree (Youngentob et al., 2011), the criteria of selecting the best-fit endmember model still need to be verified systematically, as it may include inappropriate endmembers . With C-MESMA, three separated spectral libraries are built based on corresponding mixed land cover types. On the one hand, the distribution of endmembers is restricted in the corresponding land cover classes, and inappropriate endmembers are excluded from the unmixing model. As an example, for the vegetation-ISA land cover type, only endmembers of vegetation and ISA are considered, and soil is effectively excluded in the model. With this advantage, the over-estimation of soil in urban areas was effectively addressed in the study area. On the other hand, with the reduction of irrelevant spectral endmembers, the number of spectral signatures decreases significantly, which improves the computational efficiency during the unmixng process. Moreover, with a lower number of spectral signatures in the spectral libraries, C-MESMA may also improve the computational efficiency. Some researchers have attempted to improve the

computational efficiency by separating the entire spectral library into several libraries. Each of these libraries only contains spectra of one land cover class (Dennison and Roberts, 2003). Computational time may be reduced with this strategy. However, only one spectrum of every land cover class can be included in each endmember combination, thereby reducing the performance of addressing the within-class variability. For instance, impervious surface area commonly contains two types of features, high albedo and low albedo surface features (Wu and Murray, 2003). These two types of land surface features are always close to each other, especially in the downtown areas. Misclassification may appear if only one of them is contained in the endmember combination models. On the contrary, C-MESMA considers all the spectra as potential endmembers. The reduction of spectral library size is attribute to the constraint of corresponding land cover types derived from the SVM classification. Besides, pure land cover classes resultant from the SVM are excluded from further spectral unmixing, which further reduces the computation time.

Although it has advantages, C-MESMA cannot adequately address the confusion between soil and ISA. This is because that the spectral signatures of sandy soil are highly like those of high albedo ISA. As a result, fractions of dry soil are overestimated. Nonetheless, most of the sandy soil is in the developing regions or the factory areas. These areas, to a certain degree, are classified as urban land uses.

4.6 Conclusions

A novel approach called land cover-class based multiple endmember spectral mixture analysis (C-MESMA), which combines the pixel-based supervised classification and MESMA, is proposed to extract the fractions of the ISA, vegetation, and soil. The C-MESMA, which first partitions the land cover into three pure land cover classes (vegetation, impervious surface area, and soil) and three mixed land cover types (ISA-vegetation, soil-vegetation, and ISA-soil-vegetation) and then

estimates the fractional coverages of mixed land cover classes using MESMA, is a promising and efficient method to prevent the appearance of inappropriate endmembers. Mixed pixels are being classified as an independent land cover class, breaking through the limitation of pixel-based classification that every pixel should belong to a pure land cover class. A fraction value of one is assigned to the corresponding pure land cover classes while the mixed land cover classes are unmixed using MESMA with their corresponding spectral libraries, not only improving the computational efficiency but also avoiding overestimating the fraction of improper endmember and underestimating the suitable endmember's fraction. Accuracy assessment and quantitative/qualitative analyses prove the significantly better performance of C-MESMA when compared to MESMA.

Admittedly, the classification accuracy of soil is relative low. A major reason is that the spectra of sandy soil and ISA are almost the same, which cannot be well distinguished through the SVM and MESMA. Additional information about soil should be included to reduce the mixture of sandy soil in the future. Moreover, the number of land surface features identified in this research is limited, and more details of specified materials in urban environment are expected to be distinguished in future experiments with the help of hyperspectral data.

CHAPTER5 CONCLUSIONS

5.1 Summary

SMA has been widely applied in various fields. Most scholars applied SMA based on their background knowledge and application requirements. Analysis about SMA, specially the uncertainties of endmembers and spectral mixture models, have not been discussed adequately. Therefore, this study: 1) provided analysis of endmember uncertainties by examining WSMA and TSMA in different study areas; and 2) addressed the uncertainties of spectral mixture modeling by introducing a class-based MESMA.

Specifically, this study explored endmember uncertainties by examining five existing weighting schemes as well as five potential weighting schemes in Janesville, WI and Asheville, NC, USA. Each scheme was tested 100 times with different spectra using the V-ISAh-ISAl endmember model. ISA's MAE was used to evaluate each scheme's performance. Then paired-samples T tests were applied to test if there was a significant difference of mean MAE between weighted and unweighted schemes. In addition, the effectiveness of twenty-six spectrally transformed schemes as well as the untransformed scheme in three urban areas were examined with Landsat data sets. Like the examination of WSMA, each scheme was repeatedly tested 100 times with different spectra using the V-ISAh-ISAl-S endmember model. MAE was also used as the criteria to assess each scheme's accuracy. Significant differences of mean MAE between transformed and untransformed schemes were tested using paired-sample T tests. Further, an index named BWVI was introduced to indicate the change of between- and within-class variance. Regression analysis was conducted to analyze the relationship between BWVI and MAE. Finally, this study developed a land cover class-based multiple endmember spectral mixture analysis (C-MESMA) method to address spectral mixture model uncertainties. A supervised classification was employed to divide

the stacked Landsat image into six segments, including three pure-class segments and three mixed-pixel segments. A fraction of one was assigned to the pure-classes' pixels directly while MESMA with the corresponding spectral libraries were applied to the mixed-pixel parts respectively. RMSEs of impervious surface area were employed to assess the performance.

5.2 Contributions

The first contribution about this study is to analyze endmember uncertainties in WSMA. WSMA is an alternate way to address endmember variability, the major source of endmember uncertainties. However, only a few weighting schemes have been discussed in previous studies. This study explored both existing and potential weighting schemes, providing a thorough comparison between different weighting schemes in urban environments. It provides references for other scholars about how to address endmember uncertainties using weighting schemes. And it also provides guideline about which directions to use in constructing a practical weighting scheme.

The second contribution of this study concerns addressing endmember uncertainties using TSMA. Like WSMA, TSMA is also a common method to address endmember uncertainties by highlighting the between-class variability and compressing the within-class variability. However, discussion about the TSMA in the literature is not sufficient. Therefore, this study provides a comprehensive analysis about how to address endmember uncertainties using a TSMA and which TSMA is the most effective to address endmember uncertainties. Additionally, an index named BWVI was developed to serve as a guide to select an appropriate transformed scheme for SMA in different study areas.

The third contribution addresses the uncertainties of spectral mixture models by developing a class-based MESMA (C-MESMA). The major uncertainty of the spectral mixture model is that it

may include some incorrect endmember in the best-fit model. C-MESMA may avoid incorrect endmembers by restricting endmembers in corresponding mixed pixels. Thus, it could improve accuracy significantly and reduce much of the calculation burden.

5.3 Future Research

My future research will focus on: 1) incorporating social information and other spatial and spectral information into the unmixing process, and 2) human interpretation simulation of mixed pixel unmixing. Currently, some scholars have incorporated spatial and spectral information, e.g., stacking the spectral indices into the original data set, fusing the high spatial resolution image with a lower spatial resolution data set, and merging geographical information, to enhance spectral characteristics. However, most of them did not take human social activities, such as the WIFI coverage map, the cumulative social communication activities map and similar data into account. Human social activities are highly correlated with the impervious surface areas since most of us live in the urban/suburban environments where most of the areas are covered by impervious surfaces. Therefore, human social activities, to some degree, can indicate the existence of impervious surfaces. Moreover, fractional estimation using SMA is a one-way process that we only follow for image pre-processing, endmember selection, unmixing, and accuracy assessment. It is different from the process of humans use to understand their environment. Humans interpret an image based on texture, spectral information, and other factors. Further, humans also use their background knowledge to verify their estimated results and to correct results. Thus, the traditional unmixing process, compared to human interpretation, lacks feedback from the unmixed results. Therefore, additional information is needed to provide proper verification of SMA results. With the assistance of additional information, there is a chance for SMA to correct unmixing results automatically. Therefore, an improved SMA may be able to provide more reliable fractional results.

REFERENCES

Adams, J.B., Sabol, D.E., Kapos, V., Almeida Filho, R., Roberts, D.A., Smith, M.O., & Gillespie, A.R. (1995). Classification of multispectral images based on fractions of endmembers: Application to land-cover change in the Brazilian Amazon. *Remote Sensing of Environment, 52*, 137-154

Ahmed, N., Natarajan, T., & Rao, K.R. (1974). Discrete cosine transform. *Computers, IEEE Transactions on, 100*, 90-93

Alejandro, M., & Omasa, K. (2007). Estimation of vegetation parameter for modeling soil erosion using linear Spectral Mixture Analysis of Landsat ETM data. *ISPRS Journal of Photogrammetry and Remote Sensing, 62*, 309-324

Amato, U., Cavalli, R.M., Palombo, A., Pignatti, S., & Santini, F. (2009). Experimental approach to the selection of the components in the minimum noise fraction. *Geoscience and Remote Sensing, IEEE Transactions on, 47*, 153-160

Arbiol, R., Zhang, Y., & Palà, V. (2006). Advanced classification techniques: a review. In, *Proceedings of the ISPRS Mid-term Commission VII Symposium, 292*

Asner, G.P., & Lobell, D.B. (2000). A biogeophysical approach for automated SWIR unmixing of soils and vegetation. *Remote Sensing of Environment, 74*, 99-112

Barducci, A., & Mecocci, A. (2005). Theoretical and experimental assessment of noise effects on least-squares spectral unmixing of hyperspectral images. *Optical Engineering, 44*, 087008-087008-087017

Bedini, E., Van Der Meer, F., & Van Ruitenbeek, F. (2009). Use of HyMap imaging spectrometer data to map mineralogy in the Rodalquilar caldera, southeast Spain. *International Journal of Remote Sensing, 30*, 327-348

Boardman, J. (1993). Spectral angle mapping: a rapid measure of spectral similarity. In: AVIRIS

Boardman, J.W., & Kruse, F.A. (1994). Automated spectral analysis: a geological example using AVIRIS data, north Grapevine Mountains, Nevada. In, *Proceedings of the Thematic Conference on Geologic Remote Sensing* (pp. I-407): Environmental Research Institute of Michigan

Bruce, L.M., Koger, C.H., & Li, J. (2002). Dimensionality reduction of hyperspectral data using discrete wavelet transform feature extraction. *IEEE Transactions on Geoscience and Remote Sensing, 40*, 2331-2338

Carvalho Junior, O., & Guimaraes, R. (2001). Employment of the multiple endmember spectral mixture analysis (MESMA) method in mineral analysis. In, *JPL AIRBORNE EARTH SCIENCE WORKSHOP* (pp. 73-80)

Chang, C.-I., & Ji, B. (2006). Weighted abundance-constrained linear spectral mixture analysis. *Geoscience and Remote Sensing, IEEE Transactions on, 44*, 378-388

Chavez, P., Berlin, G.L., & Sowers, L.B. (1982). Statistical method for selecting Landsat MSS ratios. *Journal of applied photographic engineering, 8*, 23-30

Chu, H.-f., Zhai, Z.-m., Zhao, Y.-d., Li, P.-x., & Zhang, L.-p. (2007). A convex cone analysis method for endmember selection of multispectral and hyperspectral images. *JOURNAL OF REMOTE SENSING-BEIJING-, 11*, 460

Chu, H., & Zhu, W. (2006). Image fusion algorithms using discrete cosine transform. *Optics and Precision Engineering, 14*, 266-273

Cloude, S.R., & Pottier, E. (1997). An entropy based classification scheme for land applications of polarimetric SAR. *IEEE Transactions on Geoscience and Remote Sensing, 35*, 68-78

De Jong, S.M., & van der Meer, F. (2004). *Remote Sensing Image Analysis: Including the Spatial Domain*. Springer Science & Business Media

Debba, P., Carranza, E.J.M., van der Meer, F.D., & Stein, A. (2006). Abundance estimation of spectrally similar minerals by using derivative spectra in simulated annealing. *Geoscience and Remote Sensing, IEEE Transactions on, 44*, 3649-3658

DeNavas-Walt, C., Proctor, B.D., & Smith, J.C. (2009). US Census Bureau.(2010). *Income, poverty, and health insurance coverage in the United States: 2009*

Deng, C., & Wu, C. (2012). BCI: a biophysical composition index for remote sensing of urban environments. *Remote Sensing of Environment, 127*, 247-259

Deng, C., & Wu, C. (2013a). Examining the impacts of urban biophysical compositions on surface urban heat island: A spectral unmixing and thermal mixing approach. *Remote Sensing of Environment, 131*, 262-274

Deng, C., & Wu, C. (2013b). A spatially adaptive spectral mixture analysis for mapping subpixel urban impervious surface distribution. *Remote Sensing of Environment, 133*, 62-70

Deng, Y., Fan, F., & Chen, R. (2012). Extraction and Analysis of Impervious Surfaces Based on a Spectral Un-Mixing Method Using Pearl River Delta of China Landsat TM/ETM+ Imagery from 1998 to 2008. *Sensors, 12*, 1846-1862

Deng, Y., & Wu, C. (2016). Development of a Class-Based Multiple Endmember Spectral Mixture Analysis (C-MESMA) Approach for Analyzing Urban Environments. *Remote Sensing, 8*, 349

Deng, Y., Wu, C., Li, M., & Chen, R. (2015). RNDSI: A ratio normalized difference soil index for remote sensing of urban/suburban environments. *International Journal of Applied Earth Observation and Geoinformation, 39*, 40-48

Dennison, P.E., & Roberts, D.A. (2003). Endmember selection for multiple endmember spectral mixture analysis using endmember average RMSE. *Remote Sensing of Environment, 87*, 123-135

Drake, N.A., Mackin, S., & Settle, J.J. (1999). Mapping vegetation, soils, and geology in semiarid shrublands using spectral matching and mixture modeling of SWIR AVIRIS imagery. *Remote Sensing of Environment, 68*, 12-25

Eastman, J., & Laney, R. (2002). Bayesian Soft Classification for Su b-Pixel Analysis: A Critical Evaluation

Elmore, A.J., Mustard, J.F., Manning, S.J., & Lobell, D.B. (2000). Quantifying vegetation change in semiarid environments: precision and accuracy of spectral mixture analysis and the normalized difference vegetation index. *Remote Sensing of Environment, 73*, 87-102

Fan, F., & Deng, Y. (2014). Enhancing endmember selection in multiple endmember spectral mixture analysis (MESMA) for urban impervious surface area mapping using spectral angle and spectral distance parameters. *International Journal of Applied Earth Observation and Geoinformation, 33*, 290-301

Fernández-Manso, A., Quintano, C., & Roberts, D. (2012). Evaluation of potential of multiple endmember spectral mixture analysis (MESMA) for surface coal mining affected area mapping in different world forest ecosystems. *Remote Sensing of Environment, 127*, 181-193

Fernandez-Manso, A., Quintano, C., & Roberts, D.A. (2016). Burn severity influence on post-fire vegetation cover resilience from Landsat MESMA fraction images time series in Mediterranean forest ecosystems. *Remote Sensing of Environment, 184*, 112-123

Finn, J.T. (1993). Use of the average mutual information index in evaluating classification error and consistency. *International Journal of Geographical Information Science, 7*, 349-366

FLAASH, U.G. (2009). Atmospheric correction Module; QUAC and FLAASH user guide v. 4.7. *ITT visual information solutions*

Foody, G.M. (1996). Approaches for the production and evaluation of fuzzy land cover classifications from remotely-sensed data. *International Journal of Remote Sensing, 17*, 1317-1340

Foody, G.M. (2002). Status of land cover classification accuracy assessment. *Remote Sensing of Environment, 80*, 185-201

Foody, G.M., Campbell, N., Trodd, N., & Wood, T. (1992). Derivation and applications of probabilistic measures of class membership from the maximum-likelihood classification. *Photogrammetric Engineering and Remote Sensing, 58*, 1335-1341

Franke, J., Roberts, D.A., Halligan, K., & Menz, G. (2009). Hierarchical multiple endmember spectral mixture analysis (MESMA) of hyperspectral imagery for urban environments. *Remote Sensing of Environment, 113*, 1712-1723

Giri, C.P. (2012). *Remote Sensing of Land Use and Land Cover: Principles and Applications*. CRC Press

Green, A.A., Berman, M., Switzer, P., & Craig, M.D. (1988). A transformation for ordering multispectral data in terms of image quality with implications for noise removal. *IEEE Transactions on Geoscience and Remote Sensing, 26*, 65-74

Hansen, M.C., & DeFries, R.S. (2004). Detecting long-term global forest change using continuous fields of tree-cover maps from 8-km advanced very high resolution radiometer (AVHRR) data for the years 1982–99. *Ecosystems, 7*, 695-716

Huguenin, R., & Jones, J. (1986). Intelligent information extraction from reflectance spectra: Absorption band positions. *Journal of Geophysical Research: Solid Earth, 91*, 9585-9598

Hyvarinen, A. (1999). Fast and robust fixed-point algorithms for independent component analysis. *IEEE transactions on Neural Networks, 10*, 626-634

Hyvärinen, A., & Oja, E. (2000). Independent component analysis: algorithms and applications. *Neural Networks, 13*, 411-430

Jensen, J.R., & Lulla, K. (1987). Introductory digital image processing: a remote sensing perspective

Jia, X., Dey, C., Fraser, D., Lymburner, L., & Lewis, A. (2010). Controlled spectral unmixing using extended Support Vector Machines. In, *Hyperspectral Image and Signal Processing: Evolution in Remote Sensing (WHISPERS), 2010 2nd Workshop on* (pp. 1-4): IEEE

Jia, X., & Richards, J.A. (1999). Segmented principal components transformation for efficient hyperspectral remote-sensing image display and classification. *Geoscience and Remote Sensing, IEEE Transactions on, 37*, 538-542

Kauth, R.J., & Thomas, G. (1976). The tasselled cap--a graphic description of the spectral-temporal development of agricultural crops as seen by Landsat. In, *LARS Symposia* (p. 159)

Krishnapuram, R., Keller, J.M., & Ma, Y. (1993). Quantitative analysis of properties and spatial relations of fuzzy image regions. *Fuzzy Systems, IEEE Transactions on, 1*, 222-233

Kruse, F.A. (1988). Use of airborne imaging spectrometer data to map minerals associated with hydrothermally altered rocks in the northern grapevine mountains, Nevada, and California. *Remote Sensing of Environment, 24*, 31-51

Kumar, U., Raja, S.K., Mukhopadhyay, C., & Ramachandra, T. (2013). Assimilation of endmember variability in spectral mixture analysis for urban land cover extraction. *Advances in Space Research, 52*, 2015-2033

Laba, M., Tsai, F., Ogurcak, D., Smith, S., & Richmond, M.E. (2005). Field determination of optimal dates for the discrimination of invasive wetland plant species using derivative spectral analysis. *Photogrammetric Engineering & Remote Sensing, 71*, 603-611

Li, J. (2002). *Linear unmixing of hyperspectral signals via wavelet feature extraction*. Mississippi State University

Li, J. (2004). Wavelet-based feature extraction for improved endmember abundance estimation in linear unmixing of hyperspectral signals. *Geoscience and Remote Sensing, IEEE Transactions on, 42*, 644-649

Li, S., Kwok, J.T., & Wang, Y. (2002). Using the discrete wavelet frame transform to merge Landsat TM and SPOT panchromatic images. *Information Fusion, 3*, 17-23

Ling, F., Du, Y., Xiao, F., & Li, X. (2012). Subpixel land cover mapping by integrating spectral and spatial information of remotely sensed imagery. *Geoscience and Remote Sensing Letters, IEEE, 9*, 408-412

Liu, K.-H., Wong, E., Wen, C.-H., & Chang, C.-I. (2013). Kernel-based weighted abundance constrained linear spectral mixture analysis for remotely sensed images. *IEEE Journal of Selected Topics in Applied Earth Observations and Remote Sensing, 6*, 531-553

Liu, L. (2008). BEST: Bayesian estimation of species trees under the coalescent model. *Bioinformatics, 24*, 2542-2543

Liu, T., & Yang, X. (2013). Mapping vegetation in an urban area with stratified classification and multiple endmember spectral mixture analysis. *Remote Sensing of Environment, 133*, 251-264

Lobell, D.B., & Asner, G.P. (2004). Cropland distributions from temporal unmixing of MODIS data. *Remote Sensing of Environment, 93*, 412-422

Loveland, T., & Belward, A. (1997). The international geosphere biosphere programme data and information system global land cover data set (DISCover). *Acta Astronautica, 41*, 681-689

Lu, D., Batistella, M., Moran, E., & Mausel, P. (2004). Application of spectral mixture analysis to Amazonian land-use and land-cover classification. *International Journal of Remote Sensing, 25*, 5345-5358

Lu, D., & Weng, Q. (2006). Use of impervious surface in urban land-use classification. *Remote Sensing of Environment, 102*, 146-160

Lu, D., & Weng, Q. (2009). Extraction of urban impervious surfaces from an IKONOS image. *International Journal of Remote Sensing, 30*, 1297-1311

Lu, D., Weng, Q., & Li, G. (2006). Residential population estimation using a remote sensing derived impervious surface approach. *International Journal of Remote Sensing, 27*, 3553-3570

Ma, J., Chan, J.C.-W., & Canters, F. (2014). Robust locally weighted regression for superresolution enhancement of multi-angle remote sensing imagery. *IEEE Journal of Selected Topics in Applied Earth Observations and Remote Sensing, 7*, 1357-1371

Melgani, F., & Bruzzone, L. (2004). Classification of hyperspectral remote sensing images with support vector machines. *Geoscience and Remote Sensing, IEEE Transactions on, 42*, 1778-1790

Mertes, L.A., Smith, M.O., & Adams, J.B. (1993). Estimating suspended sediment concentrations in surface waters of the Amazon River wetlands from Landsat images. *Remote Sensing of Environment, 43*, 281-301

Mountrakis, G., Im, J., & Ogole, C. (2011). Support vector machines in remote sensing: A review. *ISPRS Journal of Photogrammetry and Remote Sensing, 66*, 247-259

Mutanga, O., Skidmore, A., Kumar, L., & Ferwerda, J. (2005). Estimating tropical pasture quality at canopy level using band depth analysis with continuum removal in the visible domain. *International Journal of Remote Sensing, 26*, 1093-1108

Neville, R., Staenz, K., Szeredi, T., Lefebvre, J., & Hauff, P. (1999). Automatic endmember extraction from hyperspectral data for mineral exploration. In, *Proc. 21st Can. Symp. Remote Sens* (pp. 21-24)

Ogbu, F., & Smith, D.K. (1990). The application of the simulated annealing algorithm to the solution of the n/m/C max flowshop problem. *Computers & Operations Research, 17*, 243-253

Okujeni, A., van der Linden, S., Tits, L., Somers, B., & Hostert, P. (2013). Support vector regression and synthetically mixed training data for quantifying urban land cover. *Remote Sensing of Environment, 137*, 184-197

Pan, C., Wu, G., Prinet, V., Yang, Q., & Ma, S. (2005). A band-weighted landuse classification method for multispectral images. In, *2005 IEEE Computer Society Conference on Computer Vision and Pattern Recognition (CVPR'05)* (pp. 96-102): IEEE

Pathirana, S., & Fisher, P.F. (1991). Combining membership grades in image classification

Peddle, D., Brunke, S., & Hall, F. (2001). A comparison of spectral mixture analysis and ten vegetation indices for estimating boreal forest biophysical information from airborne data. *Canadian journal of remote sensing, 27*, 627-635

Plaza, A., Martínez, P., Pérez, R., & Plaza, J. (2004). A quantitative and comparative analysis of endmember extraction algorithms from hyperspectral data. *Geoscience and Remote Sensing, IEEE Transactions on, 42*, 650-663

Plaza, A., Valencia, D., & Plaza, J. (2006). High-performance computing in remotely sensed hyperspectral imaging: the pixel purity index algorithm as a case study. In, *Parallel and Distributed Processing Symposium, 2006. IPDPS 2006. 20th International* (p. 8 pp.): IEEE

Portigal, F., Holasek, R., Mooradian, G., Owensby, P., Dicksion, M., & Fene, M. (1997). Vegetation classification using red edge first derivative and green peak statistical moment indices with the Advanced Airborne Hyperspectral Imaging System(AAHIS). In, *International Airborne Remote Sensing Conference and Exhibition- Development, Integration, Applications & Operations, 3 rd, Copenhagen, Denmark*

Powell, R.L., Roberts, D.A., Dennison, P.E., & Hess, L.L. (2007). Sub-pixel mapping of urban land cover using multiple endmember spectral mixture analysis: Manaus, Brazil. *Remote Sensing of Environment, 106*, 253-267

Pu, R., Gong, P., Michishita, R., & Sasagawa, T. (2008). Spectral mixture analysis for mapping abundance of urban surface components from the Terra/ASTER data. *Remote Sensing of Environment, 112*, 939-954

Pyke, C.R., & Andelman, S.J. (2007). Land use and land cover tools for climate adaptation. *Climatic Change, 80*, 239-251

Qaid, A.M., & Basavarajappa, H. (2008). Application of optimum index factor technique to Landsat-7 data for geological mapping of north east of Hajjah, Yemen. *American-Eurasian Journal of Scientific Research, 3*, 84-91

Quintano, C., Fernández-Manso, A., & Roberts, D.A. (2013). Multiple Endmember Spectral Mixture Analysis (MESMA) to map burn severity levels from Landsat images in Mediterranean countries. *Remote Sensing of Environment, 136*, 76-88

Radeloff, V.C., Mladenoff, D.J., & Boyce, M.S. (1999). Detecting jack pine budworm defoliation using spectral mixture analysis: separating effects from determinants. *Remote Sensing of Environment, 69*, 156-169

Richards, J.A., & Richards, J. (1999). *Remote sensing digital image analysis*. Springer

Roberts, D.A., Gardner, M., Church, R., Ustin, S., Scheer, G., & Green, R. (1998). Mapping chaparral in the Santa Monica Mountains using multiple endmember spectral mixture models. *Remote Sensing of Environment, 65*, 267-279

Roberts, D.A., Quattrochi, D.A., Hulley, G.C., Hook, S.J., & Green, R.O. (2012). Synergies between VSWIR and TIR data for the urban environment: An evaluation of the potential for the Hyperspectral Infrared Imager (HyspIRI) Decadal Survey mission. *Remote Sensing of Environment, 117*, 83-101

Roberts, D.A., Smith, M.O., Sabol, D.E., Adams, J.B., & Ustin, S. (1992). Mapping the spectral variability in photosynthetic and non-photosynthetic vegetation, soils and shade using AVIRIS. In, *JPL, Summaries of the Third Annual JPL Airborne Geoscience Workshop.* (pp. 38-40): United States

Rogerson, P.A. (2014). *Statistical methods for geography: a student's guide*. Sage

Roth, K.L., Dennison, P.E., & Roberts, D.A. (2012). Comparing endmember selection techniques for accurate mapping of plant species and land cover using imaging spectrometer data. *Remote Sensing of Environment, 127*, 139-152

Rouse, J., Haas, R., Schell, J., & Deering, D. (1973). Monitoring vegetation systems in the great plains with ERTS. In, *Third ERTS Symposium* (pp. 309-317): NASA

Rudorff, C.M., Novo, E., & Galvão, L.S. (2006). Spectral mixture analysis of inland tropical Amazon floodplain waters using EO-1 Hyperion. In, *Geoscience and Remote Sensing Symposium, 2006. IGARSS 2006. IEEE International Conference on* (pp. 128-133): IEEE

Sabol, D.E., Adams, J.B., & Smith, M.O. (1992). Quantitative subpixel spectral detection of targets in multispectral images. *Journal of Geophysical Research: Planets (1991–2012), 97*, 2659-2672

Sala, O.E., Chapin, F.S., Armesto, J.J., Berlow, E., Bloomfield, J., Dirzo, R., Huber-Sanwald, E., Huenneke, L.F., Jackson, R.B., & Kinzig, A. (2000). Global biodiversity scenarios for the year 2100. *Science, 287*, 1770-1774

Settle, J. (2006). On the effect of variable endmember spectra in the linear mixture model. *Geoscience and Remote Sensing, IEEE Transactions on, 44*, 389-396

Settle, J., & Drake, N. (1993). Linear mixing and the estimation of ground cover proportions. *International Journal of Remote Sensing, 14*, 1159-1177

Shao, Z., & Liu, C. (2014). The integrated use of DMSP-OLS nighttime light and MODIS data for monitoring large-scale impervious surface dynamics: A case study in the Yangtze River Delta. *Remote Sensing, 6*, 9359-9378

Singer, R.B., & McCord, T.B. (1979). Mars-Large scale mixing of bright and dark surface materials and implications for analysis of spectral reflectance. In, *Lunar and Planetary Science Conference Proceedings* (pp. 1835-1848)

Singh, A. (1989). Review article digital change detection techniques using remotely-sensed data. *International Journal of Remote Sensing, 10*, 989-1003

Small, C. (2001). Estimation of urban vegetation abundance by spectral mixture analysis. *International Journal of Remote Sensing, 22*, 1305-1334
Small, C., & Lu, J.W. (2006). Estimation and vicarious validation of urban vegetation abundance by spectral mixture analysis. *Remote Sensing of Environment, 100*, 441-456
Small, C., Pozzi, F., & Elvidge, C.D. (2005). Spatial analysis of global urban extent from DMSP-OLS night lights. *Remote Sensing of Environment, 96*, 277-291
Somers, B., Asner, G.P., Tits, L., & Coppin, P. (2011). Endmember variability in spectral mixture analysis: A review. *Remote Sensing of Environment, 115*, 1603-1616
Somers, B., Delalieux, S., Stuckens, J., Verstraeten, W., & Coppin, P. (2009). A weighted linear spectral mixture analysis approach to address endmember variability in agricultural production systems. *International Journal of Remote Sensing, 30*, 139-147
Song, C. (2005). Spectral mixture analysis for subpixel vegetation fractions in the urban environment: How to incorporate endmember variability? *Remote Sensing of Environment, 95*, 248-263
Song, C., Huang, B., & Ke, L. (2013). Modeling and analysis of lake water storage changes on the Tibetan Plateau using multi-mission satellite data. *Remote Sensing of Environment, 135*, 25-35
Souza, C., Firestone, L., Silva, L.M., & Roberts, D. (2003). Mapping forest degradation in the Eastern Amazon from SPOT 4 through spectral mixture models. *Remote Sensing of Environment, 87*, 494-506
Strang, G., & Nguyen, T. (1996). *Wavelets and filter banks*. SIAM
Tallis, H., & Polasky, S. (2009). Mapping and valuing ecosystem services as an approach for conservation and natural-resource management. *Annals of the New York Academy of Sciences, 1162*, 265-283
Tan, K., Jin, X., Du, Q., & Du, P. (2014). Modified multiple endmember spectral mixture analysis for mapping impervious surfaces in urban environments. *Journal of Applied Remote Sensing, 8*, 085096-085096
Tang, J., Wang, L., & Myint, S. (2007). Improving urban classification through fuzzy supervised classification and spectral mixture analysis. *International Journal of Remote Sensing, 28*, 4047-4063
Thorp, K., French, A., & Rango, A. (2013). Effect of image spatial and spectral characteristics on mapping semi-arid rangeland vegetation using multiple endmember spectral mixture analysis (MESMA). *Remote Sensing of Environment, 132*, 120-130
Tompkins, S., Mustard, J.F., Pieters, C.M., & Forsyth, D.W. (1997). Optimization of endmembers for spectral mixture analysis. *Remote Sensing of Environment, 59*, 472-489
Trimble, S.W., & Crosson, P. (2000). US soil erosion rates--myth and reality. *Science, 289*, 248
Tsai, F., & Philpot, W. (1998). Derivative analysis of hyperspectral data. *Remote Sensing of Environment, 66*, 41-51
Tso, B., & Mather, P. (2001). Classification Methods for Remotely Sensed Data. 2001. *London and New York: Taylor & Francis, 332*
Tyler, A., Svab, E., Preston, T., Présing, M., & Kovács, W. (2006). Remote sensing of the water quality of shallow lakes: A mixture modelling approach to quantifying phytoplankton in water characterized by high-suspended sediment. *International Journal of Remote Sensing, 27*, 1521-1537
Veraverbeke, S., Somers, B., Gitas, I., Katagis, T., Polychronaki, A., & Goossens, R. (2012). Spectral mixture analysis to assess post-fire vegetation regeneration using Landsat

Thematic Mapper imagery: Accounting for soil brightness variation. *International Journal of Applied Earth Observation and Geoinformation, 14*, 1-11

Vermillion, S.C., & Sader, S.A. (1999). Use of the Minimum Noise Fraction (MNF) Transform to Analyze Airborne Visible/Infrared Imaging Spectrometer (AVIRIS) Data of Northern Forest Types. In, *JPL Workshop, JPL Publication*

Vetterli, M., & Herley, C. (1992). Wavelets and filter banks: Theory and design. *IEEE Transactions on signal processing, 40*, 2207-2232

Wang, J., & Chang, C.-I. (2006). Independent component analysis-based dimensionality reduction with applications in hyperspectral image analysis. *IEEE Transactions on Geoscience and Remote Sensing, 44*, 1586-1600

Wang, Y.-X., & Bao, F.S. (2007). An entropy-based weighted clustering algorithm and its optimization for ad hoc networks. In, *Third IEEE International Conference on Wireless and Mobile Computing, Networking and Communications (WiMob 2007)* (pp. 56-56): IEEE

Weng, Q. (2012). Remote sensing of impervious surfaces in the urban areas: Requirements, methods, and trends. *Remote Sensing of Environment, 117*, 34-49

Wessman, C.A., Bateson, C., & Benning, T.L. (1997). Detecting fire and grazing patterns in tallgrass prairie using spectral mixture analysis. *Ecological Applications, 7*, 493-511

Wu, C. (2004). Normalized spectral mixture analysis for monitoring urban composition using ETM+ imagery. *Remote Sensing of Environment, 93*, 480-492

Wu, C., & Murray, A.T. (2003). Estimating impervious surface distribution by spectral mixture analysis. *Remote Sensing of Environment, 84*, 493-505

Xie, H., Luo, X., Xu, X., Pan, H., & Tong, X. (2016). Automated subpixel surface water mapping from heterogeneous urban environments using Landsat 8 OLI imagery. *Remote Sensing, 8*, 584

Youngentob, K.N., Roberts, D.A., Held, A.A., Dennison, P.E., Jia, X., & Lindenmayer, D.B. (2011). Mapping two Eucalyptus subgenera using multiple endmember spectral mixture analysis and continuum-removed imaging spectrometry data. *Remote Sensing of Environment, 115*, 1115-1128

Yuan, F., & Bauer, M.E. (2007). Comparison of impervious surface area and normalized difference vegetation index as indicators of surface urban heat island effects in Landsat imagery. *Remote Sensing of Environment, 106*, 375-386

Zhang, H., Zhou, L.-G., Chen, M.-N., & Ma, W.-C. (2011). Land use dynamics of the fast-growing Shanghai Metropolis, China (1979–2008) and its implications for land use and urban planning policy. *Sensors, 11*, 1794-1809

Zhang, J. (2010). Multi-source remote sensing data fusion: status and trends. *International Journal of Image and Data Fusion, 1*, 5-24

Zhang, J., Rivard, B., & Sanchez-Azofeifa, A. (2004). Derivative spectral unmixing of hyperspectral data applied to mixtures of lichen and rock. *Geoscience and Remote Sensing, IEEE Transactions on, 42*, 1934-1940

Zhang, J., Rivard, B., Sánchez-Azofeifa, A., & Castro-Esau, K. (2006). Intra-and inter-class spectral variability of tropical tree species at La Selva, Costa Rica: Implications for species identification using HYDICE imagery. *Remote Sensing of Environment, 105*, 129-14

CURRICULUM VITAE

Education

2018 **Ph.D. Geography, University of Wisconsin-Milwaukee**

Disseration title: *Uncertainty assessment of spectral mixture analysis in remote senisng imagery*

Adviser: Dr. Changshan Wu

2013 **M.S. Cartography and Geographical Information Science, South China Normal University, China**

Thesis title: *Extraction of impervious surface area of Pearl River Delta*

Adviser: Dr. Fenglei Fan

2010 **B.S. South China Normal University, China**

Publications

1. **Yingbin Deng**, Changshan Wu*, Xin Zhang, Xiuping Jia. Examining the effectiveness of weighted spectral mixture analysis (WSMA) in urban environment. (*International Journal of Remote Sensing*, accepted)
2. **Yingbin Deng**, Changshan Wu*. Examining the effectiveness of transformed spectral mixture analysis in urban environment. (*ASPRS Photogrammetric Engineering & Remote Sensing*, in review)
3. **Yingbin Deng**, Changshan Wu*. Development of a Class-based Multiple Endmember Spectral Mixture Analysis (C-MESMA) Approach for Analyzing Urban Environments. *Remote sensing*. 2016, 8, 349.
4. **Yingbin Deng**, Changshan Wu*, Miao Li, Renrong Chen. "RNDSI: A ratio normalized difference soil index for remote sensing of urban/suburban environments." International *Journal of Applied Earth Observation and Geoinformation.* 2015 39: 40-48.
5. **Yingbin Deng**, Fenglei Fan* and Renrong Chen. Extraction and Analysis of Impervious Surfaces Based on a Spectral Un-Mixing Method Using Pearl River Delta of China Landsat TM/ETM+ Imagery from 1998 to 2008. *Sensors*. 2012, 12. P1846-1862
6. Fenglei Fan, **Yingbin Deng**, Xuefei Hu, Qihao Weng*. Estimating Composite Curve Number of SCS-CN Based on Remotely Sensed Variables in Guangzhou, China. *Remote Sens*. 2013,5: 1425-1438.
7. Fan Fenglei*, **Deng Yingbin**, Fan wei. Temporal Analysis of Forest Volume From 1990 to 2010 in Wugui Mountain of Zhongshan Based on Remote Sensing.*Guangdong Agricultural Sciences*. 2013, 4: 171-173.

8. Fenglei Fan*, **Yingbin Deng**, Yunqiang Zhu. Extracting impervious surface area and discussing urban expansion of Guangzhou (1990-2003) based on VIS model by using linear spectral mixture analysis method. *Journal of Food, Agriculture & Environment*. 2013, 11 (2), 925-929

9. Fenglei Fan*, **Yingbin Deng**, Enhancing Endmember Selection in Multiple Endmember Spectral Mixture Analysis (MESMA) for Urban Impervious Surface Area Mapping Using Spectral Angle and Spectral Distance Parameters. *International Journal of Applied Earth Observation and Geoinformation*. 12/2014; 33(3):290-301

10. Miao Li · Shuying Zang***** · Changshan Wu · **Yingbin Deng**. Segmentation-based and rule-based spectral mixture analysis for estimating urban imperviousness. Advances in Space Research. 12/2014. 55 (5): 1307-1315.

11. CHEN Ren-rong, ZHOU Shang-zhe*, **DENG, Yingbin**. Morphological Characteristics of Glacial Deposits during the Last Glaciation--- Taking the Parlung Zangbo River Basins as an Example. *Journal of Glaciology and Geocryology*. 2012, 34, p836-847.

12. Renrong Chen, Shangzhe Zhou*, **Yingbin Deng**. 2013. The morphological characteristics of glacial deposits during the Last Glaciation, taking the Parlung Zangbo River Basin as an example.*Sciences in Cold and Arid Regions*,5(6):0698~0708.

13. CHEN, Renrong, ZHOU, Shangzhe, LAI, Zhongping, OU, Xianjiao, CHEN, Rong and **DENG, Yingbin**. Luminescence chronology of late Quaternary moraines and Last Glacial Maximum equilibrium-line altitude reconstruction from Parlung Zangbo Valley, south-eastern Tibetan Plateau. *J. Quaternary Sci*., 2014. 29: 597–604. doi: 10.1002/jqs.2733

14. Renrong Chen, Shangzhe Zhou*, Yingkui Li, **Yingbin Deng**. Glacial geomorphology of the Parlung Zangbo Valley, southeastern Tibetan Plateau. *Journal of Map.* 2015. 08. 1-6.

Conference Presentations

2018 "Examination of spectrally transformed SMA", ISPRS Technical Commission III on Remote Sensing, Beijing, China, May 7-10

2018 "Examining the effectiveness of spectrally transformed SMA in urban environment". Association of American Geographers Annual Meeting, New Orleans, LA, April 10-14

2017 "Spectral mixture analysis: how and when to apply a weighting scheme". Association of American Geographers Annual Meeting, Boston, MA, April 5-9.

2016 "Development of a Class-based Multiple Endmember Spectral Mixture Analysis (C-MESMA) Approach for Analyzing Urban Environments". Association of American Geographers Annual Meeting, San Francisco, CA, March 29- April 2.

2015 "RNDSI: A ratio normalized difference soil index for remote sensing of urban/suburban environments". Association of American Geographers Annual Meeting, Chicago, Illinois. April 21-25

2014 "Enhancing Endmember Selection in Multiple Endmember Spectral Mixture Analysis (MESMA) for Urban Impervious Surface Area Mapping Using Spectral Angle and Spectral Distance Parameters". Association of American Geographers Annual Meeting, Tempa, Florida. April 8-12.

2012 "Extraction and Analysis of Impervious Surfaces Based on a Spectral Un-Mixing Method Using Pearl River Delta of China Landsat TM/ETM+ Imagery from 1998 to 2008". Graduate student Forum. Guangzhou, Dec 30.

2012 Conference attending. The 4th Forum on Environmental Remote sensing for Pearl River Delta Region, HK, Feb 24-25

2010 "Design and Implementation of geocoding system based on Geo-grid". The 7th International Symposium on LBS & TeleCartograph, Guangzhou, September 20-22.

Awards and Honors

2017 First Place of 2017 Student GIS Project Competition.

2017-2018 Outstanding Graduate Student Service Award

2014-2018 Mary Jo Read Awards, University of Wisconsin – Milwaukee (for 4 consecutive years)

2016-2017 Graduate School Distinguished Dissertation Fellowship(DDF) (18 were selected campus-wide) University of Wisconsin – Milwaukee

2013-2014 Chancellor's Graduate Student Awards. University of Wisconsin – Milwaukee

2012-2013 Huazhuang Scholarship (1 were selected from School of Geography), South China Normal University

2011-2012 Qiu Shi Graduate Scholarship (2 were selected from School of Geography) South China Normal University

2010-2011 Research & innovation award (for 2 consecutive years) South China Normal University

2008-2009 Fellowship of South China Normal University, Second Price

2007-2008 Fellowship of South China Normal University, Third Price

2007-2008 Self-renewal scholarship

2006-2007 Fellowship of South China Normal University, Second Price

Research Experience

2017-2018 Research Assistant, “Spectral mixture analysis: when and how to apply a weighting scheme, spectral transformation”

2010-2013 Research Assistant, “Impervious surface area extraction in urban/suburban environment” (National Science Found of China (NSFC, No: 41201432), Youth Research Training Project, and Project “863” of China (No: 2006AA06306))

2012-2013 Research member. Forest Volume survey (the project of Zhongshan Government)

2012-2013 Cooperation with CUHK. Cooperation on the land use change detection of Pearl River Delta.

2008-2010 Team leader of National Science Innovation Experiment Program for University Student. “Design and Implementation of Geo-coding system Base on Geo-Grid.”

2008-2009 Team leader of SCNU Research Project. “Compiled software to test the WIFI hotspots using C++.”

2008-2009 Team Leader of SCNU Continue Education college’s website construction.

2007-2008 Team member of SCNU Research Project. “A Web-based Tourism Service System.”

Teaching experience

Lectures:

Geog 247 Quantitative analysis in Geography (undergraduate level)

Geog 403 Remote sensing: Environmental and land use analysis (G/undergraduate level)

Teaching assistant:

Geog 625 Intermediate Geographic Information Science (Graduate/undergraduate level)

Geog 215 Introduction to Geographic Information Science (Undergraduate level)

Guest Lectures:

Geog 703 Advanced Remote Sensing (Graduate level)

Geog 547 Spatial Analysis (Graduate/undergraduate level)

Geog 525 Geographic Information Science (Graduate/undergraduate level)

Services

2018-2019	Student Co-Director (2018-2020) AAG Remote Sensing Specialty Group
2018	Supervisor of Wisconsin Science Olympiad, Division C, Remote Sensing.
2015-2018	Volunteer for Annual meeting of American Associate Geographers, Graduate school open house, and Tour of America's Dairy land
2017-2018	Graduate student representative, Department of Geography, UMW
2013-2017	Reviewer of *Water, Sensors, Remote Sensing, IEEE Xplore: IEEE Transactions on Geoscience and Remote Sensing*, *International Journal of Remote Sensing*, and *ISPRS Journal of Photogrammetry and Remote Sensing*.
2015-2016	Session organizer of AAG annual meeting 2015, 2016